OREGON HEALTH & SCIENCE UNIVERSITY
SCHOOL OF MEDICINE – GRADUATE STUDIES

Profiling Extracellular Vesicles in Niemann Pick Disease Type C

By

Sarah Catherine Briann Baker Hawthorne

A DISSERTATION

Presented to the Department of Developmental and Cellular Biology
and the Oregon Health & Science University
School of Medicine
in partial fulfillment of
the requirements for the degree of

Doctor of Philosophy

May 20th, 2025

CERTIFICATE OF APPROVAL

This is to certify that the PhD dissertation of

Sarah Catherine Hawthorne

has been approved by

_____REDACTED_____

Advisor, Julie Saugstad, Ph.D.

_____REDACTED_____

Member & Chair, Jonathan Brody, Ph.D.

_____REDACTED_____

Member, Anthony Paul Barnes, Ph.D.

_____REDACTED_____

Member, Gaurav Sahay, Ph.D.

_____REDACTED_____

Member, Joseph Quinn, M.D.

_____REDACTED_____

Outside Reader, Stuart Ibsen, Ph.D.

Contents

LIST OF ACRONYMS

Acronym	*Definition*
Aβ	Amyloid β
ANOVA	Analysis of Variance
APC	Allophycocyanin
APP	Amyloid precursor protein

BH	Benjamin-Hochberg procedure
CD	Hydroxypropyl-beta-cyclodextrin
CNS	Central nervous system
CSF	Cerebrospinal fluid
CTL	Control
DMEM	Dulbecco's modified eagle medium
dSTORM	Direct stochastic optical reconstruction microscopy
ESCRT	Endosomal sorting complex required for transport
EV	Extracellular vesicle
FBS	Fetal bovine serum
FDR	False discovery rate
FITC	Fluorescein isothiocyanate
GSL	Glycosphingolipid
Hex-Cer	Hexosylceramide
ICAM-1	Intercellular adhesion molecule-1
ILV	Intraluminal vesicle
IPA	Ingenuity pathway analysis
ISEV	International Society for Extracellular Vesicles
Lamp1	Lysosomal-associated membrane protein 1
Lamp4	Lysosomal-associated membrane protein 4
LPC	Lysophosphatidylcholine
MBFC	Multiplexed bead-based flow cytometry
miRNA	MicroRNA
mL	Milliliter
mRNA	Messenger RNA
MRPS	Microchip resistive-pulse sensing
MVB	Multivesicular body
NPC	Niemann pick disease type c
NPC1	NPC intracellular cholesterol transporter 1
NPC2	NPC intracellular cholesterol transporter 2
NPC-SS	Niemann pick disease type c clinical severity score (5 domains)
PBS	Phosphate buffered saline
PE	Phycoerythrin
qPCR	Quantitative polymerase chain reaction
RNA	Ribonucleic acid
SEC	Size exclusion chromatography
SEM	Standard error of the mean
SSD	Sterol sensing domain
TEM	Transmission electron microscopy

TMD	Transmembrane domain
TPS	Total protein stain
U18	U18666a
µl	Microliter
UTR	Untranslated region
VFC	Vesicle flow cytometry

LIST OF FIGURES

LIST OF TABLES

Dedication

To my father, Dr. Brian M. Baker, who set me on this journey.

To my mother, Laura A. Baker, who showed me how to finish it.

And to my husband, Kevin A. Hawthorne. The real prize was finding you.

ACKNOWLEDGEMENTS

In an early dissertation advisory committee meeting, one of my advisors (Dr. Gaurav Sahay) told me, “your PhD is a marathon.” I agreed with him at the time, and even more so now. Thankfully, I have not had to run this race alone. I have had many kinds of help: advisors making sure I had the right supplies and a clear map; lab mates ready to prop me up when I couldn’t finish the day; friends and family that were always standing on the sidelines, cheering me on when I needed it most. To everyone who has run this race with me, I am eternally grateful.

My lab deserves immediate thanks. Dr. Julie Saugstad has been a wonderful mentor. She supports all my unconventional ideas, guides my scientific philosophy, and always has chocolate ready for bad days. Dr. Ursula Sandau has been instrumental in this journey. She is both an incredible scientist and a wonderful teacher, and the opportunity to learn from her over these years has truly shaped who I am. Trevor McFarland has brought scientific guidance, sarcastic humor, and much needed perspective to life in lab. He has talked me off the cliff more than times than I can count, and I will always remember the phrase *making lemonade out of rocks* when looking at bad data. Dr. Sierra Smith, who walked this road just ahead of me, was my guiding light in lab and remains one of my closest friends. Brooke Rogers, our newest addition, brought fresh perspective and excitement to this embittered old graduate student, and allowed me to experience the joy of mentoring. To each of these scientists, co-workers, and friends: thank you.

My advisory committee has been a wonderful support network through my entire PhD. Dr. Paul Barnes served as my chair for the majority of this project, and provided an excellent example of what a caring, supportive scientific mentor should look like. I have missed having him pop in the lab from time to time to share his wisdom and (more often) his hilarious stories. Dr. Jonathan Brody stepped up to fill the Chair position this year, and throughout my PhD has

been a much-needed source of support and positivity as I navigated the world of extracellular vesicles. Dr. Gaurav Sahay provided excellent scientific advice (and life lessons; see above) that always left me excited about the next experiment. Dr. Joseph Quinn provided the original samples that started this project; without his support, none of this would have been possible (and yes, Julie expects you to open the champagne if I pass). Dr. Stuart Ibsen gamely agreed to read this dissertation despite knowing little about me and is yet another example of the excellent support I have received from OHSU faculty. I have been fortunate to have the opportunity to learn from each of you.

My friends and family probably won't read this, but I will thank them here anyway. Samantha Swan has been my best friend since kindergarten, and she followed me to Portland one year after I moved here. Her friendship got me through this PhD program, as it has gotten me through the rest of life's challenges. My friends Michael Martinez and Adrian Bars, who I met in this program, have filled my PhD with adventures, margarita nights, and Keanu Reeves movies. My family is my rock. When I moved to Portland I didn't know how far away it would feel, but each of them has supported me regardless. My brothers, Zach, Ian, and Nate; my uncles, John and Bob; my grandfather; my in-laws, Beth and Lauren; and most of all, my parents. I would not be who I am without each of you.

Finally, my husband, who I met on the first day of this PhD program and who has supported me through all of it. On late nights in lab, he brings me dinner; on early mornings, he drives me in. He has celebrated my successes, supported my struggles, and filled my life with love and joy. Thank you for being my partner.

ABSTRACT

Niemann Pick Disease Type (NPC), also known as "Childhood Alzheimer's," is a rare lysosomal storage disorder that causes neurodegeneration in infants, children, and young adults. The primary cellular defect in NPC is abnormal cholesterol accumulation in endolysosomes due to mutations in the *NPC1* or *NPC2* genes. This causes extensive dysregulation of the endolysosomal pathway, which also produces extracellular vesicles (EVs), nanoparticles that are shed from every known cell and play important roles in cellular communication. Many studies have demonstrated that EV molecular content, including proteins and microRNAs (miRNAs), is altered in disease states. Thus, EVs and their cargo have been implicated in a number of diseases, including neurodegeneration and lysosomal storage disorders. Current literature suggests that NPC affects the concentration and protein cargo of EVs. However, very few of these studies were performed on patient samples, and it is unknown whether EV alterations are related to the neurodegenerative phenotype seen in NPC patients. Additionally, while studies have demonstrated altered miRNA expression in NPC human cells or mouse tissue, nothing is yet known about NPC EV miRNAs in any model.

Here, we describe for the first time the profile of NPC EVs from patient cerebrospinal fluid (CSF) and patient dermal fibroblasts, as compared to CSF and fibroblast EVs from healthy human controls. Our results show that EV concentration is significantly elevated in NPC CSF and inversely correlates with NPC1 protein expression in fibroblasts. Using cell culture experiments we demonstrated that this increase can be partially attenuated by treatment with hydroxypropyl-β-cyclodextrin (CD), an experimental NPC therapeutic currently in Phase III clinical trials. We further found that CSF and fibroblast EVs are significantly enriched in the endolysosomal Lamp proteins. In CSF, EV expression of Lamp proteins inversely correlated with the age of disease onset; similarly, EV Lamp expression in fibroblasts was inversely correlated with cellular expression of the NPC1. These results indicate that EV alterations in NPC are connected with endolysosomal disturbances and are of clinical relevance. We also compared NPC and control miRNA expression in CSF EVs, fibroblast EVs, and fibroblast cells. Each group expressed distinct miRNAs, demonstrating that miRNA expression is both tissue and EV specific. NPC CSF EVs in particular showed differential expression of miRNAs 320a and 199a/b-3p, both of which have been implicated in cholesterol homeostasis. Together, these results add to our understanding of the fundamental cell biology linking endolysosomal injury to EV production and content and contribute novel information about a rare childhood disorder that currently has no cure.

CHAPTER I: INTRODUCTION

1.1. Niemann Pick Disease Type C

1.1a: NPC Disease Presentation

Niemann-Pick disease type C (NPC) is a rare autosomal recessive disorder that primarily affects children and young adults. NPC has a prevalence of approximately 1 in every 100,000 live births, with an estimated 42 new cases each year[1]. NPC is associated with severe morbidity and mortality. The average life expectancy is 13 and 70% of patients do not live past 26; these statistics have not improved since the 1980s[2]. The FDA approved the first two treatments for NPC in September of 2024, yet both are aimed at symptom management and are not curative[3]. New treatments are desperately needed.

NPC is neurovisceral disorder that causes symptoms in both the central nervous system (CNS) and the periphery. In infancy and early childhood, NPC primarily presents as liver and spleen disease accompanied by subtle neurological symptoms such as delayed developmental milestones [4]. Children, teenagers, and young adults typically present with neurodegenerative and psychiatric symptoms. These include motor control issues, such as clumsiness, seizures, and gaze palsy, as well as neurodegenerative symptoms such as behavioral change, memory loss, and cognitive decline[5]. Indeed, NPC is often called childhood Alzheimer's due to similarities in pathology and clinical symptoms of age-related Alzheimer's disease in adults[6]. However, NPC is an extremely heterogeneous disease and there is significant variation in disease onset, symptoms, and progression between patients.

NPC is caused by mutations in either the *NPC1* (95% of cases) or *NPC2* (5% of cases) genes, which respectively code for the NPC1 and NPC2 proteins[7]. The *NPC1* gene is found on chromosome 18q11 and was identified in 1997[8], while the *NPC2* gene is found on chromosome

14q24.3 and was identified in 2000[9]. Since their discovery, over 400 pathogenic mutations in *NPC1* and *NPC2* have been identified. The most common mutation among NPC patients results from a point mutation of cytosine to thymine at position 3182 in the *NPC1* gene, which results in an isoleucine residue instead of a threonine at position 1061 of the NPC1 protein. As such this mutation is commonly referred to as I1061T, and it results in the classic juvenile onset form of NPC disease[10].

However, even as the most common NPC mutation I1061T is only found in 20% of patients. The remaining 80% have mutations that can be entirely unique or shared with only a handful of other patients[5]. To add further complexity, NPC patients are often heterozygous, inheriting two different disease-causing alleles from each parent. This variety of *NPC1* and *NPC2* mutations likely contributes to the disease heterogeneity seen across all patients, as each mutation impedes the function of the NPC1 and NPC2 proteins to a different extent. For example, mutations that cause severe disruptions to the NPC1 protein (e.g. frameshift or nonsense mutations) typically result in the most severe neurological outcomes[5]. Yet genetic background alone does not fully explain the variability observed between NPC patients. Many family members with the same mutations have been shown to exhibit different symptoms and rates of progression, which has been illustrated by two interesting case studies on twins. In the first, two non-identical twins presented with similar cognitive disturbances but at very different ages (16 vs. 31); the 31 year old twin showed severe neurological impairments while his monozygotic 16 year old brother was largely asymptomatic[11]. While the exact cause of these variances in disease severity are unknown, possible contributors to these differences could include the maternal immune system, infection, or mRNA processing defects[12].

The high genetic heterogeneity between patients is a key challenge to understanding NPC biology. Many NPC studies focus on a single mutation or use genetic knockouts, yielding results that are only relevant to a small portion of patients. Building *in vitro* or *in vivo* models that represent the full spectrum of NPC patients is time and cost prohibitive. Given the rarity of the disease, human studies rarely obtain truly representative sample sizes. This has also presented challenges for clinical trials, as medications may work for some patients but not others.

To address these challenges, there have been a number of efforts to categorize NPC patients based on various forms of disease presentation, which could allow for more targeted investigations and/or better tracking through clinical trials. Two such classification schemes are:

i. *Age of onset:* the age at which patients first display neurological symptoms is largely considered the best predictor of their disease symptoms and severity[4]. This is not the age of diagnosis, which can sometimes occur years later, but is often estimated by information from a patient's primary caregiver. Earlier onset is associated with more severe disease and correlates with faster disease progression and shorter lifespan. The established age of onset categories are early infantile (under 2 years), late infantile (2-6 years), juvenile (6-15 years), and adolescent/adult (15+ years)[5].

ii. *NPC Clinical Severity Scales:* There are at least six different NPC Clinical Severity Scales (NPC-SS)[13]. Each assesses the severity of various NPC symptom categories (domains) on a points-based system, with higher scores corresponding to worse outcomes. Two severity scales that are largely accepted by clinicians and have been implemented in clinical trials are the 17-domain scale, which is the most comprehensive, and the 5-domain scale, which was designed to be a simpler version better-suited to routine clinical visits[14]. Creating a uniform scale to assess such a clinically heterogeneous disease is a significant challenge.

However, increased use of these scales has been a critical step towards standardizing data collection, as it allows for better comparisons of clinical and experimental results between studies.

1.1b: NPC Molecular and Cellular Pathology

NPC1 and NPC2 are endolysosomal proteins that are evolutionarily conserved and highly expressed in all human cell types[8]. NPC1 is comprised of ~1,278 amino acids consisting of 13 transmembrane domains and three luminal domains[15]. By contrast, NPC2 is a small protein comprised of 130 amino acids and is localized to the lysosomal lumen[16]. Both NPC1 and NPC2 play key roles in transporting cholesterol through the endolysosomal pathway.

Cholesterol typically enters the cell through endocytosis and resides in early endosomes, which then mature into late endosomes, and finally merge with lysosomes to form endolysosomes (**Fig 1.1**). Inside the endolysosomal lumen NPC2 binds cholesterol at its sterol-sensing domain (SSD). This complex then binds to the NPC1 protein, which has both a cholesterol binding domain and an NPC2 binding domain on its

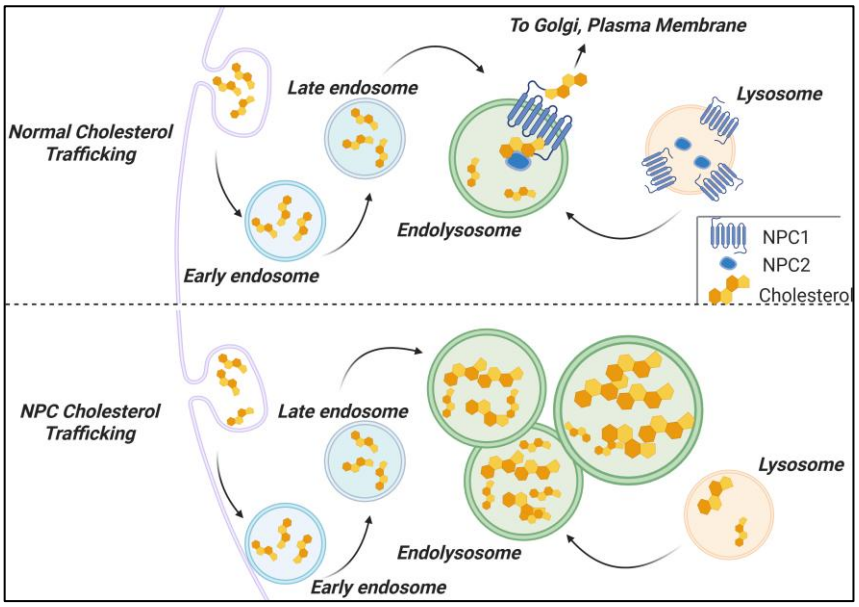

Fig 1.1: Cholesterol trafficking in normal and NPC cells. Cholesterol enters the cell through endocytosis. Early endosomes mature into late endosomes and fuse with lysosomes to produce endolysosomes. NPC1 and NPC2 proteins then move cholesterol across the endolysosomal membrane, allowing it to enter the cytoplasm and be further trafficked to the Golgi apparatus or plasma membrane. In NPC, loss of NPC1 or NPC2 leaves cholesterol trapped in endolysosomes, causing them to enlarge and multiply. The rest of the cell enters cholesterol starvation.

luminal side[17]. Cholesterol is then transferred from NPC2 to NPC1 (for Notre Dame scientists, this step is called the Holy (Hydrophobic) Handoff). NPC1 then transfers cholesterol across the endolysosomal membrane and into the cellular cytosol. While the exact mechanism of cholesterols transfer is still unknown, studies suggest it is passed along the SSD embedded in the NPC1 transmembrane domains[18]. Thus, NPC1 and NPC2 are essential for moving cholesterol out of the lysosomal compartment and into the rest of the cell where it can be used. Given this, it is not surprising that the cellular hallmark of NPC is over-accumulation of cholesterol inside endolysosomal compartments[19]. In fact, before the *NPC1* and *NPC2* genes were identified, NPC was diagnosed by staining patient skin biopsies for cholesterol[7].

However, cholesterol mis-trafficking is not able to fully explain NPC pathology, especially its neurological symptoms. Neurodegeneration in NPC is caused by progressive loss of Purkinje neurons in the cerebellum, and to a lesser extent neurons in the frontotemporal cortex[20]. Yet neither cell type is particularly dependent on cholesterol intake; *NPC1* and *NPC2* are expressed in neurons, but not to an unusual degree[21]. Why these cell types are particularly sensitive to NPC remains unknown.

The build-up of endolysosomal cholesterol in NPC creates a number of other cellular problems which may contribute to disease biology[22]. Secondary lipid accumulation severely disrupts the lipid profile of NPC endolysosomes, including a buildup of sphingomyelin, glycosphingolipids, and ceramides[23]. The autophagy pathway becomes dysfunctional, altering the rate of autophagic flux and causing autophagosomes to accumulate inside NPC cells[24]. Mitochondria are also disrupted, showing increased contacts with endolysosomes[25]. Recently, there has been growing interest in how endolysosomal disruptions in NPC affect extracellular vesicles (EVs), which can be produced through the endolysosomal pathway. Though not yet fully

understood, emerging evidence suggests that EV concentration and cargo is altered by NPC, making them key players in disease pathology.

1.2. Extracellular Vesicles

At their most basic level, extracellular vesicles (EVs) are nanoparticles released from cells. They range in size but are typically between 50 and 500nm; they are enclosed by a lipid bilayer; and they contain molecular cargo such as proteins, DNA, multiple forms of RNA (coding and non-coding), and metabolites[26]. While technically accurate, these definitions bely the incredible complexity and opportunity contained in these tiny packages. Every known cell releases EVs, from single-celled protozoa to human neurons. The cargo they contain reflects their cell of origin but does not perfectly mirror it. EVs can have dramatic effects on their recipient cells, including either causing disease or stopping it[27-29]. Although a nascent field of science, EVs have been implicated in nearly every type of human disease, including cancer[30, 31], neurodegeneration[32, 33], infection[34, 35], and even rare diseases[36, 37].

1.2a: Defining Extracellular Vesicles

Semantically, "EVs" is an umbrella term that can refer to any secreted cellular vesicles that are enclosed in a lipid bilayer and are incapable of replication[26]. Other terms to describe secreted vesicles (e.g. exosomes) are often used to refer to specific EV populations, but inconsistent definitions have led to confusion in the field. Thus, in 2018 the International Society for Extracellular Vesicles (ISEV; https://www.isev.org/) created guidelines that divided EVs into categories based on their general size and where they originated in the cell[26]. These guidelines, further updated in 2023[38], have been instrumental in standardizing EV terminology, enabling effective communication between EV researchers, and creating a theoretical framework for EV biology. Of particular interest for this project are the EVs known as exosomes, which originate

from endosomes and are enriched in endolysosomal proteins like CD63 and Flotillin-1; and the EVs known as microvesicles, which originate from the plasma membrane and enriched in Annexin and heat shock proteins[39]. Although these two populations overlap in size, exosomes are typically thought to be smaller in size (50-120nm) while microvesicles are thought to be larger in size (70-200nm).

While theoretically helpful, the ISEV guidelines themselves note that their EV definitions are functionally limited. ISEV defines EV subtypes loosely by size, although many EVs have overlapping size ranges; by place or origin (endosome or plasma membrane), which is difficult to prove with certainty; and by protein markers, none of which are always expressed on one EV type and never expressed on another[40]. The most common EV isolation techniques involve separating particles by size, either through column chromatography or centrifugation[41]. Therefore, many EV researchers have adopted the term "small EVs" (sEVs) to indicate that they have enriched for EVs under 200nm – which could include a mixed population of exosomes and microvesicles – without making claims about which exact type of particle they have isolated.

1.2b: EV Molecular Makeup

One of the most interesting aspects of EVs is their molecular cargo. Early EV researchers viewed them as a stochastic "trash disposal" system for the cell, wherein vesicles are generated and released with whatever cellular components were unneeded anymore and in proximity at the time of formation[42]. However, a landmark study challenged this assumption by reporting that RNA cargo in the parent cell and EVs were quite distinct, and that EV transfer into a recipient cell transformed the phenotype of that cell[43]. Since then, many studies have shown that EVs are enriched for certain cargo that is disproportionate to what is found in their parent cell[39]. These findings suggest that EVs are mechanistically packaged with specific molecules, either to

remove them from the parent cell or send them to a recipient cell. Whether EV cargo is randomly integrated, intentionally curated, or some mix of both, is still a matter of debate. Yet in either case, the cargo of EVs offers useful insight into the state of the parent cell. Cellular perturbations, either through disease or experimental manipulation, are known to alter EV cargo. Further, the functional effects that EVs have on recipient cells can be altered based on changes to the parent cell. This suggests that, random or not, EV cargo has important implications for parent cell biology and cell-to-cell communication. A brief, non-exhaustive description of the major types of molecular cargo found in EVs is presented below.

Proteins: Perhaps the most commonly studied EV cargo is their proteins, which include both surface proteins and internal cargo. Short of live-cell imaging experiments to visualize biogenesis, EV proteins can be the best indicator of EV subtype and place of origin. For example, the plasma membrane protein AnnexinV is often considered a marker for microvesicles, while endosomal proteins such as Lamp1 are thought to be markers of exosomes[39, 44]. The "canonical" markers for small EVs are the tetraspanin proteins CD63, CD81, and CD9.

RNA: Many forms of RNA have been found inside EVs. Perhaps the best studied are microRNAs (miRNAs), a class of short noncoding RNAs typically 18-22 nucleotides in length. MiRNAs can regulate protein expression by binding to target messenger RNAs (mRNAs), which usually result in reduced mRNA translation or degradation of the mRNA transcript. This discovery changed the paradigm of protein synthesis regulation, as evidenced by the 2024 Nobel Prize in Physiology and Medicine awarded to Drs. Ambros and Ruvkin for their discovery of miRNAs. MiRNAs down-regulate their target genes through binding of their seed sequence, which is typically 7 nucleotides long, to the 3' untranslated region (UTR) of their respective

mRNA targets[45]. However, this binding does not need to be perfect: in mammals it is dominated by the seed region at the 5' end of the mature miRNA, which consists of eight nucleotides[46]. Additional factors that can influence strong binding include the presence of a base towards the 3' end of the mature miRNA, the total number of miRNA binding sites at the 3' UTR, the proximity to the gene start, and the local A/U composition[46]. As one miRNA can bind many mRNA targets, and several distinct miRNAs can bind to one mRNA, these RNA interactions are very complex and regulate many different cellular pathways under both normal and disease states. For many pathologic conditions, EVs from diseased cells and tissues show altered miRNA expression. For this reason EV miRNAs have become candidate biomarkers for many diseases, including Alzheimer's disease[47, 48] and many types of cancer[31].

Lipids: By definition, all EVs are enclosed in a lipid bilayer[38]. Yet compared to other types of cargo, relatively little is known about the composition of EV bilayers and how they may vary by cell type or disease state. Foundational work by Skotland *et. al.* showed that EVs isolated from many cell types are composed of nearly 50% cholesterol, with other common lipids including sphingomyelin, phosphatidylcholine, and phosphatidylserine[49]. Some studies have shown that EV lipid composition changes in response to disease. For example, human brain-derived EVs in Alzheimer's disease show altered glycerophospholipid and sphingolipid content[50], and EVs from NPC cells are enriched in specific forms of ceramide[51].

1.2c: EV Biogenesis Pathways

The pathways responsible for EV biogenesis are complex and incompletely understood. Here, we will focus on the biogenesis of the two best-studied EV populations: exosomes and microvesicles.

Exosomes: EVs known as exosomes are formed inside of late endosomes. Invagination of the endosomal membrane creates small vesicles in the endosome lumen, termed intraluminal vesicles (ILVs) (**Fig 1.2**)[52]. Due to their appearance on electron microscopy, late endosomes loaded with ILVs are termed multivesicular bodies (MVBs). After ILV formation, an MVB fuses with the plasma membrane wherein the ILVs are released into the extracellular space as exosomes. The exact molecular cues that send an MVB to the plasma membrane, rather than to other locations in the cell (e.g., the lysosome) remain unclear[53].

The first exosome biogenesis pathway to be discovered relies on a family of proteins known as the endosomal sorting complex required for transport (ESCRT). In particular, ESCRT-0, I, II, III, and Vps4 are recruited to endosomal membranes enriched in the lipid phosphatidylinositol 3-phosphate (PI_3P) and promote inward budding to generate ILVs[52]. This pathway has been termed *ESCRT-dependent EV biogenesis*. In 2008, Trajkovic *et. al.* discovered an alternative exosome biogenesis pathway that relies on the neutral sphingomyelinase 2 (nSMase2) enzyme[54]. nSMase2, a transmembrane protein found in endolysosomes, cleaves sphingomyelin lipids (rectangular shaped) in endolysosomal membranes

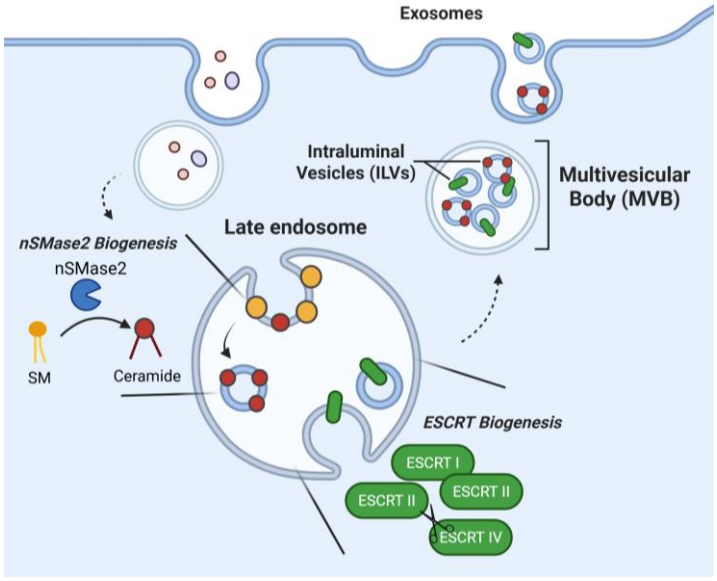

Fig 1.2: Exosomes biogenesis through the endosomal pathway. Inside late endosomes, ESCRT-dependent and ESCRT-independent pathways actively invert the endosomal membrane to form intraluminal vesicles (ILVs). An endosome laden with ILVs, also termed a multivesicular body (MVB), then merges with the plasma membrane where ILVs are released as exosomes.

into ceramide lipids (cone shaped). This transformation induces inward curvature in the endolysosomal membrane, which then forms ILVs. This pathway was termed "ESCRT-independent" biogenesis. nSMase2 EV biogenesis has been implicated in many diseases for its role in producing exosomes enriched in toxic cargo, such as those containing amyloid β (Aβ) fragments in Alzheimer's disease[55]. More recently, new ESCRT-independent biogenesis pathways have been proposed, including ones that rely on CD63, Flotillin-1, and lipid rafts[56-58]. Evidence suggests that these exosome biogenesis pathways co-occur in cells, but can be preferentially utilized by certain cell types or in certain disease states.

Microvesicles: EVs known as microvesicles (also termed ectosomes) are formed by outward budding of the plasma membrane. The pathways responsible for microvesicle formation involve complex rearrangement of both cytoskeletal and membrane components, facilitated in part by a local increase in calcium ions and proteolytic enzymes that disassemble the cytoskeleton[59]. Membrane curvature is facilitated by lipid-anchor modifications placed on proteins (e.g. myristylation or palmitoylation), and the GTPase ARF is required for secretion[60]. Some proteins involved in exosome biogenesis are also implicated in microvesicle biogenesis, such as TSG101 and ALIX.

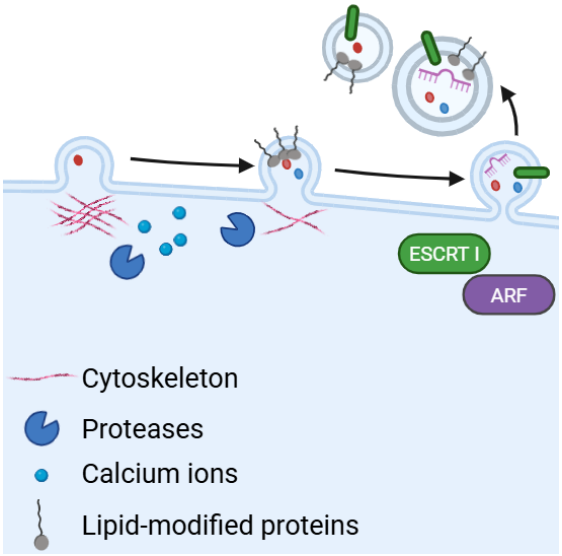

Fig 1.3: Microvesicle biogenesis at the plasma membrane. Increased concentration of proteases and calcium ions dissolves cytoskeletal proteins. Lipid-anchor modifications on proteins initiates outward budding of the plasma membrane, and cargo is sorted into membrane buds. ESCRT1 and ARF allow for the final pinching of the plasma membrane to release microvesicles into the extracellular space.

Theoretically, biogenesis also includes EV packaging with cargo. However, across all biogenesis pathways, the ways in which EV packaging is facilitated is incompletely understood. Some studies suggest the process is random and that EVs simply contain whatever content is nearby during biogenesis (sometimes termed "passive loading")[61]. Other studies have shown certain EV cargos, like miRNAs, contain "homing signals" that direct them to EVs[62]. It is likely that both processes occur, but the circumstances that favor one mechanism over another are unknown. A more detailed understanding of how EVs are formed and packaged for delivery to recipient cell(s) is a major focus for many studies spanning from normal to disease states.

1.2d: Methods to Isolate and Analyze EVs

EVs are notoriously difficult to work with, largely due to their small size, low concentration, and heterogeneity[41]. EVs are typically very small, often less than 100nm, that is at or below the limit of detection for standard analytical techniques that are optimized for cells, such as flow cytometry[63]. To circumvent this limitation, EV researchers must often employ specialized techniques and/or machinery, or risk that their EV data EV is hidden below background. Additionally, the concentration of EVs from common sources such as cell culture media, or uncommon (and more rare) sources such as cerebrospinal fluid (CSF), are often very low (less than 10^9 particles/mL)[64]. This can mean that in order to isolate enough EVs to analyze, researchers must either start with extremely large volumes – possible for models like cell culture but challenging for biofluids like CSF – or by carefully optimizing their techniques to require as little input as possible while still producing reliable data. Finally, EVs isolated from biological sources are extremely heterogenous[65]. Any one EV isolation likely contains many populations of EVs, each of which differs in terms of size, lipid composition, and surface proteins, etc. This heterogeneity distinguishes EV methodologies from other small particle protocols, such as

viruses or manufactured nanoparticles, which are able to optimize techniques for a fairly consistent population of particles with similar qualities.

To address these technical challenges and increase the rigor and reproducibility of EV research, ISEV and its working groups have created a number of recommendations for EV researchers[26, 38, 66]. In addition, ISEV has formed several Scientific Reproducibility Task Forces, each focused on improving and/or standardizing studies in a particular biofluid (https://www.isev.org/task-forces). A key theme of these recommendations is to use orthogonal methods to validate results (e.g., showing that a protein is enriched on EVs using both flow cytometry and microscopy).

The first step for any EV project is successful and reproducible isolation of EVs, which can be demonstrated in several ways. A common way to isolate EVs is the use of size-based methods, such as *i)* size exclusion chromatography (SEC), which uses resin-packed columns to separate particles in a fluid (CSF, cell culture media) into fractions based on particle size; or *ii)* ultracentrifugation, which uses high centrifugal force to pellet particles of a certain size range[41]. Other EV isolation methods include immunocapture using a known EV marker or protein of interest, or isolation based on precipitation using reagents like polyethylene glycol. Each isolation technique aims to separate true EVs from other particles, such as lipoproteins, proteins, or non-membranous particles. Yet often there is a tradeoff between purity and concentration, as the strictest isolation methods will also result in the lowest particle yield[38]. Regardless of method, EV researchers are encouraged to report the purity of their population of EVs using orthogonal techniques. According to the MISEV guidelines[26, 38], this verification can include a combination of:

i) Verifying that the isolation enriches for EV markers while minimizing the presence of other nanoparticles or cell debris. This is typically done by the use of immunoblots to show the presence of EV-associated transmembrane proteins (e.g. CD63, CD81, or CD9) and cytosolic proteins (e.g. TSG101), or the absence of proteins found on non-EV nanoparticles (e.g. apolipoproteins) and proteins found in cell lysate (e.g. calnexin).

ii) Visualizing the isolated membranous particles in their target size range with limited presence of other particles, typically shown through electron microscopy.

iii) Demonstrating the relative size and concentration of the EV population. This is often accomplished through techniques such as nanoparticle tracking analysis or microchip resistive-pulse sensing (MRPS).

1.3. NPC and EVs: Current Knowledge and Future Opportunities

EVs have emerged as a key component of human health and disease. In both lipid storage disorders and neurodegenerative diseases EVs play important roles in disease pathology and can serve as biomarkers[32, 37, 67]. While many elements of EV biology are likely impacted by the cellular disruptions that occur in NPC, little is known about the role of EVs in NPC.

To the best of our knowledge, to date only 18 peer-reviewed publications have directly examined EVs in the context of NPC (**Table 1.1**). The majority (12) utilized *in vitro* models, including immortalized cells (7), primary murine cells (3), human fibroblasts (1), or some combination of these cells. Three studies used cells that mimic neurological phenotypes, including oligodendrocyte precursors (Oli-neu) and primary rat neurons and astrocytes. Some studies used genetic tools to manipulate *NPC1/NPC2* expression, but the more common method was to treat cells with U18666A (U18). U18 is a small molecule inhibitor that specifically binds and inactivates the NPC1 SSD, reproducing the cholesterol storage problems in NPC cells[68].

Four studies investigated EVs in NPC mouse models, and only three studies examined EVs in NPC human samples, each of which relied on fibroblasts derived from a single patient. Given the heterogeneity between NPC patients, more studies on a larger cohort of NPC human samples are needed.

	Paper (Author Year)[Ref]	Experimental System	NPC EV Profile (Concentration/Cargo)	Mechanistic Findings
Human Samples	Strauss, 2010[72]	NPC1 fibroblast (R934X/P1007A)	Increased EV release and EV cholesterol	
	Ilnytska, 2021[79]	NPC1 fibroblast (P237S/I1061T)		NPC1 phenotype ameliorated via release of cholesterol-laden EVs
	Juhl, 2021[70]	NPC1 fibroblast (GM18455)		NPC2 drives cholesterol efflux from ELs via EV release
***In Vitro* Models**	Strauss, 2010[72]	Oli-neu cells + U18[1] or *NPC1* siNRA	Increased EV release and EV cholesterol	Cholesterol increases EV release in a Flotillin dependent manner
	Wustner, 2023[71]	*NPC2* KO fibroblasts		NPC2 is required for EV-driven sterol export
	Canfran-Duque, 2013[78]	HEPG2 and THP-1 cells + U18	No change to EV release	
	Cashikar, 2019[77]	T-Rex-293 cells + U18	No change to EV release	
	Feltes, 2020[80]	U2OS cells with *NPC1* KO		EVs do not mediate CD-driven cholesterol egress from NPC cells
	Albacete-Albacete, 2020[73]	Mouse embryonic fibroblasts + U18	Increased EV release	
	Cotafreda, 2020[35]			NPC1 facilitates HAV EV cargo uptake
	Wu, 2021[75]	Rat primary astrocytes + U18	Decreased EV release and altered EV proteins	
	Lu, 2021[81]	K562 cells with *NPC1* KO		Deletion of ESCRT proteins increases cholesterol in NPC KO
	Elgner, 2016[69]	Hu7.5 cells + U18		U18 inhibits exosome-mediated release of HCV viral particles
	Guix, 2021[72]	Aged rat cortical neurons	Increased EV release	Decreased NPC1 and increased cholesterol drive EV release
	Palmulli, 2024[56]	HeLa and MNT-1 cells + U18		CD63 and NPC1 sort cholesterol into ILVs for release as small EVs
***In Vivo* Models**	Chen, 2010[99]	NPC1 null mouse		CD does not alter EV release
	Van Hoecke, 2021[76]	NPC1^{m1N}/J mouse	Decreased and larger EVs	NPC choroid plexus EVs are cytotoxic
	Van Hoecke, 2021[28]	NPC1^{m1N}/J mouse		WT human MSC EVs ameliorate NPC pathology
	Soto-Huelin, 2023[51]	NPC1^{nmf174}/J mouse	Increased lipid content, esp. HexCer and LPC	NPC1 phenotype ameliorated by stimulating increased EV release

Table 1: NPC EV publications. EL: endolysosomes; PM: plasma membrane; U18: U18666A, a chemical inhibitor of NPC1; HCV: Hepatitis C Virus; HAV: Hepatitis A Virus; HexcCer: hexosylceramide; LPC: lyposphosphatidylcholine; KO: knockout

The current studies on EVs in NPC have primarily focused either on the mechanistic role of EVs in NPC pathways, or on how NPC disease affects EV production. It is important to consider that protocols for isolating and analyzing EVs vary widely between publications, and results must be interpreted within their methodological context. Despite these limitations, there is growing evidence that the NPC proteins play direct roles in EV biology; that EV concentration and cargo is altered by NPC pathology; and that EV packaging and release may be one method by which NPC cells attempt to remove cholesterol from endolysosomes. To further understand how EVs contribute to or are affected by NPC, these studies must be carefully considered and built upon.

1.3a: NPC Proteins in EV Uptake and Release

The NPC proteins have been implicated in various phases of the EV life cycle. For example, evidence from virology has shown that NPC1 is essential for the endosomal uptake of cargo delivered by hepatitis A viral EVs[35]. Conversely, NPC1 is essential for the release of EVs containing hepatitis C viral particles[69]. There is also evidence that NPC2 participates in EV release by trafficking cholesterol-rich ILVs from endolysosomes and allowing microvesicles to shed directly from the plasma membrane[70, 71]. Similarly, the NPC1 protein interacts with CD63 to facilitate the release of cholesterol-enriched ILVs from endolysosomes[56]. These studies suggest that loss of either the NPC1 or NPC2 protein would impact EV uptake and/or release.

1.3b: Alterations to EV Concentration in NPC Samples

There is conflicting evidence as to whether NPC results in an increase[72-74], decrease[75, 76], or no change[77, 78] to EV concentrations relative to controls. A thorough and frequently-cited study by Strauss *et. al.* found that NPC pathology, which they modeled through siRNA knockdown of *NPC1,* the U18 drug inhibitor, or cholesterol-loading cells, led to increased release of EVs[72].

They further showed that NPC EVs contained higher concentrations of cholesterol and were released in a Flotillin-1 dependent manner, and they replicated their results in a patient fibroblast cell line. Their findings were supported by Albacete-Albacete *et. al.*, who also found that treating mouse embryonic fibroblasts with U18 increased EV release[73]. However in immortalized cell lines, including HEK293[77], HepG2[78], and THP-1[78], treatment with U18 does not alter EV concentration.

Given that NPC is characterized by both peripheral and neurological defects, there have also been studies on NPC and EVs in brain models. For example, rat cortical neurons released an increased amount of EVs following exposure to U18[74]. Genetic manipulations further showed that NPC1 regulates ILV production, such that loss of NPC1 leads to increased ILV formation[74]. In contrast rat astrocytes treated with U18 showed decreased EV release, suggesting that this relationship may be cell-type specific[75]. Further, the choroid plexus of $NPC^{-/-}$ mice contained significantly fewer EVs but they were larger, suggesting a change in EV subpopulations[76].

Comparing the outcomes of these studies is complicated by the fact the experiments utilized different *in vitro* and *in vivo* models of NPC, as well as different EV isolation and analysis techniques. Yet taken together, these findings suggest that the effect of NPC pathology on EV concentration likely varies by cell type, animal model, and the extent to which the NPC1 protein is inhibited. Importantly, and relevant to the studies presented herein, the only study to examine EV concentrations in NPC patients used one fibroblast cell line from one person[72]. Given the large heterogeneity amongst NPC patients in terms of genetics and disease severity, repeated analysis in a larger cohort of patients is critical. Additionally, a better understanding of how EV concentrations are altered in peripheral vs. neural tissues could reveal important biology behind the neurodegenerative aspects of NPC.

1.3c: Therapeutic Effects on NPC EVs

New therapeutics for NPC are often aimed at lowering cholesterol levels in endolysosomes, either by redistributing it to other cellular locations or removing it from the cell entirely. As these therapeutics are developed, some researchers have hypothesized that cholesterol removal in NPC could be facilitated by EVs. For example, treating an NPC patient fibroblast line with phosphatidylglycerol substantially reduced cellular cholesterol by exporting it via EVs[79]. Similarly, treating mice with the candidate NPC treatment ellagic acid dramatically increased EV release while reducing levels of cellular cholesterol and other lipids[51]. Further, many NPC patients have been treated with the experimental drug hydroxypropyl-β-cyclodextrin (CD), which has shown conflicting efficacy but is currently in Phase III clinical trials (NCT04860960)[5]. Studies have shown that EVs are not involved in the CD-mediated mechanism of lowering cholesterol, but whether EV release is increased after CD treatment or involved in other cellular pathways was not investigated[80].

Conversely, inhibiting EV release in NPC cell lines can have damaging effects. In a patient cell line, inhibiting exosome release with GW4869 (a drug that blocks nSMase2-driven ESCRT-independent EV biogenesis) caused significant accumulation of cholesterol-rich vesicles at the plasma membrane[79]. A CRISPR screen performed under U18-driven NPC1 inhibition showed that deletion of any of the ESCRT proteins increased cellular cholesterol[81], in agreement with a previous study showing that knockdown of ESCRT-0 causes NPC-like cholesterol accumulation[82]. Together, these studies suggest that EVs play a beneficial role in NPC, possibly by removing endolysosomal cholesterol.

1.3d: The Molecular Cargo of NPC EVs

Although few, the studies that have examined the molecular cargo of EVs from NPC samples have yielded interesting results. Two studies have shown that EVs from NPC mouse models cause significant cell death and stress signaling in recipient cells, suggesting that NPC EVs are enriched in cytotoxic material[75, 76]. Wu *et. al.* linked this cytotoxicity to increased amyloid precursor protein (APP) and Aβ fragments they observed in NPC EVs[75]. These markers are highly relevant to the development Alzheimer's disease, which shares many similarities with NPC[6]. The authors also a noted significant decrease in Lamp1 and LC3 expression in EVs released from cells treated with U18, implicating EVs in the autophagy disruptions previously observed in NPC[24].

Given the lipid dysregulation of NPC, understanding the lipid content of NPC EVs is of great interest. As described previously, Strauss *et. al*. found increased cholesterol content in EVs isolated from an NPC cell line[72]. Another study examining the lipid content of EVs from control and $NPC^{-/-}$ mouse brain tissue found a general increase in lipid content of NPC EVs, including significant increases in hexosylceramide (HexCer) and Lysophosphatidylcholine (LPC)[51]. LPC has been previously implicated in NPC and is a proposed biomarker for tracking response to CD treatment response [83].

These studies emphasize that EVs from NPC sources are enriched in proteins and lipids that are highly relevant to disease pathology. As with other neurodegenerative diseases and lysosomal storage disorders, identifying NPC EV cargo will likely inform our understanding of NPC biology, and possibly lead to the identification of novel biomarkers or therapeutic targets for the treatment of NPC[84, 85].

1.4: Project Rationale

The current literature suggests that EVs are altered in NPC and that these changes are relevant to NPC pathology. However, a number of critical questions remain. First, the conflicting evidence on whether EVs are increased or decreased in NPC samples suggests that the ways in which NPC affect EV formation and release may be complex, and dependent on the cell type and the subspecies of EVs analyzed (exosomes, microvesicles, or both). There is some data suggesting that NPC EVs carry altered protein and lipid content, though whether these cargo alterations are relevant to NPC pathology is unknown. Additionally, there is not yet any information on how EV miRNAs are altered in NPC. Whether any of these EV changes are related to the extensive endolysosomal disruptions found in NPC is also currently unknown. Finally, determining whether there are CNS-specific changes to EVs in NPC could help to explain the neurodegenerative aspects of the disease.

To address these questions, this project compared the EV profile of NPC patients to age-matched controls, including EV size, concentration, surface markers, and miRNA cargo, using EVs from CSF (Chapter 2) and dermal fibroblasts (Chapter 3). The data revealed that in both sample sets, NPC had altered EV concentrations and cargo as compared to controls. These alterations were primarily in EVs of endosomal origin, suggesting that EV changes stem from issues with the endolysosomal pathway in NPC. Additionally, some of the changes to EVs correlated with clinical aspects of NPC (such as age of disease onset or NPC1 protein expression). Ultimately, this work contributes to a growing body of evidence that NPC – and the endolysosomal disruptions it causes – fundamentally alter EV biology. It additionally raises the possibility that EV changes could be used as clinical biomarkers or therapeutic targets for a devastating disease that currently has no cure.

CHAPTER 2:

INCREASED ENDOLYSOSOMAL CONTENT AND miRNA EXPRESSION IN NPC PATIENT CEREBROSPINAL FLUID EVS

2.1: Abstract

Niemann Pick Disease Type C (NPC) is a rare neurodegenerative disease primarily caused by mutations in the NPC1 protein. NPC1 shuttles cholesterol from inside the lumen of late endosomes/lysosomes (endolysosomes) and into the cytosol. Thus, the fundamental cellular pathology of NPC is endolysosomal dysfunction caused by overaccumulation of cholesterol. However, the pathways by which NPC1 mutations result in neurodegeneration are currently unknown. Extracellular vesicles (EVs), which can be formed through the endolysosomal pathway, have been implicated in both neurodegenerative and lysosomal storage disorders. A growing body of work has demonstrated that EV concentration and cargo are fundamentally disrupted in NPC. However, limited work has been done on NPC EVs in human samples, and whether EV perturbations are linked to neurological defects in NPC remains unknown. Here, we compared EV populations in cerebrospinal fluid (CSF) from five healthy donors and five age-matched NPC patients undergoing treatment with hydroxy-propyl-beta-cyclodextrin (CD). We found that NPC CSF contained an increased concentration of EVs relative to controls, including a specific expansion of CD63-positive EVs. We also found NPC CSF EVs are enriched in Lamp1, an endolysosomal protein previously implicated in NPC pathology. Finally, we identified two miRNAs significantly upregulated in NPC CSF EVs, which are active in cholesterol signaling and other disease-relevant pathways. Together, these studies demonstrate that NPC fundamentally alters the concentration, subtype, and molecular cargo of CSF EVs, elucidating new biological pathways for a devastating disease that currently has no cure.

2.2: Introduction

Niemann Pick Disease Type C (NPC) is a rare neurodegenerative lipid storage disorder characterized by abnormal accumulation of cellular cholesterol[7]. NPC primarily affects infants, children, and young adults, and has an estimated prevalence of 1 in every 100,000 births[5]. Though there is high heterogeneity in age of onset and disease progression, 70% of NPC patients do not live past 26[2]. The FDA approved its first two treatments for NPC in 2024, yet both are aimed at symptom management and are not curative[3]. Thus, new treatments are desperately needed by patients.

Like many rare diseases, there is wide heterogeneity amongst NPC patients with regards to age of onset, disease severity, symptoms, and rates of progression[5]. This can partially be attributed to genetic diversity, as over 400 pathogenic *NPC1* mutations have been described and each one impacts NPC1 protein function differently[5]. However, most patients experience neurological symptoms such as loss of motor control, behavioral changes, and cognitive decline[4]. Brain changes in NPC patients include progressive death of Purkinje neurons in the cerebellum, degeneration of neurons in the hippocampus and frontotemporal lobe, and reduced myelination[21]. However, why *NPC1* mutations lead to a primarily neurodegenerative phenotype is unclear. Therefore, more research on the central nervous system (CNS) defects in NPC is needed.

Recently, EVs have emerged as key drivers of human disease[42]. EVs are membrane-enclosed nanoparticles that are released by all cell types and found in every human biofluid[26, 38]. EVs can be formed through many pathways, including at the plasma membrane (forming EVs known as microvesicles/ectosomes) or through the endolysosomal pathway (forming EVs known as exosomes)[60]. They carry molecular cargo, such as proteins, microRNAs (miRNAs), and lipids, which largely reflect their cell of origin and can be altered in disease states[86]. As such, EVs have

been implicated in the pathology of both neurodegenerative and lysosomal storage disorders[33, 37]. However, research on EVs in NPC is limited and has produced conflicting results.

Studies have shown that EV concentrations in NPC samples are increased, decreased, or unchanged[72-76, 78]. Only one of these studies was conducted on human samples, and it included a single fibroblast cell line from an NPC patient[72]. Similarly, there have been no studies on how the molecular cargo of EVs is altered in NPC human samples, although research in mouse models have shown that NPC EVs carry cytotoxic proteins and have an elevated lipid content[51, 75, 76]. MiRNAs are key regulators of cellular pathways known to be disrupted in NPC cell lines and tissues, and their differential expression in EVs has revealed new therapeutic targets and potential biomarkers in other neurodegenerative diseases[87, 88]. However, nothing is yet known about how NPC influences EV miRNA content.

Though limited, the existing literature suggests that EVs are fundamentally altered in NPC. In order to fully understand how EVs may be altered by or contributing to the neurodegenerative pathology of NPC, more research on EVs in human samples is needed. Here, we profiled EVs in cerebrospinal fluid (CSF) from healthy control and NPC donors. Our results show that NPC CSF contains an increased concentration of EVs, largely driven by expansion of EVs of endosomal origin, and that NPC EVs are enriched in surface proteins and miRNAs that are highly relevant to NPC pathology. The studies herein show for the first time that EVs are altered in CSF from human NPC patients relative to healthy controls, and demonstrate the importance of EV research in the context of NPC.

2.3: Results

2.3a: CSF Donor Demographics

Demographic and clinical information on CSF samples from healthy control donors (n=5) and NPC patients undergoing treatment with hydroxy-propyl-β-cyclodextrin (CD) (n=5) is listed in **Table 2.1**. Given the strong correlation between age and the expression of EV proteins in human CSF (**Supplementary Fig 2.1**), control and NPC donors were age-matched to the greatest extent possible. NPC samples had a mean age of 21.8 years (standard deviation=6.3), while control samples had a mean age of 22.6 years (standard deviation=0.54). Although all control samples are female, we expect this had minimal impact as no sex differences have been observed in NPC human studies[2]. The NPC patients displayed heterogeneity in age of disease onset (mean=12.8 years, standard deviation=7.8), which is notable as earlier onsets are linked to more severe disease[5]. One patient (NPC-1) presented in the late-infantile group (age of onset at 4); two patients in the juvenile group (NPC-4, age of onset at 11; NPC-5, age of onset at 13); and two patients in the adolescent/adult group (NPC-2, age of onset 16; NPC-3, age of onset 23)[4].

Table 2.1: Human CSF samples

Status	Sample	Sex	Age at Collection	Age of Onset	5-Domain NPC-SS	Months on CD	Response to CD
NPC *n=5*	NPC 1	F	17	4	13	28	Fair
	NPC 2	M	24	16	7	11	Fair
	NPC 3	M	32	23	7	2	Poor
	NPC 4	F	18	11	5	3	Good
	NPC 5	M	18	13	1	28	Good
CTL *n=5*	CTL 1	F	22	-	-	-	-
	CTL 2	F	22	-	-	-	-
	CTL 3	F	23	-	-	-	-
	CTL 4	F	23	-	-	-	-
	CTL 5	F	23	-	-	-	-

NPC-SS: 5 domain NPC Severity Scale. Scale assesses patient ambulation, fine motor skills, swallow ability, cognition, and speech on a five-point, with a maximum score of 25. Higher scores correspond to more severe impairment.

There was also heterogeneity in patient disease severity, as measured by the 5-point NPC Severity Scale (NPC-SS)[14]. Scores ranged from 1-13, out of a maximum possible score of 25, with higher scores correlated to more severe impairment (mean score=6.5, standard deviation=5). Age of onset and NPC-SS were not well-correlated in our samples (**Fig 2.1**). All patients were being treated with CD at time of CSF collection, but their length of time on CD ranged from 2-27 months (mean=14.8 months, standard deviation=14.2). Patient response to CD, as graded by the treating clinician, ranged from poor to good.

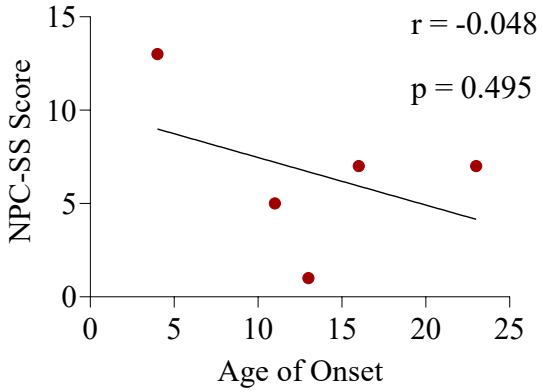

Fig 2.1: Age of onset and NPC-SS scores do not correlate in our patient cohort. p- and r-values derived from Pearson's correlation. Line represents simple linear regression.

The five NPC patients carried a range of mutations in the NPC1 protein, described in **Table 2.2**. The NPC1 protein contains 13 transmembrane domains (TMDs), which include a sterol-sensing domain (SSD), as well as three luminal-facing domains that contain binding sites for cholesterol and the NPC2 protein (**Fig 2.2**)[89]. While the impact of each mutation on NPC1 protein structure is unknown, some

Table 2.2: NPC Patient Mutations

	Allele 1		Allele 2	
Sample	**Gene**	**Protein**	**Gene**	**Protein**
NPC 1	2000 C>T	S667L	410 C>T	T137M
NPC 2*	3019 C>G	P1007A	3019 C>G	P1007A
NPC 3	2196dupT	S733fsX10	1301 C>T	P434L
NPC 4	3425 T>C	M1142T	2366 G>A	R789H
NPC 5	2000 C>T	S667L	410 C>T	T137M

*Mutation identified by sequencing sister.

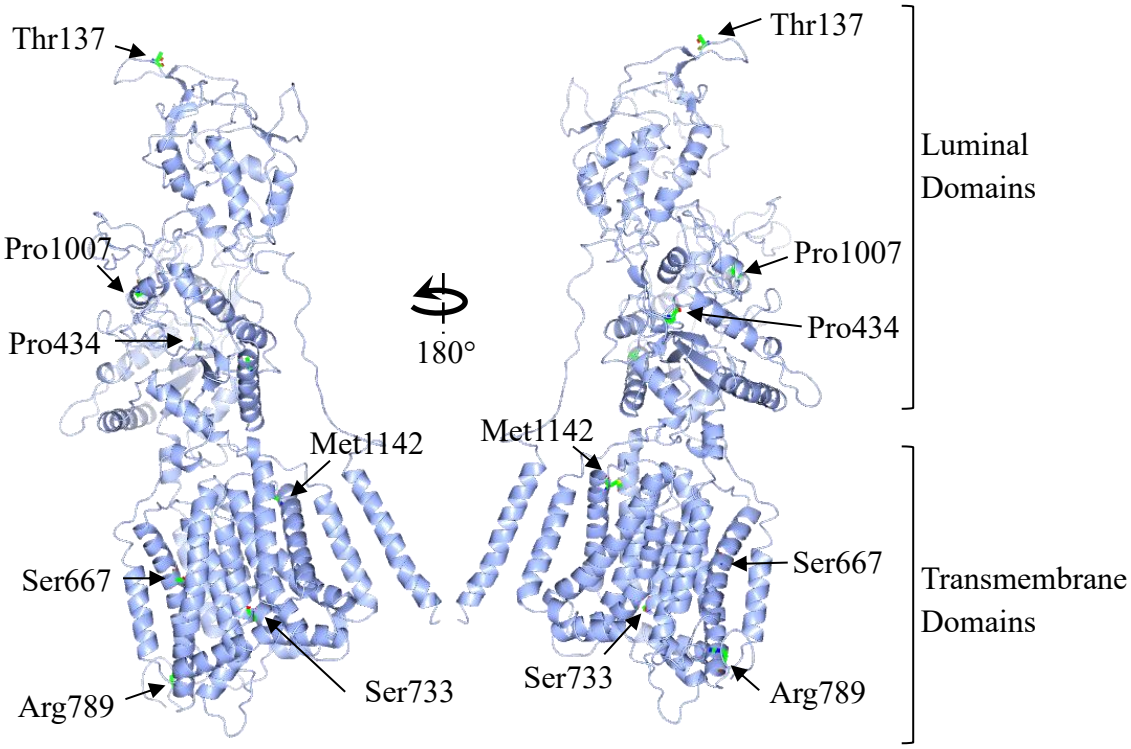

Figure 2.2: NPC1 mutations in CSF donors. Structure of full-length NPC1 protein in nanodisc as determined by electron microscopy (Qian *et. al.* 2020) was accessed from the Protein Data Bank (PDB:6W5R). Mutated residues mutated in NPC patient CSF samples are labelled and colored by atom type. Identification of protein domains was based on descriptions given by Trinh *et. al.* 2018. Image generated in CCP4MG version 2.10.11.

inferences can be drawn from previous studies and by examining which protein domains the mutations occurred in[17]. Patient NPC-2 was homozygous for the P1007A allele, which occurs in the luminal-facing C-terminal domain of NPC1. P1007A is the second most-common NPC1 mutation and is correlated with the "variant" form of NPC, which is characterized by mild alterations to cholesterol transport and typically results in mild adult-onset disease[5, 90]. The remaining four patients were heterozygous and had at least one mutated allele in the SSD, which typically results in limited NPC1 protein expression and more severe neurological outcomes[91]. Two patients (NPC-1 and NPC-5) carried the same mutations, S667L in the SSD and T137M at the site of cholesterol binding. Patient NPC-3 had a frameshift mutation in the SSD and a P434L

mutation in the middle luminal domain where NPC2 binds NPC1. NPC-4 had a mutation M1142 in the TMD and R789H in the SSD.

2.3b: CSF EV Enrichment and Characterization

To investigate the impact of NPC on CSF EVs, we first tested and validated methods to enrich for EVs from CSF. We based our protocol on our previous publications[92] and guidelines created by the International Society for Extracellular Vesicles (ISEV) and its CSF Task Force[26, 38, 64]. We used ultrafiltration to concentrate CSF, and size exclusion chromatography (SEC) to

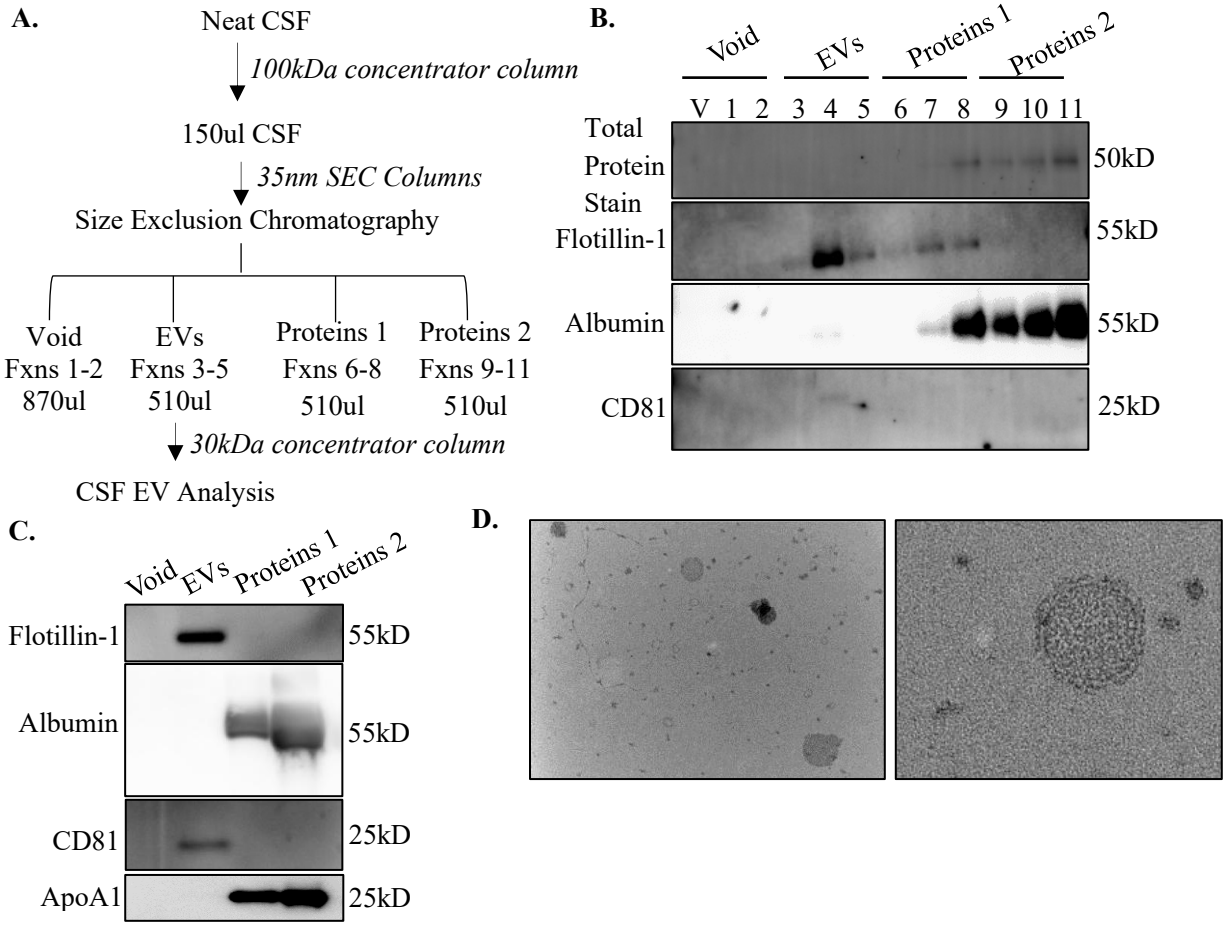

Figure 2.3: Size exclusion chromatography enriches for CSF EVs. A) Size exclusion chromatography (SEC) protocol. **B)** Immunoblot analysis of individual SEC fractions from a pool of control CSF showed enrichment for EV proteins Flotillin-1 and CD81 with minimal presence of non-EV proteins (albumin, total protein stain). **C)** Immunoblot of pooled SEC fractions from control CSF showed enrichment for EV proteins Flotillin-1 and CD81 with minimal presence of albumin and ApoA1 lipoprotein. **D)** Representative wide (left) and narrow (right) field of view transmission electron microscopy images of isolated EVs from NPC CSF.

separate EVs from other CSF content, such as proteins and lipoproteins (**Fig 2.3A**). Immunoblots confirmed that SEC fractions 3-5 were enriched for the EV proteins Flotillin-1 and CD81 with low levels of Albumin, a non-EV protein that is abundant in CSF (**Fig 2.3B**). Pooled fractions 3-5 again showed high levels of EV proteins Flotillin-1 and CD81 and low levels of albumin and the lipoprotein ApoA1 (**Fig 2.3C**). We then used transmission electron microscopy (TEM) to visually confirm that the pooled SEC EV preparation contained particles of approximately 100nm enclosed in a lipid bilayer (**Fig 2.3D**).

Two of our EV analysis techniques, direct stochastic optical reconstruction microscopy (dSTORM) and vesicle flow cytometry (VFC), include additional EV capture or labelling steps. These enabled us to use concentrated CSF rather than SEC purified EVs, which reduces experimental input volumes and conserves patient CSF (which is difficult to obtain in large volumes) (**Table 2.3**). Using ultrafiltration, we concentrated neat CSF 10-fold, 25-fold, 50-fold, and 75-fold and evaluated the effect on EVs by dSTORM imaging. EVs in concentrated CSF were then captured onto dSTORM imaging chips coated with antibodies against the canonical EV tetraspanins CD63, CD81, and CD9. We then used fluorescent antibodies against CD63 and CD81 to label EVs.

Table 2.3: CSF processing volumes by method. All volumes are listed in microliters.

EV Isolation/Enrichment Protocol ↓

	SEC EVs			10X Concentrated CSF			Neat CSF
	qPCR	MRPS	Immunoblot, TEM	dSTORM	VFC	MRPS	MBFC
Initial CSF	500	500	5000	100	100	100	150
Ultra-filtration (100kD)	150	150	150	10	10	10	NA
SEC Fraction	510	510	510	NA	NA	NA	NA
Ultra-filtration (30kD)	NA	NA	30	NA	NA	NA	NA
Final assay input	500	6	30	10	2.5	2	120

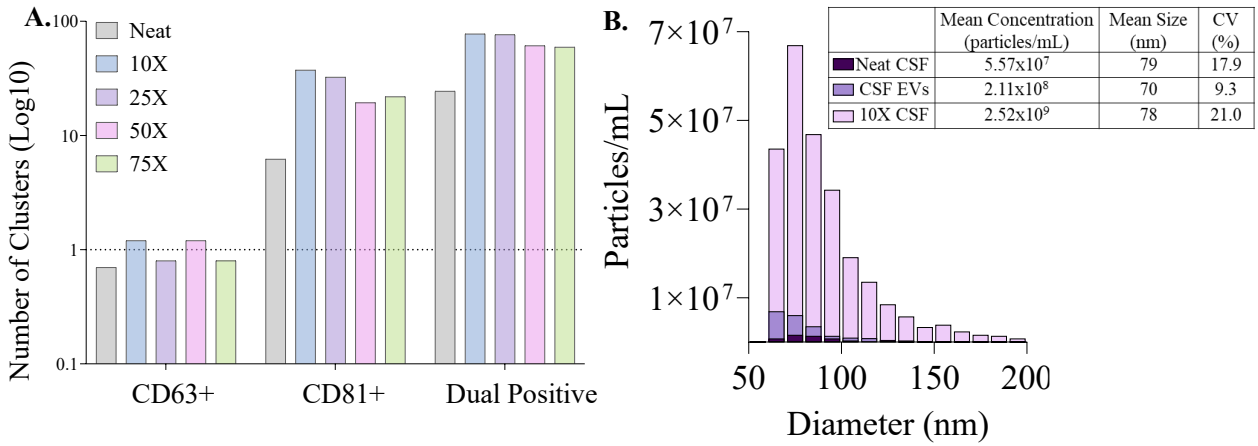

Figure 2.4: 10X CSF concentration enriches for CSF EVs. A) dSTORM imaging of unconcentrated (neat) CSF, and CSF concentrated 10, 25, 50, and 75X shows that 10X concentration allows for the detection of CD81-, CD63-, and double-positive EVs. Log10 cluster count is normalized to negative control (capture and detection antibodies alone), indicated by the dashed line. **B)** Histogram shows the distribution of particles present in neat CSF (dark purple), CSF EVs after SEC (medium purple), and 10X concentrated CSF. Particle count, size, and coefficient of variation are listed in the table below.

Our results showed that concentrating CSF 10-fold (10X CSF) resulted in robust tetraspanin signal relative to negative control (capture and imaging antibodies alone) (**Fig 2.4A**). Additional concentrations (25X, 50X, 75X) showed a limited increase or even loss in signal. We further used microchip resistive-pulse sensing (MRPS) to compare the distribution of particle size and concentration between neat CSF, CSF EVs after SEC, and 10X concentrated CSF (**Fig 2.4B**). 10X concentrated CSF contained ten-fold more particles/mL ($2.52x10^9$) than SEC-isolated CSF EVs ($2.11x10^8$), which in turn was ten-fold higher than neat CSF ($5.6x10^7$). All three preparations had a mean particle size between 70-80nm (**Fig 2.4B**). These data indicate that both our SEC and concentration protocols enrich for EVs from CSF samples.

2.3c: NPC CSF Contains a Higher Concentration of EVs Relative to Control CSF

There is conflicting evidence on whether NPC increases, decreases, or does not alter EV concentration and size[72, 73, 76-78]. Also, the size and concentration of EVs in NPC patient CSF has not yet been studied. Thus, we first used MRPS to measure the size and concentration of all particles present in 10X CSF from each sample (**Fig 2.5**). Our results show no significant difference in particle size or concentration between control and NPC CSF.

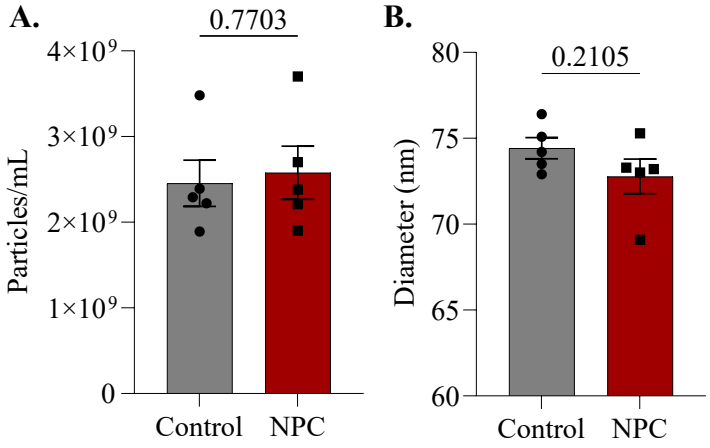

Figure 2.5: MRPS shows no change in concentration or size of CSF particles. A) No change was detected in the average concentration (particles/mL) of particles present in control CSF versus NPC. **B)** No change was detected in the mean particle diameter (nm) in control CSF versus NPC. Graphs represent the mean ± SEM of control (gray bars) and NPC (red bars) CSF. Symbols represent the average concentration or size of measured particles in each CSF sample. Data compared by Welch's t test.

As MRPS is only able to measure total particles, we next turned to VFC to distinguish between non-EV membranous particles and true EVs in concentrated CSF. In keeping with ISEV guidelines we first identified the optimal VFC staining protocols for CSF **(Supplementary Fig 2.2)**[66]. We then stained 10X concentrated CSF from individual control and NPC samples with *i)* a lipophilic membrane dye to label all membranous particles (**Fig 2.6A, B**), and *ii)* a pool of antibodies against the canonical tetraspanins (CD63/81/9) to label tetraspanin-positive particles (**Fig 2.6C, D**). Particles that are both membranous and tetraspanin positive are considered true EVs. Gating strategies and controls are described in **Supplementary Figures 2.3-2.5**.

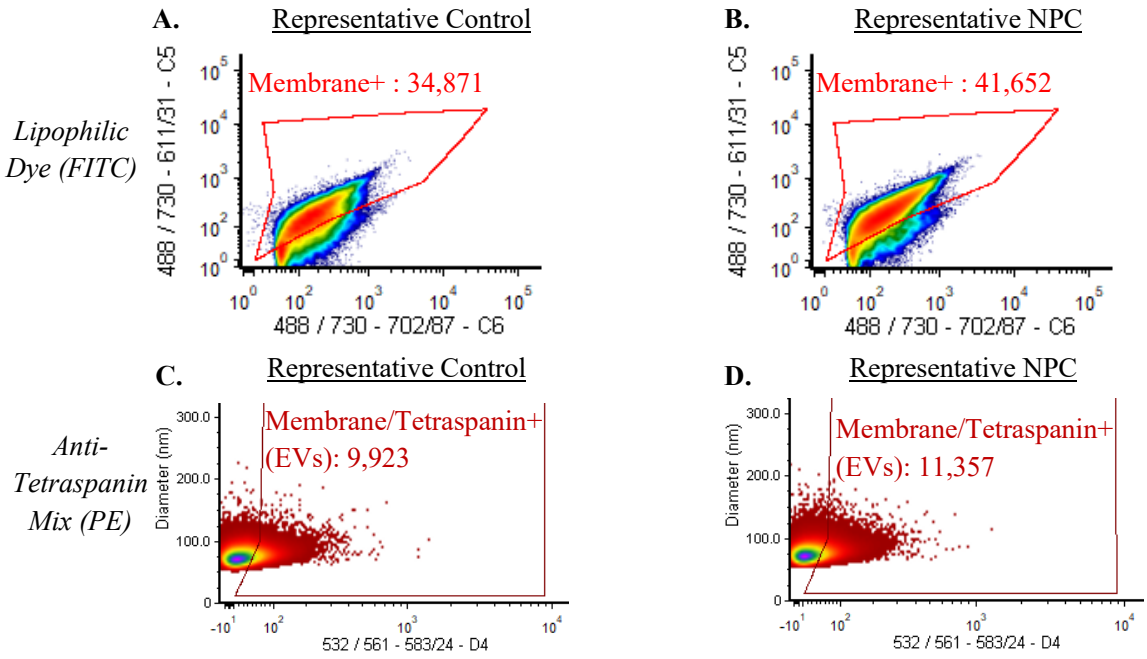

Fig 2.6: VFC gates of representative CTL and NPC CSF samples. A, B) Control (A) and NPC (B) CSF samples are stained with a lipophilic dye conjugated to fluorescein isothiocyanate (FITC). Plots show dye signal in the 488 channel. Gates depicted in bright red include all membranous particles and exclude background signal present in negative controls (unstained samples, stained buffer). Number of membranous particles in each gate is written in bright red. **C, D)** Control (C) and NPC (D) CSF samples are stained with anti-tetraspanin antibody conjugated to phycoerythrin (PE). Membranous particles gated in A and B are further gated by tetraspanin positivity. Plots show antibody signal in the 561 channel. Gates depicted in dark red include membranous and tetraspanin positive particles, and exclude background signal present in negative controls (unstained samples, stained buffer). The number of EVs in each gate is written in dark red.

In agreement with MRPS, our VFC results show no significant change in the concentration of total membranous particles between control and NPC CSF (**Fig 2.7A-B**).

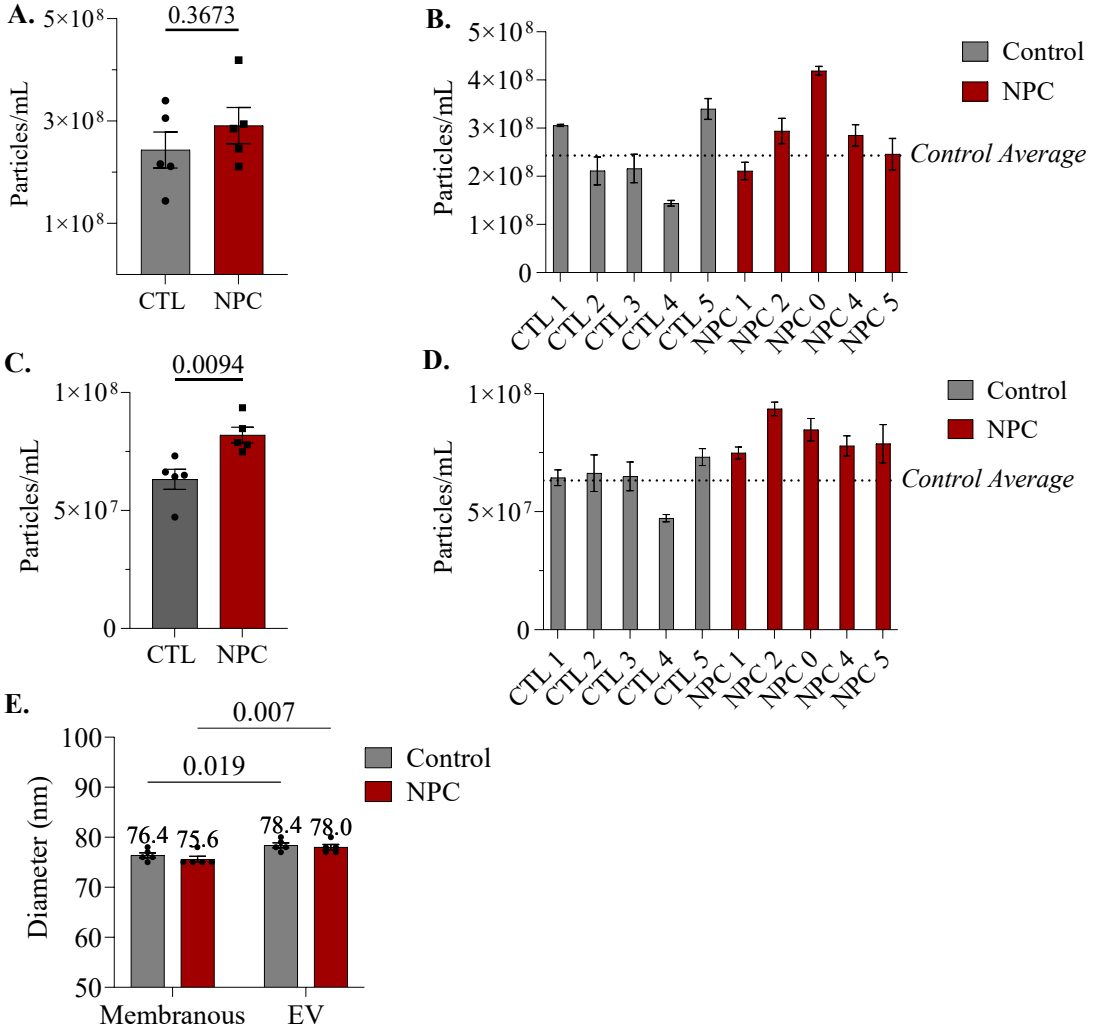

Figure 2.7: VFC shows increased EVs in NPC CSF. EVs from 10X concentrated control and NPC CSF samples were incubated with lipid membrane dye (FITC) and a combined antibody against CD9/CD81/CD63 (PE) **A)** There is no change in the total number of membrane positive particles in NPC (red) versus control (gray) CSF (Welch's t test). Symbols represent an n=3 technical replicates per sample; mean ± SEM of control and NPC are graphed. **B)** Concentration of membrane positive particles in each CSF sample. Bars show the mean concentration of three technical replicates per sample; error bars correspond to SEM. Dashed line represents average of all control samples. **C)** There is a significant increase in EV concentration in NPC (red) versus control (gray) CSF (Welch's t test). Symbols represent an n=3 technical replicates per sample; mean ± SEM of NPC and control samples are graphed. **D)** Concentration of EVs in each CSF sample. Bars show the mean concentration of three technical replicates per sample; error bars correspond to SEM. Dashed line represents average of all control samples. **E)** The median size of total membranous particles is significantly smaller than that of EVs (two-way ANOVA). There is no change in size between control (gray bars) and NPC (red bars) membranous particles or EVs. Symbols represent an n=3 technical replicates per sample; mean ± SEM of control and NPC are graphed. Median size of each population is shown above the bars.

However, there was a significant increase in tetraspanin-positive EVs present in the NPC samples relative to controls (**Fig 2.7C**). When analyzed individually, this increase was observed generally across all five NPC samples rather than being driven by a specific mutation (**Fig 2.7D**). The discrepancy between total membranous particles and tetraspanin positive EVs could be explained by a population of non-EV membranous particles, such as lipoproteins, which persist in concentrated CSF and does not vary between control and NPC individuals. As lipoproteins are typically smaller than true EVs, this hypothesis is supported by our finding that the size of total membranous particles was slightly but significantly smaller than the size of EVs (**Fig 2.7E**). There was no change in size between control and NPC membranous particles or EVs.

2.3d: EV Subpopulations Differ Between Control and NPC CSF

We next sought to examine whether the increase in EVs in NPC CSF was driven by expansion of a specific EV population or due to a global increase in all EVs. We chose to examine EV populations according to their positivity for the canonical tetraspanins (CD63, CD81, CD9) as we expected that all three proteins would be highly expressed in EVs from both NPC and control CSF. Additionally, tetraspanin positivity can inform the location of EV biogenesis and thus EV subclass. CD63 is localized to the endosome and primarily associated with exosomes; CD9 is localized to the plasma membrane and primarily associated with microvesicles; and CD81 is a cytoplasmic protein that can be found in either population[56, 93, 94].

To investigate, EVs from 10X concentrated CSF of control and NPC individuals were captured onto dSTORM imaging chips coated with anti-CD63, anti-CD9, and anti-CD81 antibodies. Chips were then labeled with fluorescent antibodies against CD63, CD81, and CD9. We then used dSTORM imaging to visualize and compare single positive EVs expressing only one tetraspanin (**Fig 2.8A)**, double positive EVs expressing two tetraspanins (**Fig 2.8B**), and

triple positive EVs expressing all three tetraspanins (**Fig 2.8C**). In both control and NPC CSF samples we found that CD9/CD81 double positives constituted the largest population of EVs, followed by triple positive EVs.

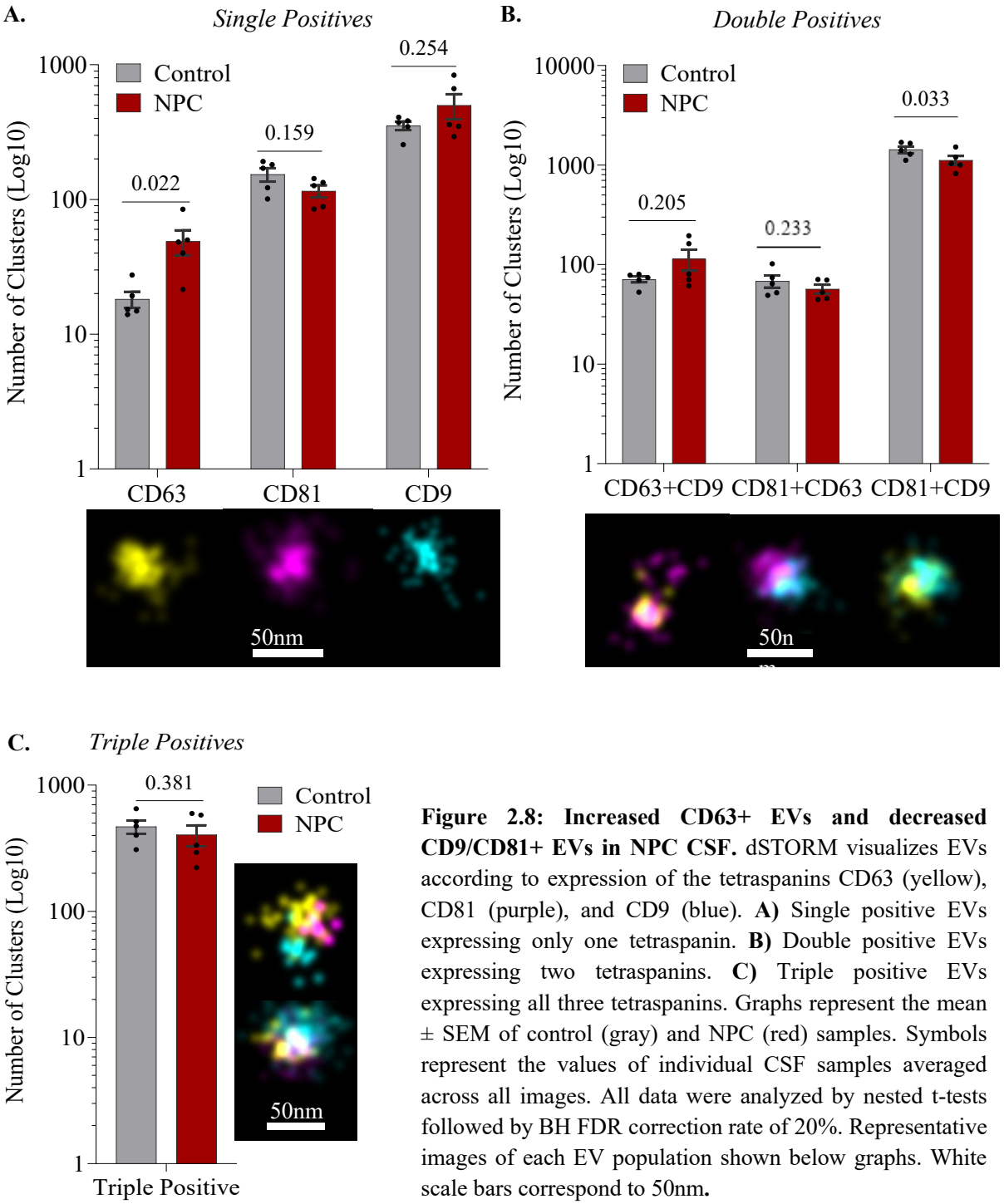

Figure 2.8: Increased CD63+ EVs and decreased CD9/CD81+ EVs in NPC CSF. dSTORM visualizes EVs according to expression of the tetraspanins CD63 (yellow), CD81 (purple), and CD9 (blue). **A)** Single positive EVs expressing only one tetraspanin. **B)** Double positive EVs expressing two tetraspanins. **C)** Triple positive EVs expressing all three tetraspanins. Graphs represent the mean ± SEM of control (gray) and NPC (red) samples. Symbols represent the values of individual CSF samples averaged across all images. All data were analyzed by nested t-tests followed by BH FDR correction rate of 20%. Representative images of each EV population shown below graphs. White scale bars correspond to 50nm.

Our dSTORM imaging results also identified two significant shifts in EV subpopulations between control and NPC CSF. In particular, NPC CSF contained a 2.6-fold increase in CD63 single positive EVs compared to controls (**Fig 2.8A, Supplementary Fig. S2.6A, B**), as well as significantly less CD9/CD81 double positive EVs (**Fig 2.8B, Supplementary Fig. S2.6C, D**). There was also a 1.7- and 1.5-fold increase in CD63/CD9 and CD9 EVs in NPC over control, although these changes were not statistically significant. Although not all population changes were significant, EV populations expressing CD81 tended to show decreases in NPC CSF versus controls, while all populations devoid of CD81 showed increases (**Fig 2.8)**.

As CD63 is generally a marker for endosomal EVs (exosomes) while CD9/CD81 double positive EVs typically originate at the plasma membrane (microvesicles), these results could indicate that NPC samples display a general shift towards EV production through endosomes rather than at the plasma membrane[93]. However, CD63-positive EVs and CD9/CD81-positive EVs were not correlated, suggesting that changes in these EV populations are at least somewhat

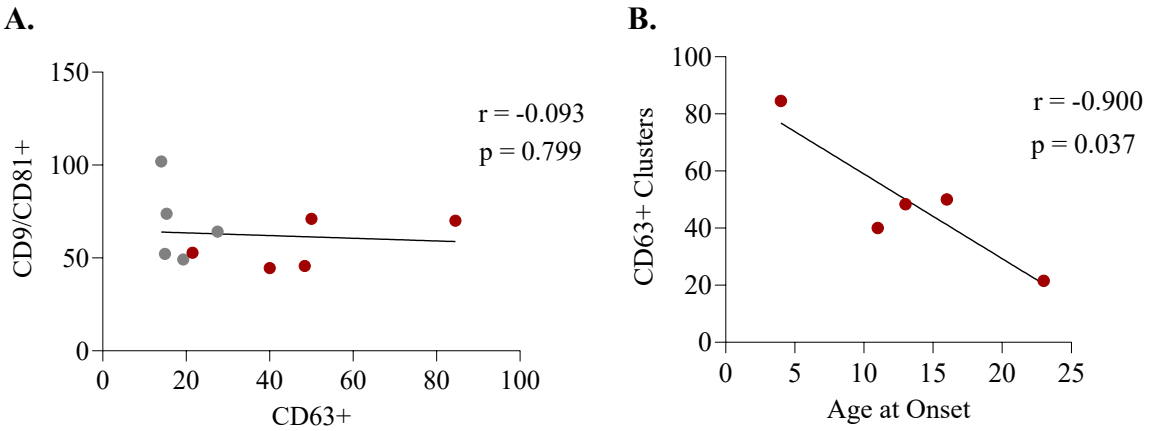

Figure 2.9: CD63+ EVs inversely correlate with NPC age of onset. A) Number of CD63+ EVs is not correlated with the number of CD9/CD81+ EVs (Pearson's test). **B)** Number of CD63+ EVs is inversely correlated with NPC age of onset (Pearson's test). Plotted symbols represent the mean EV count of individual control (gray) and NPC (red) CSF samples (averaged across all replicates). r and p-values from Pearson's correlation are listed (right). Black lines represent simple linear regression.

independent (**Fig 2.9A**). Interestingly, CD63-positive EVs inversely correlated with NPC age of onset, such that more CD63+ EVs were found in patients that showed symptoms earlier in life (**Fig 2.9B**). No clinical correlations were found with CD9/CD81 EVs (data not shown). These results suggest that the increase in CD63-positive EVs in NPC CSF is clinically significant.

2.3e: NPC CSF EVs are Enriched in Lamp1

To further define EV populations in NPC we further probed the surface markers of EVs from NPC and control CSF. We used a multiplexed bead-based flow cytometry (MBFC) panel consisting of 37 markers known to be highly expressed in human brains and commonly found on EVs to compare the relative abundance of EV types in NPC and control CSF. Of these 37 markers, 32 were expressed above background in at least eight of ten CSF samples (**Fig 2.10A**). Lysosomal-associated protein 1 (Lamp1) showed a statistically significant two-fold increase in NPC EVs over controls, although this result did not survive multiple comparisons correction (**Fig 2.10A, B**). Another protein in the same family, lysosomal-associated protein 4 (Lamp4, also known as CD68), had the largest fold-change in NPC over controls. Fold changes and significance values for all expressed proteins are described in **Supplemental Table 2.1**. Lamp1 did not correlate with any clinical data (**Supplemental Table 2.2**).

Previous studies have found elevated Lamp1 in NPC tissues[75, 76, 95]. Additionally, like CD63 (which is also known as Lamp3), Lamp1 is often used to identify EVs of endosomal origin[93]. To further investigate the potential increase in Lamp1-positive EVs in NPC CSF, we again turned to VFC. CSF samples from NPC and control individuals were combined to create one control and one NPC pool. Pooled CSF was then concentrated 10X and incubated with a FITC-conjugated membrane dye and PE-conjugated antibody against Lamp1. Sample dilution, representative gates, and gating strategies are described in **Supplemental Figs S2.7-2.8**. Only a

small percentage of membranous particles stained positive for Lamp1 (**Fig 2.10D**). However, in agreement with our MBFC findings, there was significant increase in Lamp1 positive EVs in NPC CSF relative to controls (**Fig 2.10D**). Additionally, Lamp1-positive EVs in NPC CSF were significantly smaller than Lamp1-positive EVs in control CSF (**Fig. 2.10E**). Together, these

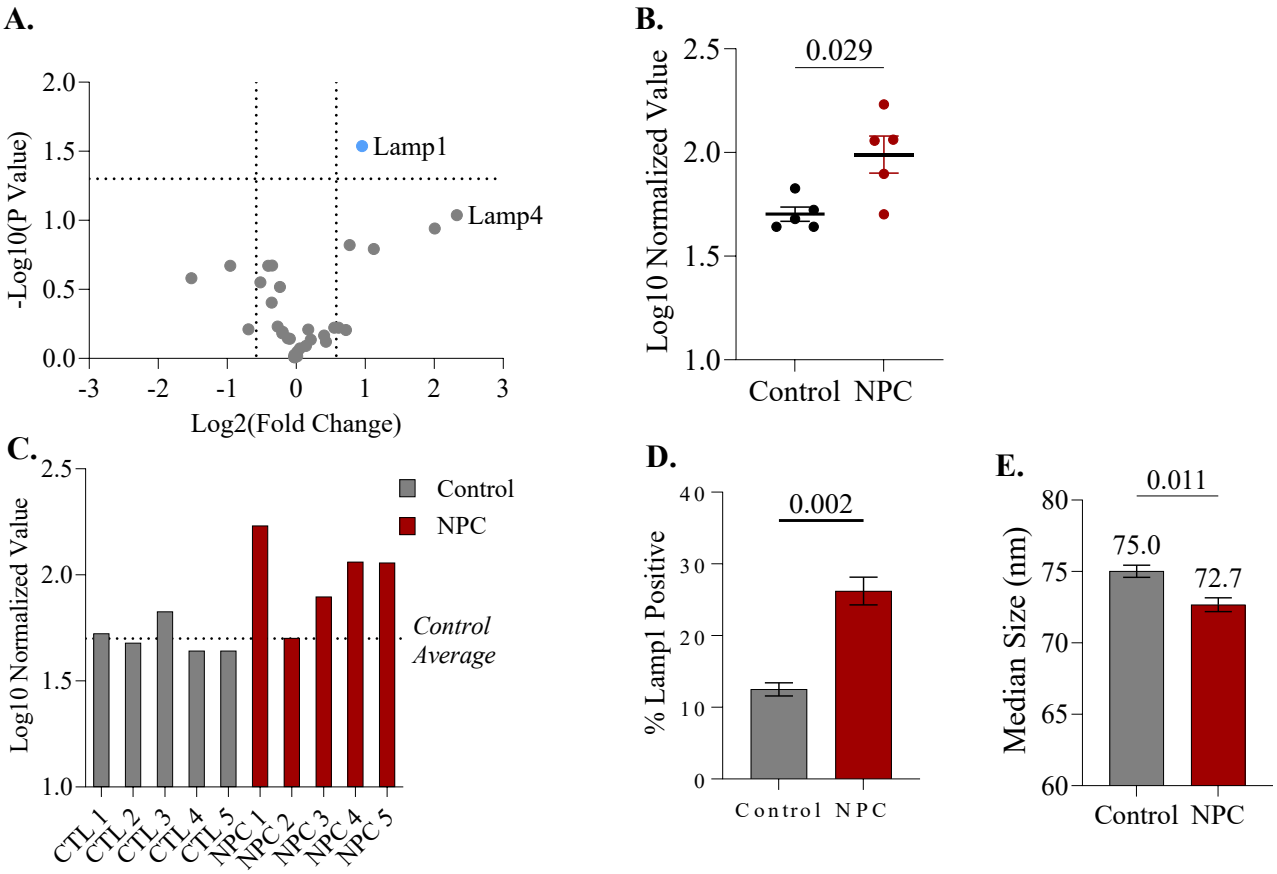

Figure 2.10: Lamp1 is enriched on the surface of NPC CSF EVs. A) Expression of 37 different proteins was compared between NPC and control EVs from individual CSF samples. Plot represents uncorrected Welch's t test; dashed lines represent thresholds for statistical significance ($P<0.05$) and meaningful fold changes. Light blue dots indicate significantly upregulated proteins. **B)** Quantification of Lamp1 EV expression. Symbols represent normalized value of individual CSF samples; bars represent the mean ± SEM. **C)** Lamp1 expression in individual CSF samples. Dashed line corresponds to the mean expression of all control samples. **D)** VFC shows NPC CSF (red) contains a greater percentage of Lamp1 positive EVs compared to controls (gray) (Welch's t test). Control and NPC groups represent pools of individuals. **E)** The median size of Lamp1 positive EVs is significantly smaller in NPC (red) relative to controls (gray) (Welch's t test). Bars represent the mean ± SEM of four technical replicates. Median size of each population is shown above the bars.

results indicate that there is a significant increase in Lamp1-positive EVs in NPC CSF, further supporting an increase in endosomal EVs in NPC.

2.3f: MiRNAs are Differentially Expressed in NPC and Control CSF EVs

We next sought to determine whether miRNA cargo was differentially expressed in NPC CSF EVs. First, we performed a pilot study on control and NPC CSF to identify miRNAs of interest. Control and NPC samples were combined to create one pool of control CSF and one pool of NPC CSF. EVs were isolated from each pool using SEC and total RNA was extracted. Next, we analyzed the CSF EV samples using premade qPCR arrays that contained probes against 754 miRNAs most commonly expressed in humans. From this screen, we selected 187 miRNAs that were expressed in our CSF EVs and/or have been previously implicated in NPC (**Fig 2.11A**). We then created a custom qPCR miRNA array to measure expression of these 187

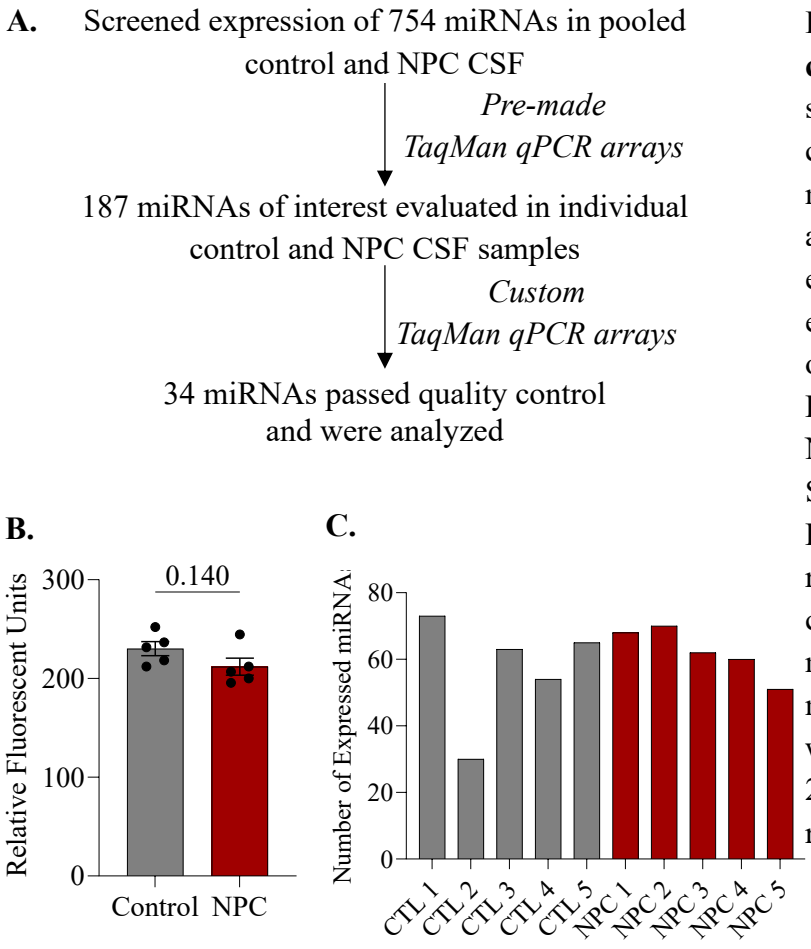

Figure 2.11: qPCR on NPC and control CSF EVs. A) Progressive screening with pre-made and custom qPCR arrays identified 34 miRNAs expressed in both control and NPC CSF EVs, which were evaluated for differential expression. **B)** No differences observed in the total amount of RNA isolated from control and NPC and samples (Welch's t test). Symbols represent the amount of RNA isolated per sample; bars represent the mean ± SEM of control and NPC. **C)** Number of miRNAs that passed quality control metrics in each CSF EV sample and were considered expressed. Control 2 showed low expression even after repeating qPCR.

miRNAs in duplicate. Next, we isolated EVs from each control and NPC CSF sample individually. RNA was extracted and miRNA expression was measured using our custom qPCR array. No difference was observed in the total amount of RNA extracted from control and NPC EVs (**Fig 2.11B**). Control 2 showed generally poor miRNA amplification, even after repeating the assay, and was thus removed from further analysis (**Fig 2.11C**). This finding was likely due to high red blood cell contamination in Control 2, which was noted during CSF collection and likely negatively affected the RNA isolation outcome.

Of the 187 miRNAs assayed by our custom qPCR array, 34 passed our quality control metrics and were analyzed further. Fold changes and significance values were used to compare miRNA expression in control and NPC CSF EVs (**Fig 2.12A**). We identified two miRNAs, 199a/b-3p and 320a, that were significantly upregulated in NPC EVs as compared to controls after correcting for multiple comparisons (**Fig 2.12B-E**). Two miRNAs, let-7g-5p and 885-5p, were also significantly upregulated in NPC EVs versus controls but failed multiple comparisons correction (**Fig 2.12F-G**). None of the differentially expressed miRNAs (199a/b-3p, 320a, let-7g-5p or 885-5p) were correlated with NPC clinical data (**Supplemental Table 2.3**).

We next investigated what pathways and diseases the differentially expressed NPC miRNAs may be implicated in. We focused on miR-320a and miR-199a/b-3p as our top candidates and identified the mRNAs that they target or are predicted to target. The online database miRTarBase identified 762 mRNA targets of miR-320a and/or miR-199a-3p that have been experimentally validated (**Fig 2.13A**)[96]. The online tools TargetScan[97] and miRDB[98] identified 902 mRNAs that miR-320a and/or miR-199a/b-3p are predicted to target, 274 of which overlapped with mRNAs identified by miRTarBase. The resulting 1,390 validated or

predicted mRNA targets of miR-320a and/or miR-199a/b-3p were used in Ingenuity Pathway Analysis (IPA) to identify the canonical pathways and diseases.

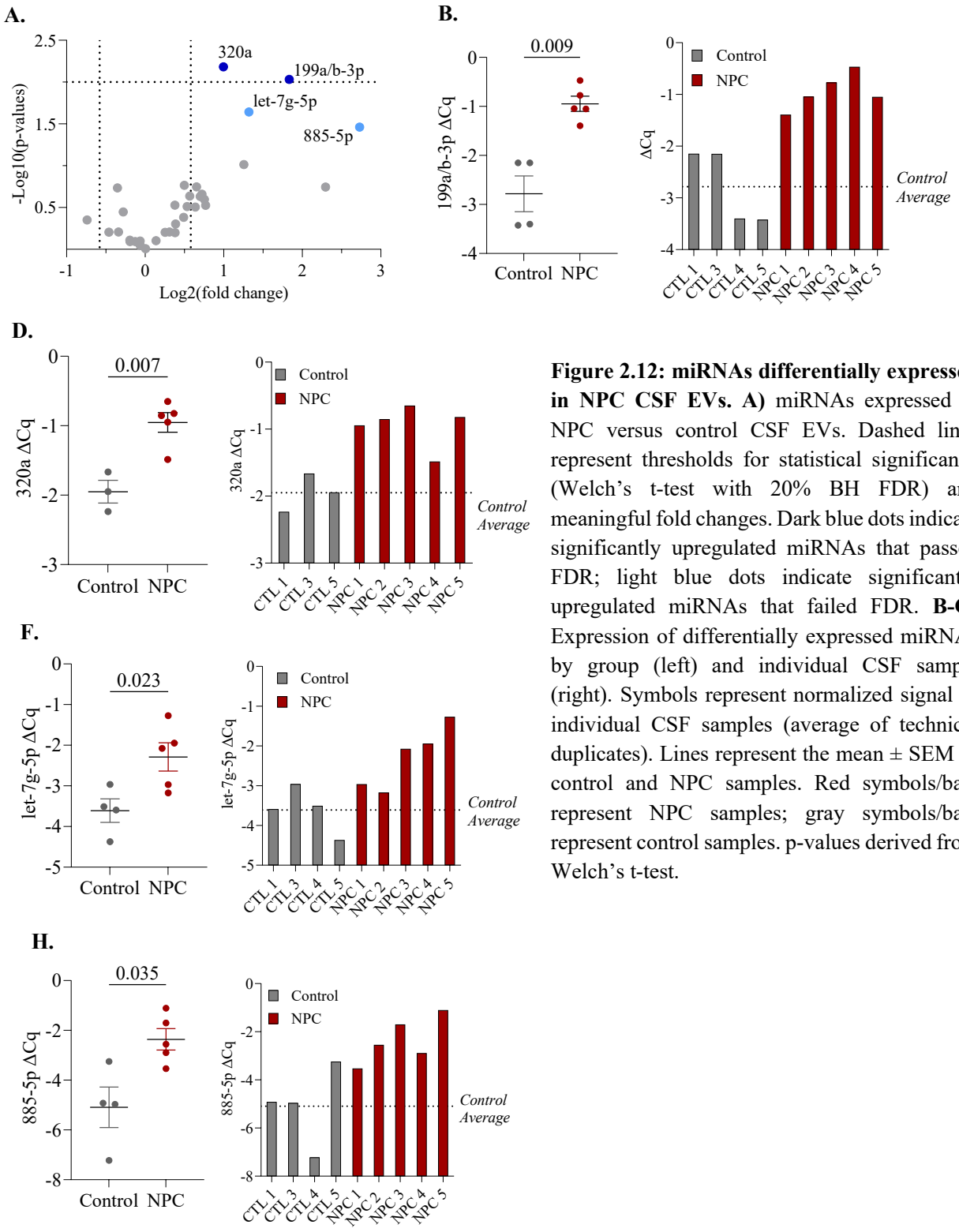

Figure 2.12: miRNAs differentially expressed in NPC CSF EVs. A) miRNAs expressed in NPC versus control CSF EVs. Dashed lines represent thresholds for statistical significance (Welch's t-test with 20% BH FDR) and meaningful fold changes. Dark blue dots indicate significantly upregulated miRNAs that passed FDR; light blue dots indicate significantly upregulated miRNAs that failed FDR. **B-G)** Expression of differentially expressed miRNAs by group (left) and individual CSF sample (right). Symbols represent normalized signal of individual CSF samples (average of technical duplicates). Lines represent the mean ± SEM of control and NPC samples. Red symbols/bars represent NPC samples; gray symbols/bars represent control samples. p-values derived from Welch's t-test.

for these mRNAs. IPA identified 357 canonical pathways and 70 diseases, which were then ranked according to the Benjamin-Hochberg (BH) corrected p-value. The top 3 overall diseases were organismal abnormality, hereditary disorder, and neurological disease, all of which are related to NPC (**Fig 2.13B**). Similarly, the top canonical pathways included oxidative stress, mTOR signaling, and autophagy, all of which are elements are NPC cellular pathology (**Fig 2.13C**). Together, these results demonstrate that NPC CSF EVs contain differentially expressed miRNAs that regulate mRNA translation and protein expression in pathways relevant to NPC disease biology.

A.

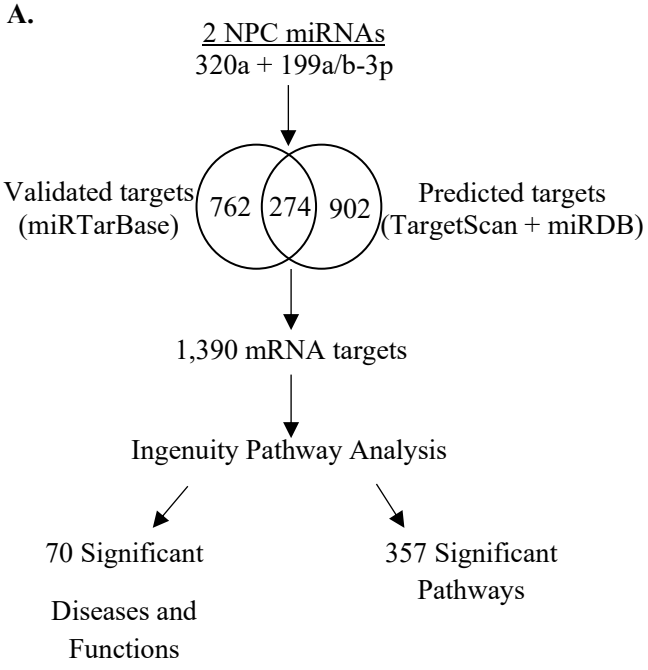

B.

Top Relevant Pathways	-log(BH p-value)
Oxidative Stress Induced Senescence	8.72
NGF Signaling	6.81
mTOR Signaling	6.66
miRNA Biogenesis Signaling	6.20
Senescence	5.94
Autophagy	5.80

C.

Top Diseases	-log(BH p-value)
Organismal Abnormality	21.68
Hereditary Disorder	18.14
Neurological Disease	18.14

Fig 2.13: Pathway analysis of differentially expressed NPC miRNAs. A) miRTarBase, TargetScan, and miRDB identify validated and predicted mRNA targets of differentially expressed miRNAs. Ingenuity pathway analysis reveals the top diseases and pathways the mRNAs are active in. **B)** mRNA targets were significantly enriched in 357 pathways, which were then ranked according to their BH-corrected p-value. The top six enriched pathways relevant to NPC are displayed. **C)** mRNA targets were significantly enriched in 70 diseases and functions, which were then ranked according to their BH-corrected p-value. The top three diseases relevant to NPC are displayed.

2.4: Discussion

These studies are the first to demonstrate changes to EV concentration and cargo in CSF from NPC patients. As is common for rare disease research, we were only able to obtain a very low number of CSF samples: five healthy donors and five NPC patients. Our NPC patients also carried different *NPC1* mutations and displayed heterogeneity in their clinical presentation. Whether our findings would replicate in a larger cohort of patients remains to be seen.

Additionally, all of the NPC patients were undergoing treatment with the experimental drug CD, while the healthy donors were not. Thus, it is impossible to know at this stage whether our results are driven by NPC pathology or are an effect of CD treatment. However, none of our significant findings correlated to the amount of time NPC patients had been on CD, suggesting that these results are not being driven by CD treatment (**Supplementary Tables S2.2, 2.3**). Previous studies in *NPC1* null mice showed that CD treatment does not alter EV release, and CD does not alter EV cholesterol content in *NPC1* KO cell lines[80, 99]. However, to fully disentangle the effect of NPC and CD treatment on EVs, experiments on CD-treated and untreated NPC samples – ideally from patients – will be needed.

We noted that patient age of onset and NPC-SS scores were not correlated in our cohort. NPC-SS assesses the extent of pathology (in the categories ambulation, swallow, cognition, speech, and fine motor skills) at the time of CSF collection and these could have been impacted by the patients' current treatment plans or supportive care, while age of onset is a general predictor of disease severity and rate of progression over the lifespan. It was interesting that CD63-positive EVs, which are formed in the endosome, inversely correlated with age of onset (**Fig. 2.9B**) but not with NPC-SS. This may suggest that the increase in CD63 EVs is driven by

biochemical changes in endosomes caused by NPC1 mutations, rather than as an effect of current symptom severity.

Our VFC data shows that there is increased EV concentration in NPC patient CSF as compared to healthy controls (**Fig. 2.7C, D**). This is in agreement with data in patient and mouse fibroblasts as well as *NPC1* knockdown in oligodendrocyte and neuronal cell types[72-74]; but in contrast with data on NPC rodent astrocyte and choroid plexus models, which showed decreased EV release[75, 76], and with data on immortalized cell lines that show no change in EV release following NPC1 inhibition[77, 78]. These discrepancies could indicate that the relationship between NPC1 and EV release is dependent on species and/or cell type. Interestingly, our results agree with the only other study to include human NPC samples[72].

However, it is important to consider that measurements of EV concentrations are highly influenced by the method of EV isolation and analysis[40]. Indeed, the previous studies on EV concentration in NPC used a range of isolation and measurement techniques, which could contribute to the disparate findings. This is an unfortunate finding in many published CSF EV studies, for which protocols are largely inconsistent at this point in time[64]. In our studies, measuring EVs by MRPS – a broad technique that can only size and count total particles – showed no significant changes between control and NPC samples (**Fig. 2.7A, B)**. Yet analysis by VFC, which is able to specifically identify tetraspanin-positive EVs, showed a significant increase in NPC EVs (**Fig. 2.7C, D**). Importantly, our VFC EV counting method was based on the presence of a lipophilic dye that fluoresces after intercalating into lipid bilayers. Soto-Heulin *et. al.* demonstrated that NPC EVs have an elevated lipid content compared to controls, including significant enrichment for hexosylceramide and lysophosphatidylcholine[51]. It is thus possible that lipid-based EV counting methods, such as our VFC pipeline, are biased by altered lipid

enrichment in NPC EVs. These considerations underline the challenges in measuring EV concentration and suggest that results should be interpreted with caution.

In addition to broadly elevated EV concentrations in NPC CSF, we also identified a specific increase in EV populations that expressed only the CD63 tetraspanin, and a decrease in EVs expressing both CD9 and CD81 (**Fig. 2.8A, B**). While all three tetraspanins have been commonly used as broad markers for small EVs (which some mistakenly refer to as exosomes), recent evidence suggests that CD9, CD63, and CD81 label distinct populations of EVs and play unique roles in EV formation and cargo packaging[94]. In particular, CD63 is primarily expressed on endosomal membranes and has been shown to preferentially label endosome-derived EVs, or exosomes; similarly, CD9 is primarily expressed on plasma membranes and preferentially labels membrane-derived microvesicles[56, 93]. CD81 is a cytoplasmic protein, although it appears to behave more similarly to CD9 than CD63. Thus, in our data, the increase in CD63+ EVs and decrease in CD9-CD81+ EVs suggests that NPC CSF may be enriched in exosomes of endosomal origin.

The increased expression of NPC CSF EV Lamp1 (**Fig. 2.10**), a protein found on late endosomes and lysosomes, further supports the hypothesis that exosomes are enriched in NPC CSF. Previous studies have shown increased Lamp1 in neural cell cultures or brain tissue from NPC rodent models, which in some cases appears hyperglycosylated[75, 76, 95]. Our detection method is not able to determine glycosylation state, and further studies are needed to determine if NPC CSF EV Lamp1 is alternatively glycosylated. Interestingly, a study in four NPC patients and four healthy controls found elevated Lamp1 in NPC cerebellar tissues, but no change in CSF Lamp1[95]. This could indicate that increased Lamp1 in NPC CSF is specific to EVs.

There is also conflicting evidence on whether CD treatment influences Lamp1 expression in NPC. Using human fibroblasts, one study reported that Lamp1 expression is elevated in NPC fibroblasts only after treatment with CD[100]. In contrast, Cawley *et. al.* reported that CD decreases Lamp1 expression in mouse brain tissues[95]. Neither study investigated the effect of CD on the Lamp1 content of NPC EVs. Thus, further research is needed to determine if the alterations to NPC CSF EV Lamp1 we identified are due to NPC pathology or CD treatment.

Finally, we found that NPC CSF EVs show increased expression of miRs-320a and -199a/b-3p, as well as a trending increase in let-7g-5p and miR-885-5p (**Fig. 2.12**). Interestingly, miRs-320a and -199a-3p play known roles in cholesterol homeostasis[101, 102], and -885-5p is elevated in patients with liver pathologies, which are also common to NPC[103]. Other studies have investigated miRNA changes in an NPC patient fibroblast cell line and spleen tissue of an NPC mouse model [87, 88]. However, the differentially expressed miRNAs identified in these studies shared no overlap with our cohort. These findings underline the tissue specificity of miRNA expression.

Together, these studies add to a growing body of evidence that EVs are fundamentally altered in NPC, including changes to concentration, subtype, surface proteins and miRNA cargo. They are the first studies to examine EVs in human NPC samples, as well as CSF from any NPC source. Thus, further examination of the role of EVs in NPC could elucidate novel disease mechanisms, as well as identify future therapeutic targets or disease biomarkers.

2.5: Materials and Methods

2.5a: Study Participants

CSF from NPC donors 1, 3, 4, and 5 was generously shared by Dr. Elizabeth Berry-Kravis from patients participating in an expanded access program at Rush University Medical Center (RUMC)[104, 105]. CSF from NPC donor 2 was generously shared by Dr. Joseph Quinn at the Oregon Health and Science University (OHSU). CSF from control donors was generously shared by Dr. Elaine Peskind at the University of Washington (UW) from a cohort of veterans participating in an ongoing longitudinal multimodal assessment[106]. Institutional Review Board approval was obtained from RUMC, OHSU, Veterans Affairs Puget Sound Health Care System and UW, as applicable. Written informed consent by parents and assent from developmentally appropriate participants was obtained; patients older than 18 years consented for themselves when applicable. Participants at all locations underwent detailed evaluations consisting of medical history, physical and neurological examinations, laboratory tests, and neuropsychological assessments. We certify that the study was performed in accordance with the ethical standards as laid down in the 1964 Declaration of Helsinki and its later amendments[107].

2.5b: CSF Collection and Storage

CSF was collected through a minimally invasive lumbar puncture as previously described[108, 109]. CSF was aliquoted and frozen on dry ice at the bedside, then stored at -80°C. CSF samples were transported on dry ice to OHSU, and each sample aliquoted again to minimize freeze-thaw cycles. CSF was then stored at -80°C until use in these experiments.

2.5c: CSF Concentration

Immediately prior to use, CSF samples were removed from -80°C and thawed on ice. Up to 5mLs of CSF was applied to 100kD concentrator columns (Millipore-Sigma MPE100025) in 500µl increments and centrifuged at 14,000xg at 4°C until desired concentrate volume was

reached. The concentrator column was then flipped over, and CSF was collected into fresh microcentrifuge tubes by centrifuging at 2,000xg for 5 minutes. Phosphate-buffered saline (PBS) was added to achieve the final volume. Initial and final volumes of CSF varied by downstream application (see **Table 2.3**).

2.5d: CSF EV Enrichment

Enrichment for CSF EVs was performed using SEC. CSF samples were concentrated as described above to a final volume of 150µl. SEC was performed using Single 35nm Gen2 columns (Izon Science ICS-35) for SEC. Prior to use, SEC columns were brought to room temperature and washed with PBS, according to the manufacturer's instructions. To begin SEC, 150µl of concentrated CSF was applied to the column and allowed to enter the frit. Next, 870µl of PBS was applied to the column and collected as the void fraction; then, 510µl of PBS was applied to the column iteratively to collect the EV and protein fractions. Following collection, the fractions were stored on ice until use. If necessary, the EV fraction was further concentrated using 30kD concentrator columns spun at 14,000xg until desired volume was reached (Millipore-Sigma MRCFOR030).

2.5e: Immunoblots

Protein concentrations were measured using the Qubit protein assay kit and Qubit 4 fluorometer (Thermo Fisher Scientific; TFS). Gel electrophoresis was performed using 4-12% Bis-Tris gels run at 125V at room temperature in MOPS buffer. Proteins were transferred to PVDF membranes (Millipore) in NuPage transfer buffer (Invitrogen) with 10% methanol for 2 hours at 100V at 4°C. PVDF membranes were stained with a total protein stain (TFS) according to the manufacturer's instructions and blocked for 1 hour in 5% milk in 1XTBS with 0.05% Tween-20 (TBST). Membranes were incubated in primary antibodies overnight at 4°C, then

washed 4 times with 0.1% TBST and stained with secondary antibodies for 1 hour at room temperature (RT). All antibody incubations and washes were performed in 1XTBS with 0.5% Tween-20. After secondary incubations membranes were incubated for five minutes in Pico, Femto, or Atto chemiluminescence dyes (TFS) and imaged using the ChemiDoc Touch Imaging System (Bio-Rad). The following antibodies were used: Albumin 1:1,000 (#4929, Cell Signaling Technology); ApoA1 (12C8) 1:200 (sc-080551, Santa Cruz Biotechnology); CD63 (H5C6) 1:5,000 (556019, BD Biosciences); CD81 (B-11) 1:100 (sc-166029, Santa Cruz Biotechnology); and Flotillin-1 1:10,000 (ab133497, Abcam). Secondary antibodies were purchased from Jackson ImmunoResearch and included horseradish peroxidase (HRP)–conjugated donkey anti-mouse (715-035-150), donkey anti-rabbit (711-035-152), and donkey anti-goat (705-035-003); all secondaries were used at 1:10,000.

2.5f: Transmission Electron Microscopy

Pooled SEC EV fractions from a representative NPC CSF sample were concentrated and delivered on wet ice to the OHSU Multiscale Microscopy Core for preparation and imaging. Five µl of EVs were deposited on glow-discharged (120s 15mAmp, negative mode) carbon formvar 400 mesh copper grids (01822-F, Ted Pella, Inc.) for 3 minutes, rinsed for 15 seconds in water, wicked on Whatman filter paper 1, stained for 60 seconds in filtered 1.33% (w/v) uranyl acetate in water, wicked again, and air dried. Samples were then imaged by using the Multiscale Microscopy Core at 120 kV on a FEI Tecnai™ Spirit TEM system (TFS). Images were acquired as 2048 × 2048 pixel, 16-bit gray scale files using the FEI's TEM Imaging & Analysis interface on an Eagle™ 2K CCD multiscan camera.

2.5g: Microchip Resistive Pulse Sensing

MRPS was performed using the nCS1™ Particle Analyzer and C-400 microchips (Spectradyne Particle Analysis). Prior to use the instrument was primed with 1X PBS without calcium and magnesium containing 1% Tween-20 (running buffer) using the supplied cleaning cartridges cleaning cartridges and lines were flushed. For analysis, neat CSF, 10X CSF, or CSF EVs were diluted 1:4 in running buffer and run on the nCS1. At least 500 particles were collected per sample.

Data was analyzed using the nCS1 Data Viewer software, version 2.5.0.325. To control for variation in microchip lots, 150 nm calibration beads of known concentration were run alongside samples in C-400 microchips of matching lots. Discrepancies between actual and measured size and concentration of the calibration beads were used to generate correction factors that were applied to each sample. To generate histograms of particle size and concentration, samples were background-subtracted and scaled to their respective correction factors. The gaussian distribution of particle concentration and size was obtained. Particles over 200nm were excluded from analysis.

2.5h: Direct Stochastic Optical Reconstruction Microscopy

dSTORM imaging was performed using commercially available kits according to the manufacturer's instructions (Oxford Nano Imaging (ONI), EV Profiler 2 Kit). Chips containing four imaging lanes each were coated with antibodies against CD63, CD9, and CD81. Ten µL of neat CSF or CSF concentrated to 10X, 25X, 50X, or 75X were applied to each imaging lane for EV capture. Chips were incubated overnight at 4°C while slowly rocking. All steps were performed in a humidity chamber in the dark.

Following EV capture, chips were washed and incubated with fluorophore-conjugated detection antibodies against CD81 (647), CD81 (561), and CD9 (488) (ONI). Imaging was performed on an ONI using CODI Acquisition settings. All lasers were set to 40% power. Channel mapping was performed daily using calibration chips coated with fluorescent beads (ONI). Ten fields of view (FOVs) were captured per sample, at 1,000 frames per FOV. Each run included platelet EVs as a positive control and capture and detection antibodies alone (no CSF) as a negative control.

The CODI EV Profiling Application used for image analysis (ONI). Visual inspection and an outlier test of total signal was used to remove FOVs that contained bubbles or uneven staining. Analysis settings to identify clusters (EVs) are described in **Table 2.4**. To compare between samples, the cluster count for each EV population (single/double/triple positives) was averaged across all FOVs.

Table 2.4: dSTORM imaging analysis parameters.

	647	**561**	**488**
Drift Correction	Drift at minimum entropy (DME)		
Frame Index (x1000)	0-1	1-2	2-3
Photon count	500-3000	150-3k	150-5000
Sigma (nm)	50-300	50-300	50-300
P Value	0-0.2		
Localization precision (nm)	0-20		
Clustering	DBSCAN (40nm)		
Area (nm^2)	100-10,000		
Circularity	0.7-1		
Radius of gyration (nm)	10-100		
Density (per nm^2)	0-0.1		
CD81 counts	2-1000		
CD63 counts		1-1000	
CD9 counts			2-1000

2.5i: Vesicle Flow Cytometry

EV concentration, size, and tetraspanin or Lamp1 expression was measured by VFC using commercially available kits (vFC Assay Kit, Cellarcus Biosciences). 10X concentrated CSF was incubated at a final concentration of 1:10 with a lipophilic membrane dye pre-diluted 1:10 (vFred) and PE-conjugated anti-tetraspanin (CD63/CD81/CD9) antibody pre-diluted 1:4 for 1 hour at 27°C. Samples were then diluted in buffer to a final dilution of 1:125 (tetraspanin measurements) or 1:150 (Lamp1 measurements) and analyzed in an Amnis CellStream flow cytometer (Cytek) using small particle detection mode. Spectral compensation was performed using stained antibody capture beads and validated by single-stain controls. Events were recorded for 120 seconds. Forward and side scatter lasers were set to zero; remaining lasers were set to 100. All samples were run in triplicate wells. As negative controls each run included unstained samples, membrane-dye only samples, and samples with lysis buffer. As positive controls each run included platelet-derived EVs and synthetic 100nm lipo-beads (Cellarcus Biosciences).

Data analysis was performed using FCS Express 7 Research Edition and templates provided by Cellarcus Biosciences. A summary of analysis settings and gating strategies is provided in **Supplemental Figs S2.3-2.5, S2.7**, and **S2.8**.

2.5j: Multiplexed Bead-Based Flow Cytometry

MBFC was performed using commercially available kits and reagents according to the manufacturer's instructions (Miltenyi Bioscience MacsPlex EV Human Neuro kit). Prior to MBFC analysis CSF aliquots were thawed on ice and centrifuged at 4°C for 10 minutes at 400xg. Supernatant was collected and centrifuged at 4°C for 10 minutes at 2,000xg. 120µL of the supernatant was transferred to a new tube and incubated with antigen-coated capture beads

(Miltenyi Biosciences) overnight at RT while rotating. For detection, samples were then incubated with fluorophore-conjugated beads coated in antigens against CD63, CD81, and CD9. Sample buffer was processed identically to CSF samples for use as a negative control. Flow cytometry was performed on a BD Biosciences LSR II with the following laser settings: forward scatter 350, side scatter 200, 488-1 360, 488-2 520, 633-1. Events were collected for 120 seconds with run speed at low.

Data analysis was performed using FlowJo version 10.10.0. The median APC value of each population was extracted. Values were buffer-subtracted and log10 transformed. Populations with APC values equal to buffer were considered not expressed; populations with APC values below buffer were considered negative and removed from the analysis. Populations that had APC values greater than buffer were considered expressed. Only markers present at detectable levels in at least eight of ten samples were analyzed.

2.5k: RNA Isolation

CSF EVs were enriched using SEC as described and 500µl of the EV fraction was used for miRNA analysis. RNA was extracted from EVs using the Urine miRNA Purification Kit (Norgen Biotek Corp), according to the manufacturer's instructions. Prior to final RNA elution samples were incubated with 30µL of elution buffer for 10 minutes at RT. To confirm successful isolations, 2µL of eluted RNA was analyzed using the Qubit miRNA assay kit and Qubit 4 fluorometer (TFS). Isolated RNA was stored overnight at -20°C prior to qPCR.

2.5l: MiRNA qPCR

CSF EV miRNA was analyzed by TaqMan qPCR arrays (TFS). MiRNA was converted to cDNA using the TaqMan Advanced miRNA cDNA Synthesis kit (A28007, TFS). Briefly, 3µL of total RNA was 3' poly-adenylated, followed by a 5' adaptor ligation step and reverse

transcription. The resulting cDNA (5µL) was added to a 14-cycle universal miR-amplification step. The miR-amplification reaction was diluted 1:10 with nuclease free water, 220µL of the diluted cDNA was mixed with 220µL of nuclease free water and 440µL of TaqMan Fast Advanced master mix (4444556, TFS). The qPCR mix (100µL) was loaded into each of the 8 ports of a TaqMan Advanced miRNA Human A Card (A34714, TFS), TaqMan Advanced miRNA Human B Card (A34714, TFS), or TaqMan Advanced Human miRNA Custom Card (TFS). All cards included a primary endogenous normalization control (miR-16-5p), an exogenous spike-in calibration control (cel-39-3p), and an exogenous negative control (plant ath-miR159a). Each card was assayed using a QuantStudio 7 Flex Real-Time PCR System (4485695, TFS) with the aid of an Orbitor RS2 Microplate Mover (ORB2001, TFS) to increase throughput and ensure each RNA isolation batch was processed on the same day. As a negative control, one card was run as described with water included in place of RNA.

2.5m: MiRNA Analysis

QuantStudio 12K Flex Software v1.3 and ExpressionSuite software v1.3 was used to process the qPCR data. MiRNA amplification values were calculated from the quantification cycle (Cq; number of PCR cycles before signal surpasses background) using automated baseline and threshold values determined by ExpressionSuite. MiRNAs with Cq ≤ 34.000 were considered expressed. MiRNAs that showed no amplification (“undetected”) or had Cq values over 34.000 were considered not expressed and censored at Cq=34. Amplification quality, calculated by Expression Suite, was further evaluated by Amplification Score (signal quality during the linear phase of amplification) and Cq Confidence (statistical confidence in the Cq value). MiRNAs with an Amplification Score < 0.950 and/or a Cq Confidence < 0.750 were

considered technical failures and removed from analysis. We also verified that there was little to no amplification in the exogenous negative control in each sample (plant ath-miR159a).

After filtering, miRNAs with good quality amplifications were calibrated and normalized. To control for technical variation in the quality of RNA isolation between samples, Cq values were calibrated with two normalization factors calculated for each sample: the Cq of the exogenous spike-in miRNA (cel-miR-39-3p); and the median Cq of all miRNAs that showed good quality amplification in all samples (n=24).

Sample normalization was performed by calculating the average expression of 4 endogenous controls for each sample. Endogenous controls were selected by identifying which miRNAs showed the most stable Cq values across all samples. The average endogenous Cq value was then subtracted from the Cq values of each miRNA to generate ΔCq. To compare expression between control and NPC samples, the ΔΔCq was calculated by subtracting the ΔCq of the control from the ΔCq of the NPC samples. The fold change (RQ) was calculated by using the $2^{\Delta\Delta Cq}$ method, with RQ > 1 indicating increased miRNA expression. Statistical significance was calculated by comparing the ΔCq of the control replicates with the ΔCq of the NPC replicates (Welch's t test). Data is shown as a Volcano plot (−Log10 (q-value) vs. the Log2(Fold change)) and the ΔCq mean ± standard error mean (SEM).

2.5n: MiRNA Target Prediction and Pathway Analysis

Identification of mRNA targets of the two differentially expressed miRNAs was performed using the online data base miRTarBase 2022[96] (experimentally validated mRNA) targets) and online prediction tools TargetScan Human version 8.0[97] and miRDB 2020[98] (predicted mRNA targets). To limit the number of predicted targets, we only included mRNAs that had a Cumulative Weighted Score above 0.3 in TargetScan or a target score above 80 in

miRDB. The combined list of validated or predicted mRNA targets of both miRNAs (n=1,390) was input into QIAGEN Ingenuity Pathway Analysis IPA). Significant canonical pathways were based on adjusted p-values using a BH false discovery rate (FDR) threshold of 0.1. In order to avoid the knowledge bias towards cancer in IPA, cancer related tissues, cell lines, and diseases were excluded from the analysis.

2.5o: Statistical Analysis

For VFC, MBFC, and miRNA experiments the samples were randomized, and the experimenter was blinded to group and sample identity. Data were analyzed with GraphPad Prism software v10.1.0 (GraphPad Software, Inc). The number of biological and technical replicates in each experiment are indicated in figure legends and results were averaged. Statistical tests were performed as indicated in legends. To compare between two groups Welch's t-test was used; for analyses involving more than four t-tests an FDR with a 20% BH correction was applied. Comparisons between more groups in VFC analysis was performed using two-way ANOVAs with Tukey's correction. Relationships between two variables were assessed using Pearson's correlation tests and simple linear regression.

2.6: Supplementary Figures

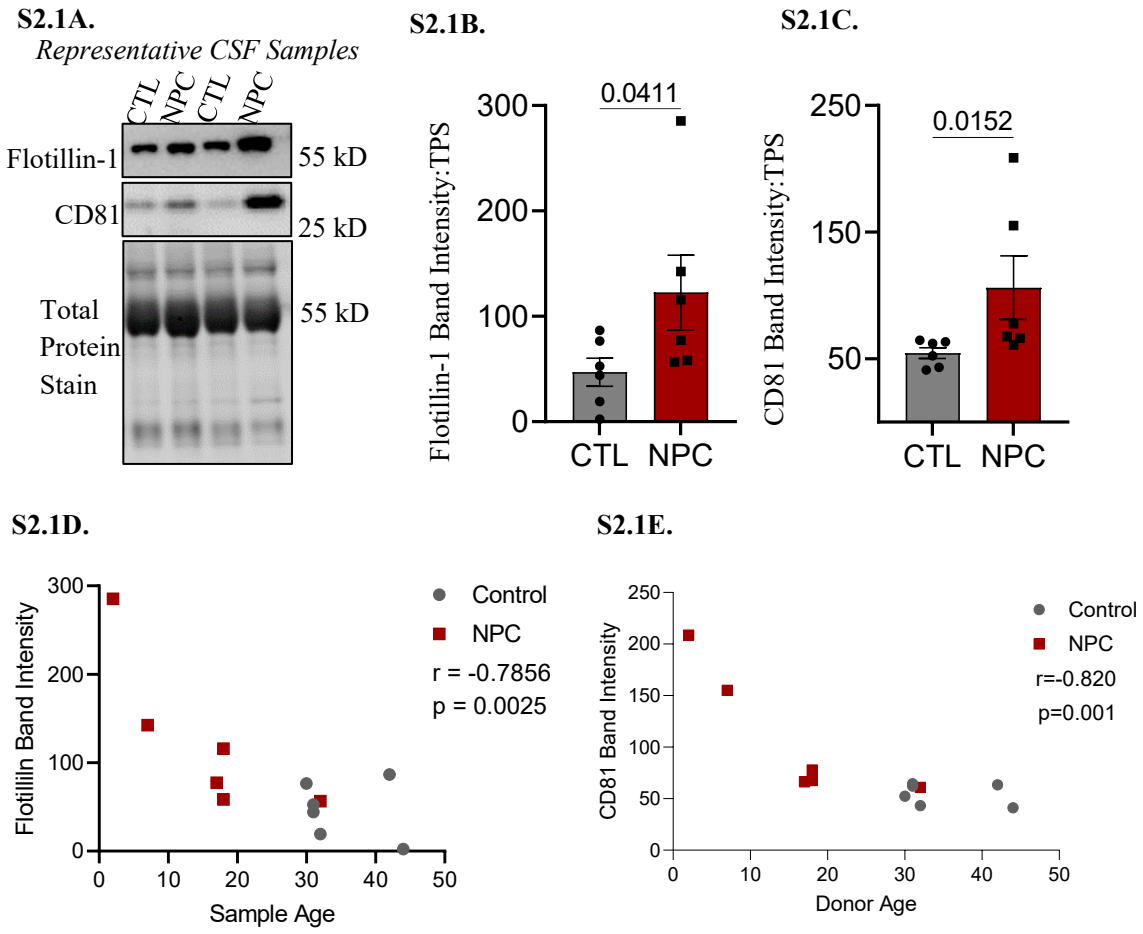

Supplementary Fig 2.1: Donor age correlates with CSF EV protein content. A) CSF from NPC patients and older controls was concentrated 10X and analyzed by immunoblot. EV proteins Flotillin-1 and CD81 were measured, as was total protein stain. **B, C)** Quantification of Flotillin-1 and CD81 band normalized to total protein stain (TPS) shows expression is elevated in NPC CSF samples as compared to controls. Bars represent the mean and standard error of each population; data analyzed by Welch's t test. **D, E)** Pearson's correlations show age of CSF donor significantly correlates with CSF Flotillin-1 (D) and CD81 (E) protein expression.

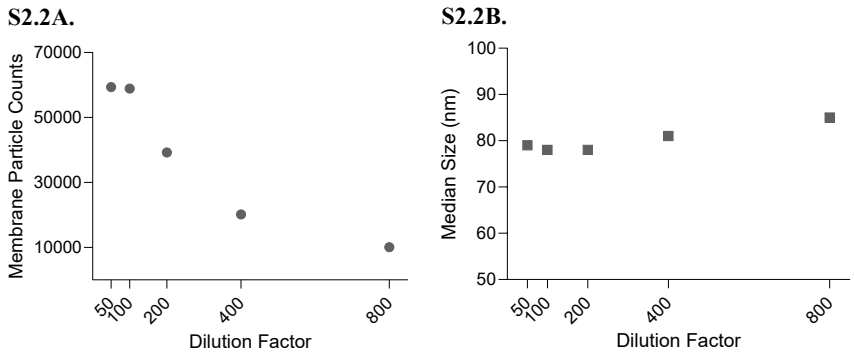

Figure S2.2: Identification of optimal CSF dilution tetraspanin staining via VFC. CSF samples were concentrated 10X and incubated with membrane dye and tetraspanin antibodies at a final dilution of 1:50, 1:100, 1:200, 1:400, or 1:800. **A)** In keeping with ISEV recommendations, dilution curves were used to identify the CSF pre-stain dilution that results in ~50,000 particle counts. **B)** CSF particle size does not change with dilution, confirming less dilute samples (1:50-1:200) do not result in particle swarm.

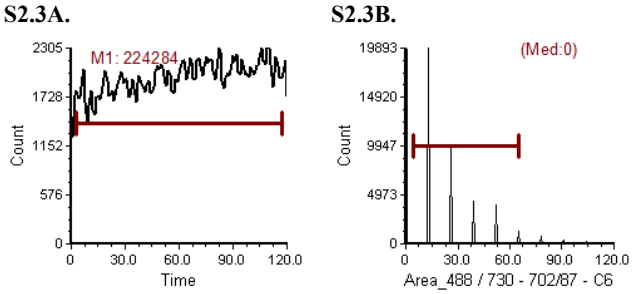

Figure S2.3: VFC time and area gates. A) Time gate of representative CSF sample. Plot shows number of events occurring over a 120 second run time. The time gate (red line) removes the first and last 3 seconds of the run to exclude fluidic anomalies. **B**) Area gate of representative CSF sample. Plot shows the area of particles occurring the in 488 FITC channel. Area gate (red line) is drawn to exclude background signal with no area, or signal with area greater than 4 pixels (coincident or out of focus events).

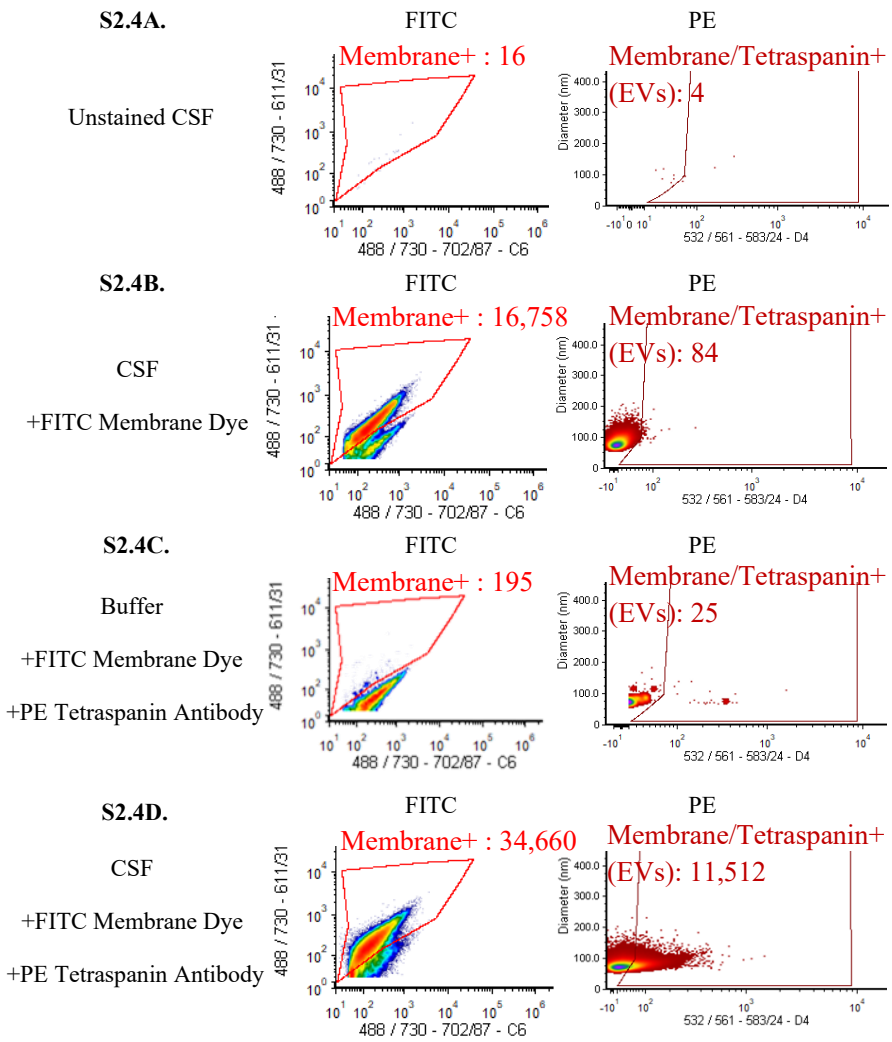

Figure S2.4: VFC background gating strategy to measure CSF tetraspanin positivity. Multiple negative controls are included in VFC studies to ensure background signal is removed. **A)** Unstained CSF shows near negative signal in both the FITC and PE channels. **B)** CSF sample stained only with membrane dye shows strong signal in the FITC channel, as expected. Signal appearing in the PE channel is considered background and gated out. **C)** Buffer stained with both membrane dye and tetraspanin antibody shows some signal in both the FITC and PE channels, which is considered background and gated out. **D)** Final gates applied to fully stained CSF sample allow for the inclusion of true signal and removal of background. Red lines on all plots represent final gates that have been adjusted to remove all background signals. Number of gated membranous particles (left) depicted in bright red on each plot; number of membranous and tetraspanin positive particles (right) written in dark red on each plot.

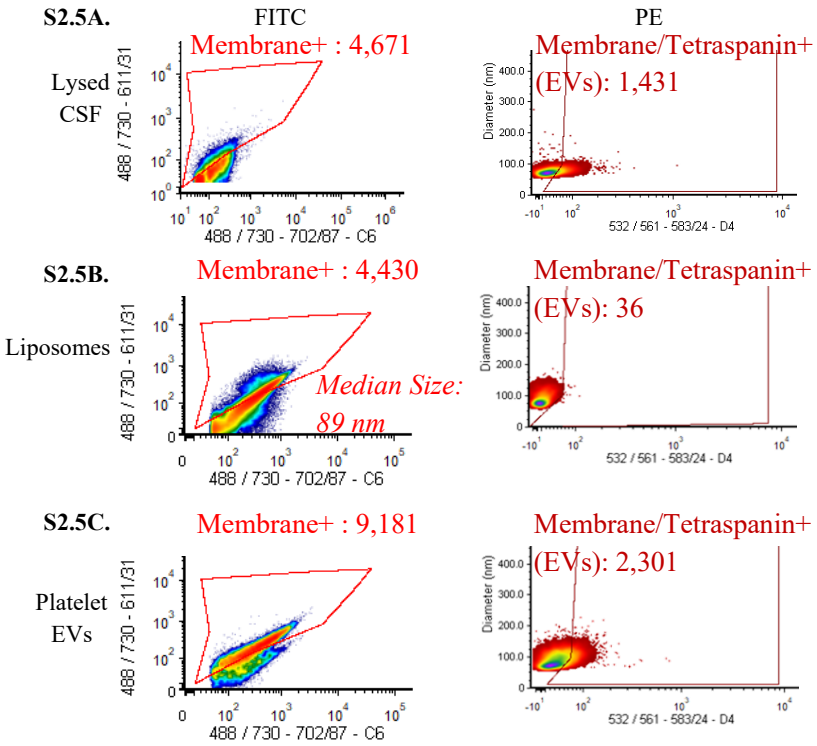

Figure S2.5: VFC negative and positive controls. To verify that gated events in CSF truly represent EV signal, multiple controls are included in each run. **A)** After completion of the standard staining protocol CSF samples are incubated in lysis buffer (0.1% Triton-X 100 PBS solution) for ten minutes to ensure signal is EV-derived. **B)** Liposomes of known size that are membrane-positive, tetraspanin-negative are used as a positive control to validate VFC size calculations gating strategies. **C)** Platelet EVs that are membrane- and tetraspanin-positive are included as a positive control for staining and gating procedures. All plots display signal occurring in FITC (488) or PE (561) channels; red lines represent applied membrane or tetraspanin gates.

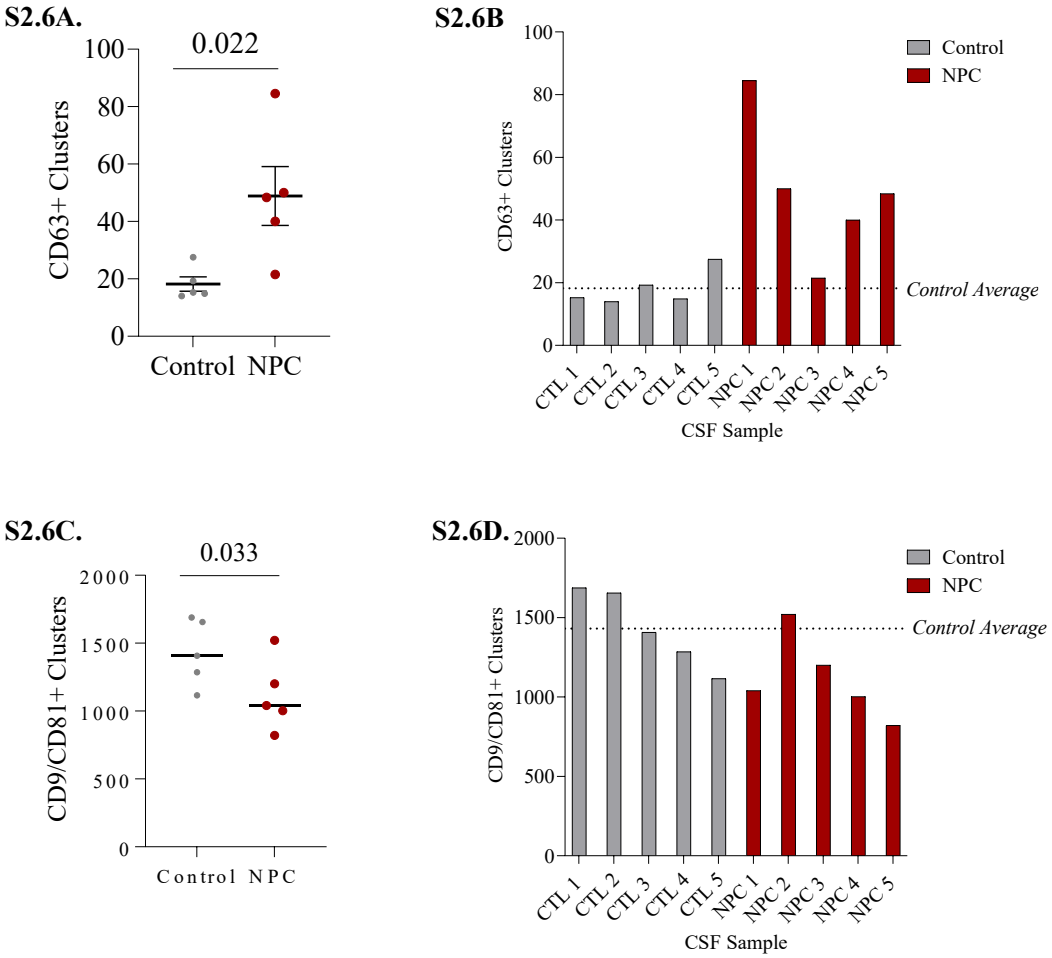

Figure S2.6: Increased CD63+ and decreased CD9/CD81+ EVS NPC CSF. A) There is a significant increase in CD63 single positive EVs in NPC CSF relative to controls (nested t-test). Graph displays the mean and SEM of control and NPC samples. Symbols represent individual samples averaged across all images. **B)** Count of CD63+ EVs in each CSF sample (average of all replicates). Dashed line corresponds to the average of all control samples. **C)** There is a significant decrease in CD9/CD81 double positive EVs in NPC CSF relative to controls (nested t-test). Graph displays the mean and SEM of control and NPC samples. Symbols represent individual samples (average of four to ten technical replicates). **D)** Count of CD9/CD81+ EVs in each CSF sample (average of all replicates). Dashed line corresponds to the average of all control samples.

Differential Expression			
	p-Value	Fold Change	q-Value
CD106	0.975	0.98	0.981
Lamp1	0.029	1.94	0.853
CD11b	0.943	0.98	0.981
CD13	0.758	1.35	0.971
CD133/1	0.161	2.18	0.853
CD140a	0.151	1.71	0.853
CD171	0.981	0.99	0.981
CD222	0.615	0.62	0.971
CD24	0.716	0.92	0.971
CD29	0.721	0.94	0.971
CD31	0.598	1.47	0.971
CD340	0.115	4.03	0.853
CD36	0.656	0.87	0.971
CD38	0.682	1.32	0.971
CD44	0.731	1.16	0.971
CD47	0.281	0.70	0.884
CD49a	0.813	1.10	0.981
CD49e	0.619	1.13	0.971
CD49f	0.894	1.01	0.981
CD54	0.965	1.01	0.981
CD56	0.262	0.35	0.884
CD63	0.847	1.04	0.981
Lamp4	0.092	5.03	0.853
CD81	0.304	0.85	0.884
CD9	0.213	0.75	0.853
CD90	0.599	1.53	0.971
CSPG4	0.589	0.83	0.971
CX3CR1	0.213	0.52	0.853
EGFR	0.213	0.79	0.853
GLAST	0.624	1.65	0.971
O4	0.643	0.87	0.971
PDPN	0.394	0.78	0.971

Supplementary Table 2.1: Evaluation of EV surface marker expression in NPC versus control CSF. p-values derived from of Welch's t tests. Fold changes represent the ratio of average NPC expression over average control expression. q-values derived from multiple comparisons testing (FDR with 20% BH correction). Green highlight designates values that met our cut-offs for significance in each category.

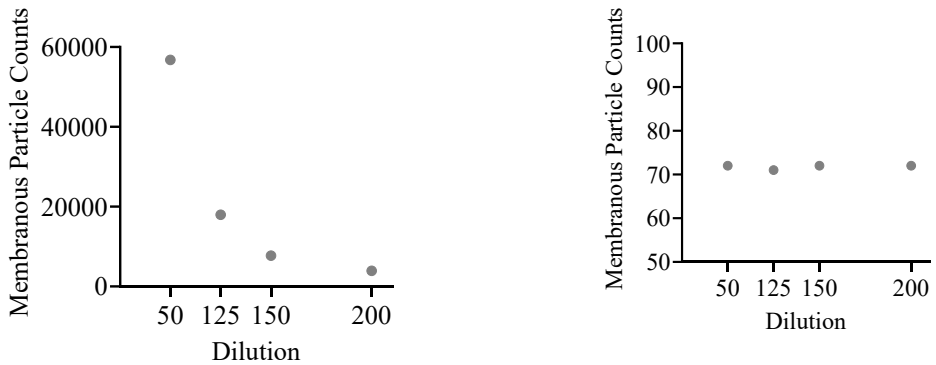

Figure S2.7: Identification of optimal CSF dilution for Lamp1 staining via VFC. CSF samples were concentrated 10X and incubated with membrane dye and tetraspanin antibodies at a final dilution of 1:50, 1:100, 1:200, 1:400, or 1:800. **A)** In keeping with ISEV recommendations, dilution curves were used to identify the CSF pre-stain dilution that results in ~50,000 particle counts. **B)** CSF particle size does not change with dilution, confirming less dilute samples (1:50-1:200) do not result in particle swarm.

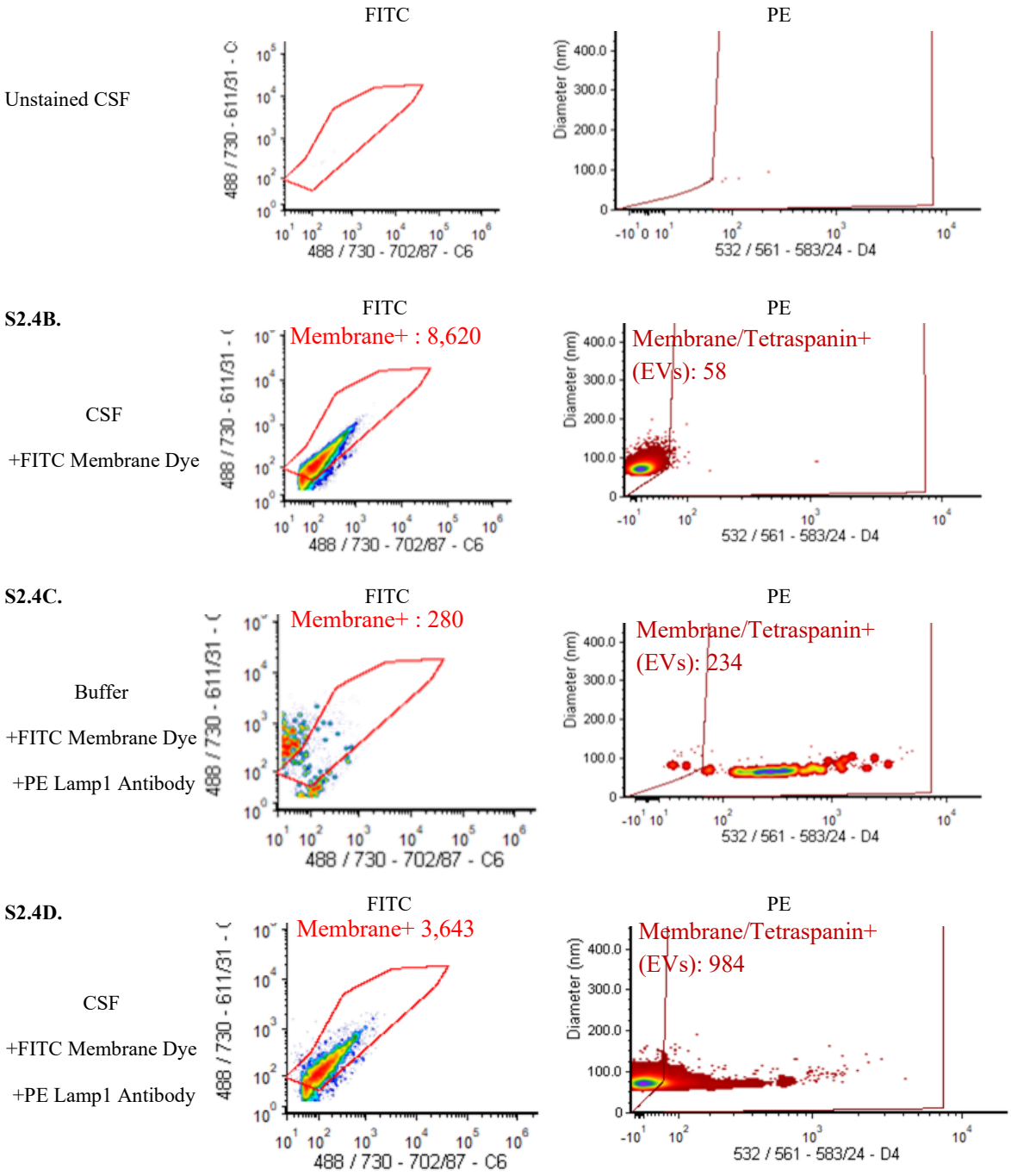

Figure S2.8: VFC background gating strategy to measure CSF Lamp1 positivity. Multiple negative controls are included in VFC studies to ensure background signal is removed. **A)** Unstained CSF shows near negative signal in both the FITC and PE channels. **B)** CSF sample stained only with membrane dye shows strong signal in the FITC channel, as expected. Signal appearing in the PE channel is considered background and gated out. **C)** Buffer stained with both membrane dye and Lamp1 antibody shows some signal in both the FITC and PE channels, which is considered background and gated out. **D)** Final gates applied to fully stained CSF sample allow for the inclusion of true signal and removal of background. Red lines on all plots represent final gates that have been adjusted to remove all background signals. Number of gated membranous particles (left) depicted in bright red on each plot; number of membranous and Lamp1 positive particles (right) written in dark red on each plot.

	Clinical Correlations											
	Age of Onset			Age of Collection			NPC-SS			Months on CD		
	p	q	r	p	q	r	p	q	r	p	q	r
CD106	0.082	0.516	-0.830	0.166	0.642	-0.725	0.435	0.882	0.461	0.829	0.985	0.134
Cd107a	0.152	0.642	-0.741	0.239	0.789	-0.646	0.672	0.975	0.261	0.362	0.882	0.526
CD11b	0.364	0.882	-0.525	0.497	0.949	-0.407	0.669	0.975	0.263	0.016	0.320	0.943
CD13	0.078	0.516	-0.836	0.019	0.320	-0.937	0.952	0.993	-0.038	0.541	0.949	0.369
CD133/1	0.621	0.975	-0.303	0.625	0.975	-0.299	0.970	0.993	0.024	0.045	0.444	0.887
CD140a	0.744	0.975	-0.203	0.514	0.949	-0.392	0.605	0.971	-0.316	0.475	0.935	-0.426
CD171	0.589	0.967	-0.329	0.647	0.975	-0.281	0.811	0.985	0.149	0.607	0.971	-0.314
CD222	0.420	0.882	-0.580	0.335	0.882	-0.665	0.985	0.993	-0.015	0.977	0.993	0.023
CD24	0.910	0.993	-0.071	0.746	0.975	-0.201	0.534	0.949	-0.375	0.133	0.610	0.763
CD29	0.082	0.516	-0.829	0.111	0.570	-0.791	0.713	0.975	0.227	0.016	0.320	0.944
CD31	0.993	0.993	-0.011	0.683	0.975	-0.478	0.580	0.965	-0.612	0.523	0.949	-0.682
CD340	0.125	0.592	-0.774	0.164	0.642	-0.728	0.653	0.975	0.276	0.902	0.993	0.077
CD36	0.428	0.882	0.467	0.425	0.882	0.470	0.804	0.985	-0.155	0.579	0.965	0.337
CD38	0.802	0.985	-0.198	0.920	0.993	0.080	0.535	0.949	0.465	0.231	0.789	-0.770
CD44	0.415	0.882	-0.478	0.426	0.882	-0.469	0.885	0.993	0.090	0.025	0.320	0.924
CD47	0.729	0.975	-0.214	0.978	0.993	0.017	0.258	0.827	0.626	0.352	0.882	-0.536
CD49a	0.044	0.444	-0.888	0.000	0.051	-0.995	0.963	0.993	-0.029	0.279	0.852	0.605
CD49e	0.099	0.527	-0.807	0.066	0.508	-0.854	0.912	0.993	0.069	0.702	0.975	0.236
CD49f	0.382	0.882	-0.509	0.274	0.852	-0.611	0.732	0.975	-0.212	0.025	0.320	0.924
CD54	0.287	0.853	-0.598	0.338	0.882	-0.549	0.787	0.985	0.168	0.001	0.090	0.989
CD56	0.065	0.508	-0.935	0.093	0.516	-0.907	0.570	0.965	0.430	0.402	0.882	0.599
CD63	0.380	0.882	-0.510	0.691	0.975	-0.246	0.325	0.882	0.561	0.171	0.643	0.719
CD68	0.055	0.504	-0.870	0.090	0.516	-0.819	0.732	0.975	0.212	0.067	0.508	0.851
CD81	0.933	0.993	-0.053	0.944	0.993	0.044	0.844	0.985	0.123	0.150	0.642	0.744
CD9	0.956	0.993	-0.035	0.922	0.993	0.061	0.846	0.985	0.121	0.159	0.642	0.733
CD90	0.393	0.882	-0.607	0.391	0.882	-0.609	0.797	0.985	0.203	0.813	0.985	-0.187
CSPG4	0.816	0.985	-0.145	0.929	0.993	-0.056	0.646	0.975	0.282	0.240	0.789	-0.645
CX3CR1	0.816	0.985	-0.145	0.923	0.993	0.061	0.508	0.949	0.397	0.184	0.674	0.704
EGFR	0.007	0.303	-0.967	0.090	0.516	-0.819	0.351	0.882	0.537	0.441	0.882	0.456
GLAST	0.033	0.389	-0.907	0.012	0.320	-0.952	0.842	0.985	0.125	0.490	0.949	0.412
O4	0.385	0.882	0.506	0.730	0.975	0.214	0.116	0.573	-0.784	0.727	0.975	0.216
PDPN	0.192	0.682	-0.696	0.301	0.876	-0.584	0.550	0.952	0.361	0.025	0.320	0.924

Supplementary Table 2.2: Evaluation of CSF EV surface protein correlations with NPC clinical data. p-values and r-values derived from of Pearson's test. q-values derived from multiple comparisons testing (FDR with 20% BH correction). Green highlight designates values that met our cut-offs for significance in each category.

miRNA	Age at Sampling		Age of Onset		NPC-SS		Months on CD	
	p	r	p	r	p	r	p	r
hsa-let-7a-5p	0.66	-0.19	0.96	-0.04	0.14	-0.86	0.30	0.85
hsa-let-7d-5p	0.29	-0.40	0.85	-0.12	0.29	-0.59	0.18	0.73
hsa-let-7g-5p	**0.71**	**-0.14**	**0.82**	**0.14**	**0.10**	**-0.80**	**0.96**	**0.15**
hsa-miR-100-5p	0.05	-0.68	0.06	-0.86	0.76	-0.19	0.19	0.68
hsa-miR-125a-5p	0.01	-0.82	0.08	-0.84	0.74	-0.21	0.42	0.43
hsa-miR-1260a	0.72	-0.14	0.40	-0.49	0.02	0.94	0.87	0.06
hsa-miR-144-3p	0.30	0.39	0.16	0.73	0.49	-0.41	0.75	-0.09
hsa-miR-153-3p	0.74	-0.13	0.71	0.23	0.09	-0.82	0.61	0.37
hsa-miR-17-5p	0.36	0.35	0.52	0.39	0.17	0.72	0.96	-0.02
hsa-miR-181c-5p	0.89	0.06	0.62	0.30	0.84	-0.12	0.26	0.57
hsa-miR-199a/b-3p	**0.86**	**-0.07**	**0.63**	**0.30**	**0.39**	**-0.50**	**0.08**	**-0.75**
hsa-miR-200a-3p	0.64	-0.20	0.89	-0.08	0.62	-0.30	0.42	0.62
hsa-miR-204-5p	0.37	0.34	0.18	0.71	0.85	-0.12	0.02	-0.97
hsa-miR-21-5p	0.62	-0.19	0.03	-0.92	1.00	0.00	0.16	0.71
hsa-miR-223-3p	0.25	0.43	0.06	0.87	0.32	-0.57	0.78	-0.17
hsa-miR-29a-3p	0.11	0.61	0.35	0.65	0.82	-0.18	0.51	-0.32
hsa-miR-320a	**0.73**	**0.15**	**0.24**	**0.65**	**0.93**	**0.06**	**0.70**	**0.19**
hsa-miR-342-3p	0.60	0.20	0.75	0.20	0.78	0.17	0.05	-0.91
hsa-miR-34c-5p	0.64	-0.18	0.56	-0.36	0.42	0.48	0.53	0.53
hsa-miR-374a-5p	0.16	0.51	0.60	0.32	0.21	0.68	0.24	-0.65
hsa-miR-374b-5p	0.98	-0.01	0.72	0.22	0.26	-0.63	0.40	0.54
hsa-miR-376a-3p	0.59	-0.21	0.58	-0.34	0.49	-0.41	0.14	0.83
hsa-miR-380-3p	0.76	0.12	0.32	0.56	0.32	-0.57	0.92	0.16
hsa-miR-423-5p	0.86	-0.07	0.74	-0.21	0.03	0.91	0.56	0.27
hsa-miR-448	0.94	0.03	0.57	0.35	0.24	-0.64	0.49	0.45
hsa-miR-502-3p	0.87	-0.06	0.73	0.21	0.39	-0.50	0.37	0.59
hsa-miR-524-3p	0.46	-0.31	0.52	-0.48	0.14	0.86	0.27	0.87
hsa-miR-628-3p	0.95	-0.03	0.80	-0.16	0.57	0.35	0.28	0.45
hsa-miR-653-5p	0.66	0.17	0.51	0.40	0.97	-0.03	0.40	0.52
hsa-miR-885-5p	**0.94**	**0.03**	**0.25**	**0.64**	**0.10**	**-0.81**	**0.99**	**0.02**

Supplementary Table 2.3: Evaluation of CSF EV miRNA correlations with NPC clinical data. p-values and r-values derived from of Pearson's test. Green highlight designates p-values<0.05; no values survived 20% BH FDR. miRNAs in bold were upregulated in comparison to control CSF EVs.

CHAPTER 3: ALTERED CONCENTRATION AND PROTEIN CARGO IN NPC DERMAL FIBROBLAST EVS

3.1: Abstract

Niemann Pick Disease Type C (NPC) is a rare autosomal recessive disorder caused by primarily mutations in the *NPC1* protein, which is responsible for transporting cholesterol out of endolysosomes. We previously demonstrated that cerebrospinal fluid (CSF) from NPC patients contains increased concentration of extracellular vesicles (EVs) as compared to healthy controls, and that NPC EVs carry different proteins and miRNA cargo. Here, we investigated whether NPC EV alterations also extend to patient fibroblasts. We isolated EVs from dermal fibroblasts from healthy control donors (n=3) and NPC patients (n=5) with different *NPC1* gene mutations. We found that EV concentration was inversely correlated with NPC1 protein expression in fibroblast cells. Treatment with hydroxypropyl-β-cyclodextrin (CD), an experimental treatment for NPC patients that is currently in Phase III clinical trials, was able to partially attenuate the increase in EV concentration between NPC and control cells. We also found that fibroblast EVs are significantly enriched in lysosomal-associated membrane protein 1 (Lamp1), a protein previously implicated in NPC. These data demonstrate that NPC EV alterations are not unique to CSF, but may be part of NPC pathology more broadly.

3.2: Introduction

In Chapter 2, we discovered a number of alterations to EVs CSF of NPC patients as compared to healthy controls. These include an increase in the overall concentration of CSF EVs; an expansion of EVs originating from the endosome; and an enrichment for disease-relevant cargo, including Lamp1 and miRNA-320a, which regulates cholesterol. However, the NPC patients in this study were undergoing treatment with the experimental drug CD, while the

healthy control cohort was untreated. It is thus unknown if the alterations we observed are due to NPC pathology or to the CD treatment.

Until very recently, there were no FDA approved drugs for NPC. However, CD became available to NPC patients under expanded access (also termed "compassionate care") guidelines in 2009, and since then it has been used to treat many patients[99, 104]. CD is a large polysaccharide commonly used as a drug vehicle due to its ability to bind and solubilize hydrophobic, lipid-dense molecules; in fact, the positive impact of CD on NPC was discovered by accident when it was used as a vehicle-only control. CD enters the cell through endocytosis and is delivered directly to endolysosomes, where it is thought to improve NPC pathology by redistributing cholesterol and other lipids from endolysosomes to other sites in the cell[80].

Despite success in animal models, CD clinical trials in NPC patients have generated conflicting results. In an 18-month phase 1-2a trial, CD successfully slowed disease progression in NPC patients (n=14)[110]. This was followed by a one-year phase 2-3 trial in 56 patients which failed to show significant differences between treatment and placebo cohorts (NCT02534844). However, the design of the phase 2-3 trial (randomized control trial with a placebo occurring over one year) has been criticized, as there was unequal randomization, higher variability than expected, and likely not enough time to observe treatment effects[5]. Thus, further research into the efficacy of CD as an NPC therapeutic is needed.

Interestingly, the *NPC1* gene is ubiquitously expressed in every cell type at relatively consistent levels[7]. Why *NPC1* mutations cause a primarily neurodegenerative phenotype, particularly in the cerebellum, is largely unknown[21]. There is thus great interest in identifying alterations in NPC that are unique to the central nervous system (CNS).

To address the CD treatment effect and explore CNS versus peripheral changes to EVs in NPC, we turned to *in vitro* experiments. We obtained dermal fibroblasts from healthy control donors (n=3) and NPC patients (n=5). As in Chapter 2, the NPC patient donors carried different *NPC1* mutations, which allows for a better representation of NPC heterogeneity. Using these cells, we sought to determine how EV concentration and molecular cargo was altered in NPC fibroblasts, again focusing on EV surface markers and miRNA content to align with our CSF data, and to then examine the effect of CD on these cells. Our results included areas of overlap between CSF and fibroblast EVs, including Lamp1 alterations, as well as unique findings in regard to EV concentration and miRNA expression. Together, these studies add to a growing body of evidence that EVs are fundamentally altered by NPC pathology.

3.3: Results

3.3a: Fibroblast Cell Line Characteristics and Heterogeneity

The demographic and clinical characteristics of dermal fibroblast cell lines from healthy control donors (n=3) and NPC patients (n=5) are detailed in **Table 3.1.** Although all information was not available for NPC 4, effort was made to match the age at collection between control and NPC lines (control average age = 23.7, standard deviation = 2.5; NPC average age = 23.3, standard deviation = 6.8, excluding NPC 4 of unknown age). One donor was female (NPC 3) while all others were male; we expect this had minimal impact as sex differences have not been observed in NPC patients[2].

Table 3.1: Human dermal fibroblast samples

Status	Sample	Source	Sex	Age at Collection	Age of Onset	Disease Severity
NPC *n=5*	NPC 1	Rush	M	23	13	Mild
	NPC 2	Rush	M	31	31	Moderate
	NPC 3	Rush	F	18	16	Mild-Moderate
	NPC 4	Coriell GM18453	M	Unknown	Unknown	Unknown
	NPC 5	Rush	M	21	22mos	Mild
Controls *n=3*	CTL 1	Coriell GM23972	M	26	-	-
	CTL 2	Coriell GM03652	M	24	-	-
	CTL 3	Coriell GM03377	M	19	-	-

The NPC donors displayed heterogeneity in

age of disease onset, which refers to the age at which neurological symptoms first appeared and can be broadly used to predict patient symptoms and disease progression[5]. In our cohort, one patient presented in the early infantile group (NPC-5, age of onset 22 months), which is associated with epileptic symptoms and enlarged spleen; one presented in the juvenile group (NPC-2, age of onset 13 years), which typically includes both muscle control issues and cognitive decline; two presented in the adult group (NPC-1, age of onset 23; NPC-3, age of onset 18), which is less likely to include seizures and more likely to include neurodegeneration and cognitive impairment; and age on onset for NPC-4 is unknown[4]. Disease severity, as indicated by the treating physician, ranged from mild to moderate for the four donors with clinical information.

The genetic mutations of each patient donor and resulting protein alterations are described in **Table 3.2** and **Fig 3.1**. Prior to experimentation, we confirmed the *NPC1* mutations in each cell line using Sanger sequencing (**Supplementary Fig 3.1**). The NPC1 protein contains 13 transmembrane domains (TMDs), which include a sterol-sensing domain (SSD), as well as three luminal-facing domains that include binding sites for the NPC2 protein and for cholesterol[89]. While the exact impact of each mutation on NPC1 protein function is unknown, inferences can be made from the protein domains each mutation occurred in[17]. We also measured NPC1 protein expression in each cell line by immunoblot, allowing for some genotype-phenotype comparisons of protein expression (**Fig 3.2A, B**). The mutations of three fibroblast cell lines (NPC-1, NPC-2, and NPC-3) matched mutations carried by CSF donors described in Chapter 2. NPC-1 carried the S667L mutation in the SSD and T137M at the luminal site of cholesterol binding. SSD mutations typically lead to severe protein misfolding, causing most of

Table 3.2: NPC fibroblast mutations.

	Allele 1		Allele 2	
Sample	**Gene**	**Protein**	**Gene**	**Protein**
NPC 1	2000 C>T	S667L	410 C>T	T137M
NPC 2	2196dupT	S733fsX10	1301 C>T	P434L
NPC 3	3425 T>C	M1142T	2366 G>A	R789H
NPC 4	3182 T>C	I1061T	3182 T>C	I1061T
NPC 5	3182 T>C	I1061T	3182 T>C	I1061T

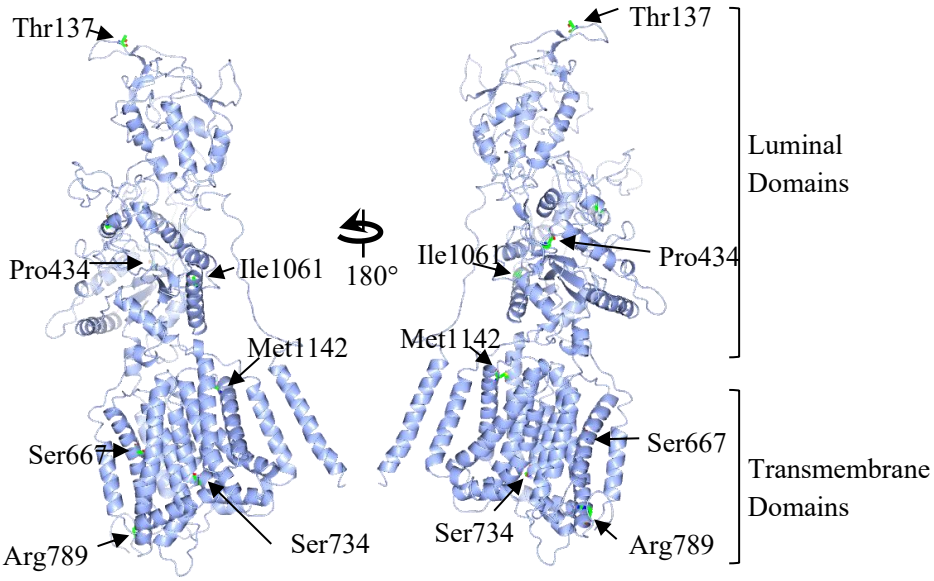

Figure 3.1: NPC1 mutations in fibroblast donors. Structure of full-length NPC1 protein in nanodisc as determined by electron microscopy (Qian *et. al.* 2020) was accessed from the Protein Data Bank (PDB:6W5R). Mutated residues mutated in NPC patient fibroblasts are labelled and colored by atom type. Identification of protein domains was based on descriptions given by Trinh *et. al.* 2018. Image generated in CCP4MG version 2.10.11.

the NPC1 protein to be degraded; indeed, by immunoblot, very little NPC1 protein was expressed in this cell line[91]. Although SSD mutations are also correlated with infantile disease onset[5], this patient had a disease onset of 13, suggesting the T137M mutated NPC1 was able to partially compensate for the other allele. The NPC-2 cell line carried a frameshift mutation in the SSD as well as loss of a proline at the NPC2 binding site; this cell line showed almost no NPC1 expression by immunoblot. Both NPC-3 mutations were in the TMD but only one (R789H) was

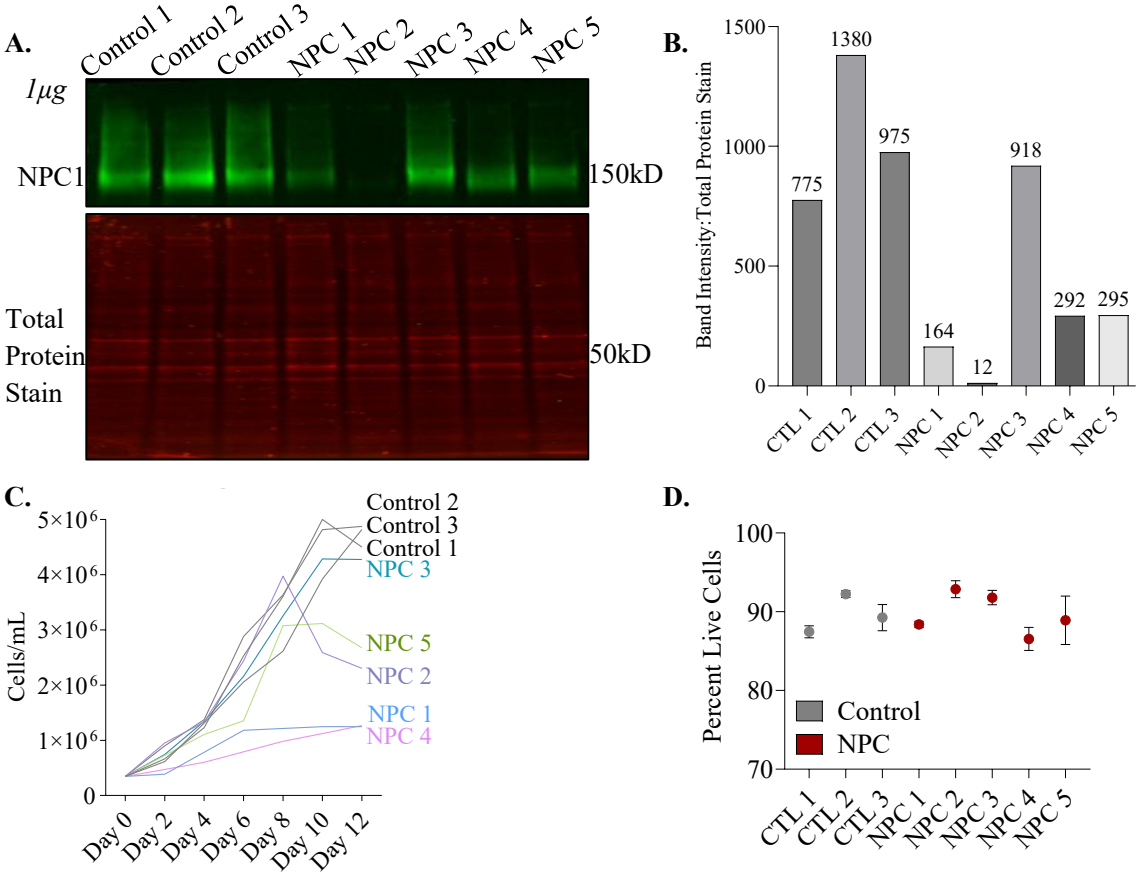

Figure 3.2: NPC1 expression and growth patterns of human dermal fibroblasts. A) Control and NPC fibroblasts show differential expression of NPC1 by immunoblot. **B)** Quantification of NPC1 band expression normalized to total protein stain. Values for each cell line are shown above the bars. **C)** Fibroblast growth rates by cell line. Plot represents average of two independent culture flasks per time point. Control cell lines shown in gray; NPC mutant cell lines are colored. **D)** Viability of fibroblast cell lines on days 4-6, depicted as the percentage of total cells that were live. Symbols represent the mean ± SEM of three independent culture flasks per cell line.

in the SSD; NPC1 protein expression was at the level of controls. Finally, both NPC-4 and NPC-5 were homozygous for I1061T, which is the most common pathogenic NPC mutation and is responsible for approximately 20% of cases[111]. This mutation occurs in the luminal C-terminal domain and is associated with late infantile or juvenile disease onset, as it encodes a protein that is functional but excessively degraded at the endoplasmic reticulum[111]. Both NPC-4 and NPC-5 showed nearly identical decreases in NPC1 protein expression, and though the age of onset for NPC-4 is unknown, NPC-5 did show late infantile age of onset.

Interestingly, NPC1 protein expression only partially predicted fibroblast growth rates (**Fig 3.2C**). NPC-3 showed NPC1 expression near controls and, as expected, grew at a similar rate to control cells. Yet NPC-2, which had the lowest NPC1 expression, also grew at a similar rate to controls (though it did not survive as long and showed decline after one week in culture). Despite having the same genetic mutation, NPC-4 and NPC-5 showed very different growth patterns. To control for this variability, all experiments were performed on cells harvested at Day 4 (Controls 1-3, NPC-3, NPC-5, and NPC-2) or Day 6 (NPC-1, NPC-4). All cell lines maintained 85-95% viability at this time point (**Fig 3.2D**).

3.3b: Size Exclusion Chromatography Enriches for EV From Conditioned Cell Culture Media

To investigate the impact of NPC on fibroblast EVs, we first validated methods to enrich for EVs from fibroblast media. Conditioned media was collected from each flask, centrifuged and filtered to remove cell debris, and concentrated to a final volume of 500µl (**Fig 3.3A**). Size exclusion chromatography (SEC) was then used to separate EV-rich fractions from other proteins in conditioned media. Immunoblot confirmed that SEC fractions 1-4 contained the highest amounts of EV proteins (Flotillin-1, CD63, and CD81) with minimal contamination from other proteins (total protein stain) (**Fig 3.3B**). When pooled, fractions 1-4 showed enrichment for these EV proteins without contamination from the cell protein GM130 (**Fig 3.3C**). Microchip resistive-pulse sensing (MRPS) showed that our cell EV preparations contain approximately $1.3x10^9$ particles/mL with a mean size of 78.9nm (**Fig 3.3D**). These results confirm SEC as an effective method for isolating EVs from fibroblast media.

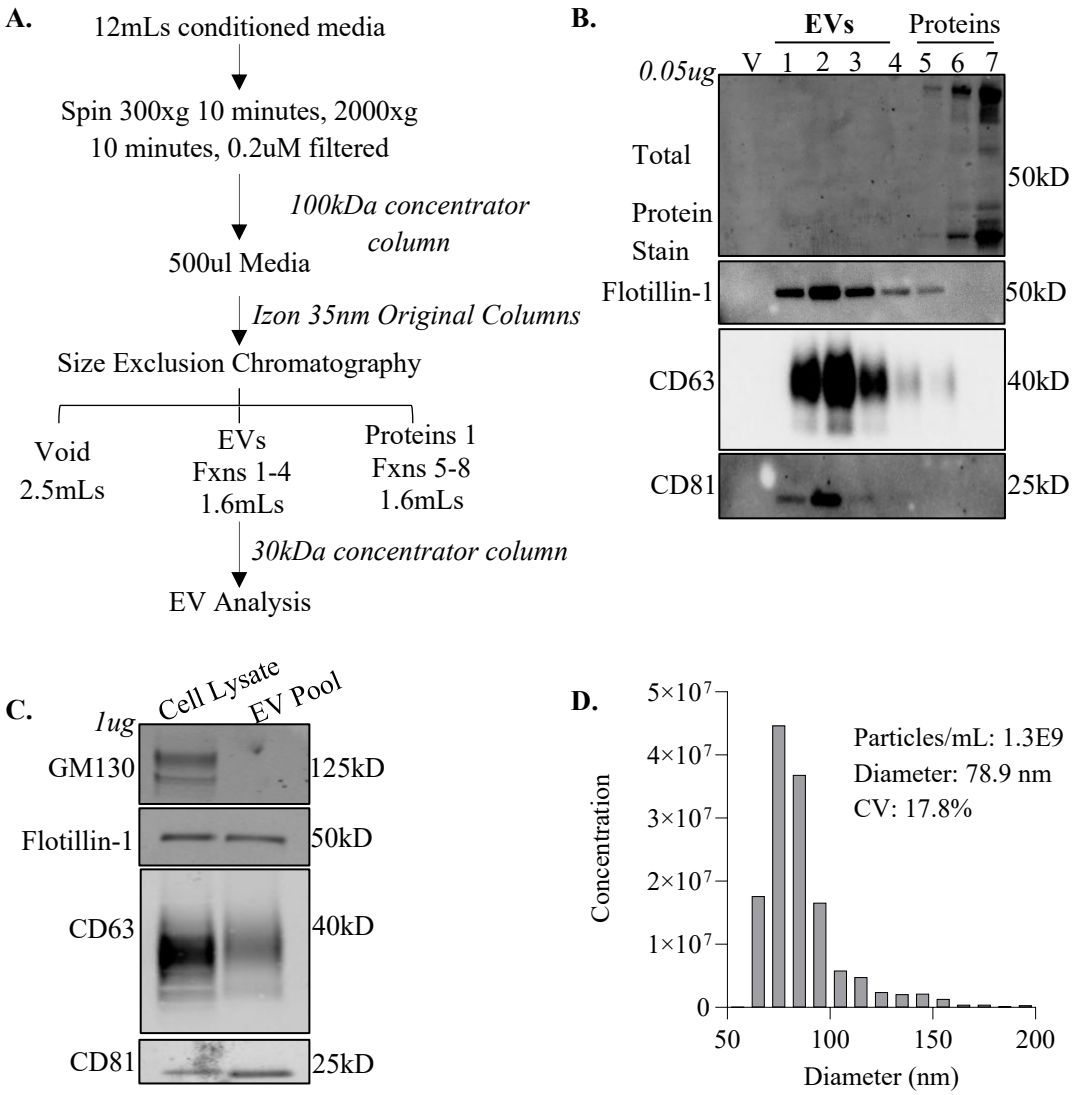

Figure 3.3: SEC isolates EVs from fibroblast conditioned media. A) EV enrichment method for fibroblast conditioned media. **B, C)** Immunoblots of individual (B) or pooled (C) SEC fractions from control fibroblast media show enrichment for EV proteins Flotillin-1, CD63, and CD81, without including other proteins (total protein stain) or cell lysate protein GM130. **D)** MRPS histogram shows the distribution of particles in pooled EV fractions isolated from control fibroblast media. Mean particle count, size, and coefficient of variation are listed.

3.3c: NPC1 Expression Inversely Correlates with EV Concentration

Previous work has shown that fibroblast cells from one NPC patient release an increased amount of EVs compared to healthy control cells[72]. To determine whether this is true in our larger cohort of fibroblast lines, we used vesicle flow cytometry (VFC) to measure the size and concentration of fibroblast EVs. In keeping with recommendations from the International Society of Extracellular Vesicles (ISEV), we first validated the ideal dilution, staining, and gating protocols for fibroblast EVs (**Supplementary Fig S3.2-5**)[66]. We then stained EVs from each cell line with *i)* a lipophilic membrane dye to label all membranous particles (conjugated to a FITC fluorophore in the 488 channel) (**Fig 3.4A, B**) and *ii)* a pool of antibodies against the canonical

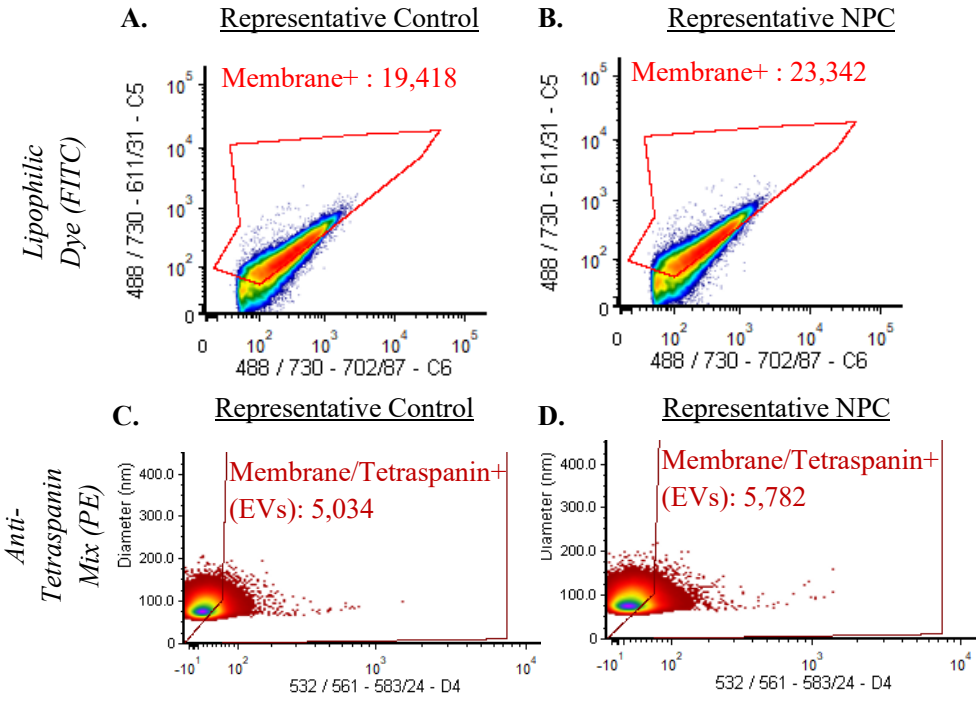

Fig 3.4: VFC gates of representative control and NPC fibroblast EV samples. A, B) Control (A) and NPC fibroblast EV (B) samples are stained with a lipophilic dye conjugated to FITC. Plots show dye signal in the 488 channel. Gates depicted in bright red include all membranous particles and exclude background signal present in negative controls. Number of gated membrane positive events is in bright red above each gate. **C, D)** Membranous particles gated in A/B are further gated by tetraspanin positivity. Plots show antibody signal in the 561 channel. Gates depicted in dark red include membranous and tetraspanin positive particles (true EVs) and exclude background signal present in negative controls. Number of gated EVs is written in dark red within each gate.

tetraspanins CD63/CD81/CD9 to label tetraspanin-positive particles (conjugated to a PE fluorophore in the 561 channel) (**Fig 3.4C, D**). Particles that are both membranous and tetraspanin positive are considered true EVs. Particle concentrations were normalized to cell count at the time of EV collection.

In contrast to CSF, our results show no change in the concentration of total membranous particles (**Fig 3.5A**) or EVs between control and NPC cells (**Fig 3.4B**). However, the NPC samples showed much greater heterogeneity in concentration than the controls, which was demonstrated by a statistically significant increase in variance by F test ($p=0.045$ for membranous particles, $p=0.038$ for EVs). EVs were slightly smaller than all membranous particles, but there were no significant differences in median size or size variability between control and NPC (**Fig 3.4C**). Given the variability NPC samples, we examined EV concentration by individual mutation and found that the cell line with the lowest NPC1 expression (NPC-2) had the highest EV concentration (**Fig 3.5D**). Indeed, the concentration of both total membranous particles and EVs were inversely correlated with NPC1 expression (**Fig 3.5E, F**). These results indicate that loss of NPC1 protein is associated with increased concentration of EVs.

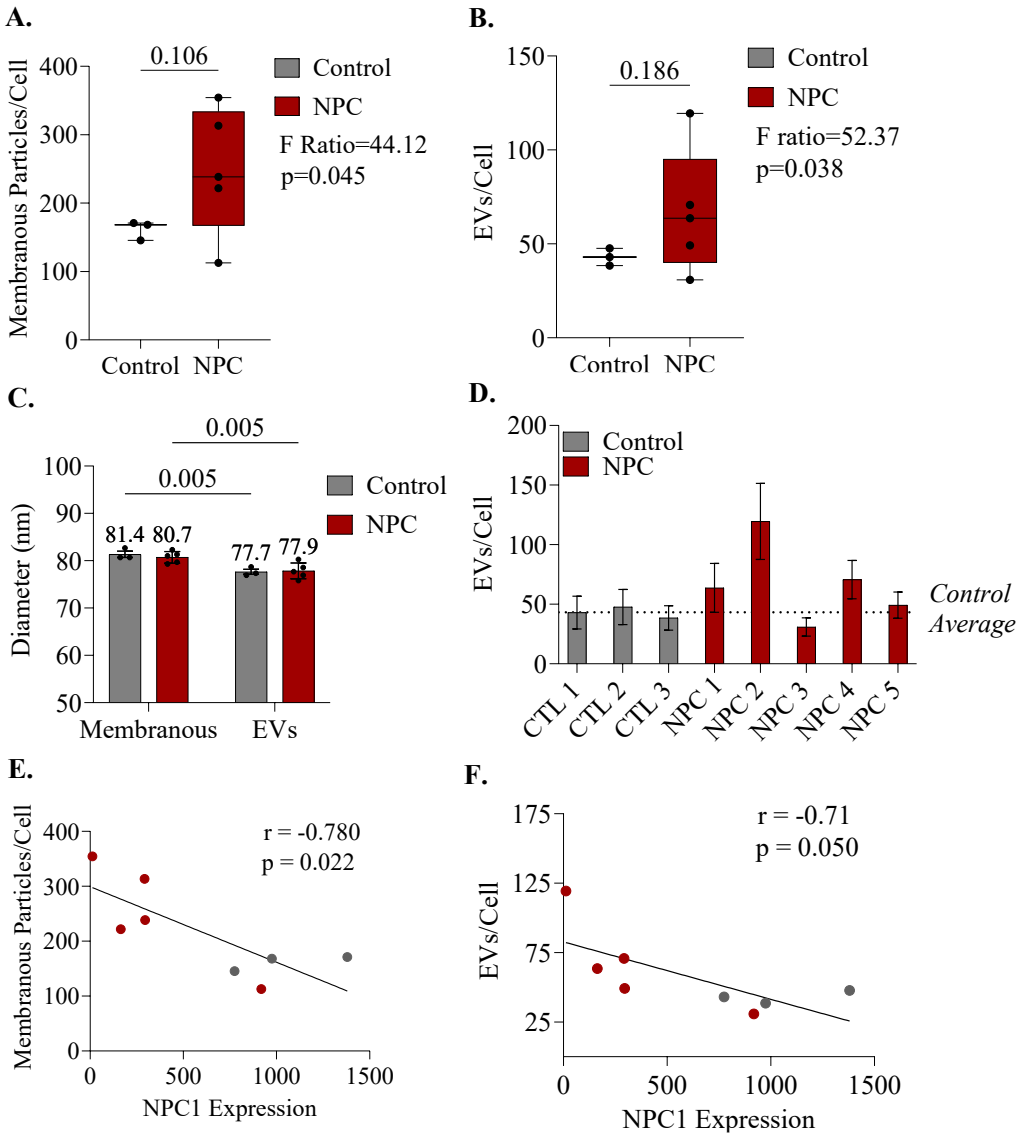

Figure 3.5: EV concentration from NPC fibroblasts is variable and correlates with NPC1 expression. EVs from control and NPC fibroblasts were incubated with lipid membrane dye (FITC) and a combined antibody against CD9/CD81/CD63 (PE). **A, B)** There is no change in concentration of total membranous particles (A) or EVs (B) between control and NPC fibroblasts (Welch's t-test), but NPC cells show significantly higher variation than controls (F test). Boxes display the median value (middle line) ± the upper and lower quartiles; symbols represent individual cell lines (average of three replicates). Welch's t-test p-values are listed above the plot; F test F ratios and p-values are listed to the right. **C)** Median size of EVs is significantly smaller than that of membranous particles (two-way ANOVA). There is no change in size between control and NPC membranous particles or EVs. Symbols represent an n=3 technical replicates per sample; mean ± SEM of control and NPC are graphed. Median size of each population is shown above the bars. **D)** Concentration of EVs from each fibroblast line. Bars show the mean concentration of three technical replicates per sample; error bars correspond to SEM. Dashed line represents average of all control samples. **E, F)** Concentration of membranous particles (E) and EVs (F) inversely correlate with NPC1 protein expression (Pearson's test). Control values are in gray; NPC values in red. Black line represents linear regression.

3.3d: CD Treatment Partially Attenuates Elevated EV Concentrations in NPC Cell Line

CD is an experimental treatment for NPC that is currently in Phase III clinical trials (NCT04860960). Some studies have shown that CD treatment can alter EV release, but the relationship between CD and EVs in the context of NPC is not well understood[112]. To investigate, we focused on the NPC-2 cell line as it showed the lowest NPC1 protein expression and highest EV release (**Fig 3.2B, Fig 3.5D**). NPC-2 and Control-2 cells were treated with CD or vehicle (water) for 48 hours, EVs were collected from cell conditioned media using SEC, and VFC was used to compare membranous particles and tetraspanin-positive EVs. The results show that CD treatment did not affect viability in either cell line (**Fig 3.6**).

The concentration of membranous particles was not affected by disease status or CD treatment, although there was a trending increase in the NPC samples over vehicle-treated control (**Fig 3.7A**). As predicted by **Fig 3.5D**, EV concentration was significantly increased in NPC-2 over CTL-2 (p=0.039); yet interestingly, this effect was lost in NPC cells treated with CD (p=0.419) (**Fig 3.7B**). This indicates that CD treatment is able to partially attenuate the increase in EVs seen in NPC samples. In NPC cells, we also observed a small but significant increase in the diameter of total membranous particles (**Fig 3.7C**) but not in EVs (**Fig 3.7D**). No statistically relevant size differences were observed between control and NPC cells. These results show that in NPC but not control cells, CD results in the release of slightly larger,

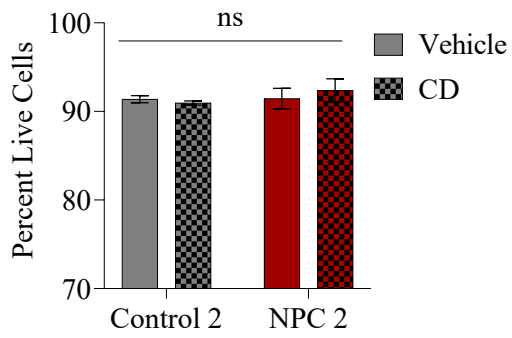

Figure 3.6: CD treatment does not affect fibroblast viability. Fibroblasts treated with vehicle (water) or CD for 48 hours showed no change in viability (two-way ANOVA with Tukey's correction). Bars represent the mean ± SEM of three replicate cultures per condition. Gray bars correspond to Control 2 cells; red bars correspond to NPC2 cells. CD treatment is depicted by checkered pattern.

membrane-positive but tetraspanin-negative particles, which could be larger EV populations (e.g. microvesicles) or non-EV material.

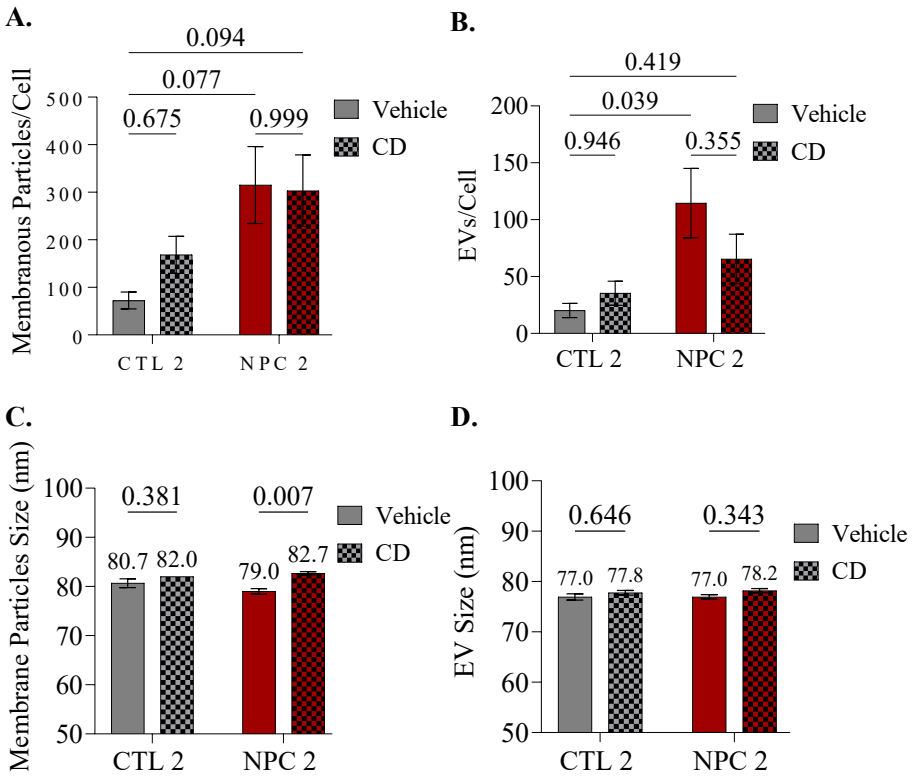

Figure 3.7: CD partially attenuates increased EVs in NPC fibroblasts. A) CD treatment has no impact on the concentration of total membranous particles released from control or NPC cells. **B)** CD treatment partially attenuates increased EV concentrations between NPC and control cell lines. **C, D)** CD treatment slightly but significantly increases the size of membranous particles from NPC fibroblasts (C) but does not affect EV size (E). Median size of each population is depicted above each graph. All graphs depict the mean ± SEM of three technical replicates per condition. Gray bars correspond to Control 2 cells; red bars correspond to NPC2 cells. CD treatment is depicted by checkered pattern. All p-values represent two-way ANOVAs with Tukey's correction.

3.3e: Increased Lamp1 and ICAM-1 Expression in NPC Fibroblast EVs

Previous work in rodent models has demonstrated that NPC1 inhibition alters the protein and lipid content of EVs[51, 75]. We thus sought to investigate whether EV surface markers are altered in our NPC fibroblast cells. Using multiplexed bead-based flow cytometry (MBFC) we measured the expression of 37 common EV markers in our three control and five NPC cell lines. Thirty-three proteins were expressed in all cells (**Fig 3.8A**). Interestingly, we observed a significant increase in Lamp1 expression in NPC fibroblast EVs relative to controls (**Fig 3.8B**, C), which aligns with our previous observations in NPC CSF EVs (**Fig 2.10**). There was also a significant increase in expression of intercellular adhesion molecule-1 (ICAM-1) (**Fig 3.8D, E**). Lamp1 and ICAM-1 expression were positively correlated (**Fig 3.8F**), and both correlated negatively with NPC1 expression (**Fig 3.8G,H**). These results suggest that loss of NPC1 is associated with an increase in Lamp1- and ICAM-1- positive EVs.

We further probed the cause of elevated Lamp1-positive EVs, given that we and others have observed its increase in various NPC tissues[75, 76, 95]. Lamp1 is a lysosomal marker, and it has been observed that NPC cells can exocytose lysosomes and lysosomal content following cholesterol overaccumulation[113]. To confirm that our observation was due to the presence of increased Lamp1-positive EVs and not co-isolated lysosomal proteins, we repeated MBFC on total cell culture media without performing EV enrichment. This revealed a new set of upregulated (Sulfatide lipids) and downregulated (NCAM1, CD44, ANPEP) surface markers, of which the lipid class Sulfatides and protein CD44 significantly correlated with NPC1 expression (**Fig 3.9A, Supplementary Fig S3.6**). However, neither Lamp1 nor ICAM-1 was differentially expressed in conditioned media (**Fig 3.9B, C**), nor were their media expression values correlated with NPC1 expression (**Fig 3.9D, E**).

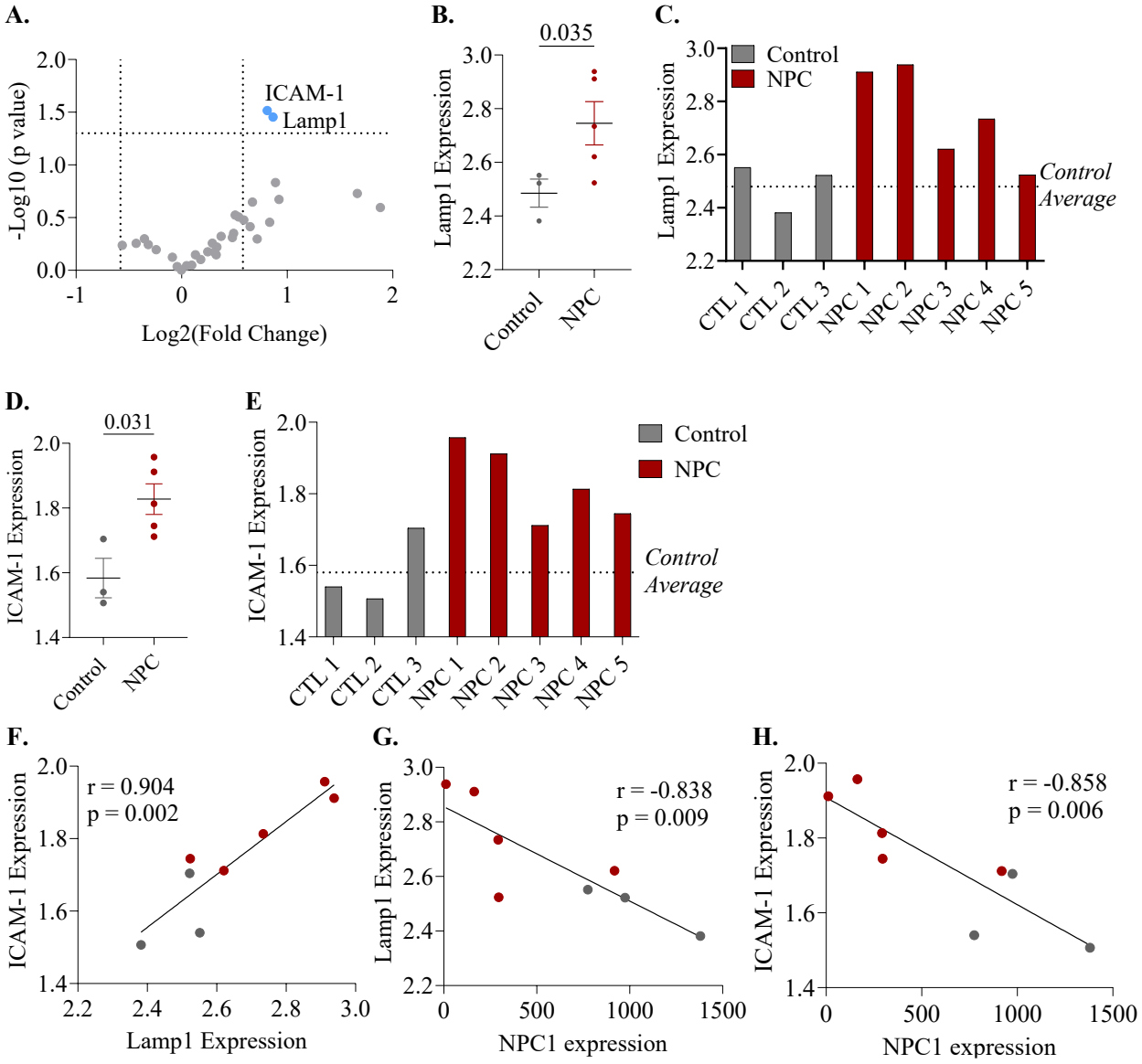

Figure 3.8: Increased Lamp1 and ICAM-1 expression on NPC fibroblast EVs. A) MBFC compared expression of 33 surface markers NPC and control EVs from each cell line. Plot represents uncorrected Welch's t-test; dashed lines represent thresholds for statistical significance ($P<0.05$) and meaningful fold changes. Light blue dots indicate upregulated proteins. **B)** Quantification of Lamp1 EV expression by Welch's t-test. Symbols represent normalized value of individual samples (average of two replicates); bars represent the mean ± SEM of each group. **C)** Lamp1 expression in individual EV samples. Dashed line corresponds to the mean expression of all control samples. **D)** Quantification of ICAM-1 EV expression by Welch's t-test. Symbols represent normalized value of individual samples (average of two replicates); bars represent the mean ± SEM of each group. **E)** ICAM-1 expression in individual EV samples. Dashed line corresponds to the mean expression of all control samples. **F-H)** Pearson's correlations of Lamp1 and ICAM-1 expression (panel F), Lamp1 and NPC1 expression (panel G), and ICAM-1 and NPC1 expression (panel H). Red dots correspond to NPC samples; gray dots correspond to controls. Black lines represent simple linear regression. P-values and Pearson's r are depicted on each graph.

We next investigated whether elevated Lamp1 expression in fibroblast EVs was reflective of altered cellular expression. Immunoblots on cell lysate showed that Lamp1 expression is not altered in the fibroblast cells (**Fig 3.10A-B**), nor does Lamp1 cellular expression correlate with NPC1 cellular expression (**Fig 3.10C**). While other studies have reported that CD treatment increases Lamp1 expression in NPC fibroblasts[100], our preliminary analysis on Control 2 and NPC2 cells suggests little impact of CD treatment on Lamp1 positivity in EVs (**Supplementary Fig S3.7**). Together, these findings indicate that there is an EV-specific elevation of Lamp1 in fibroblasts in relation to loss of NPC1.

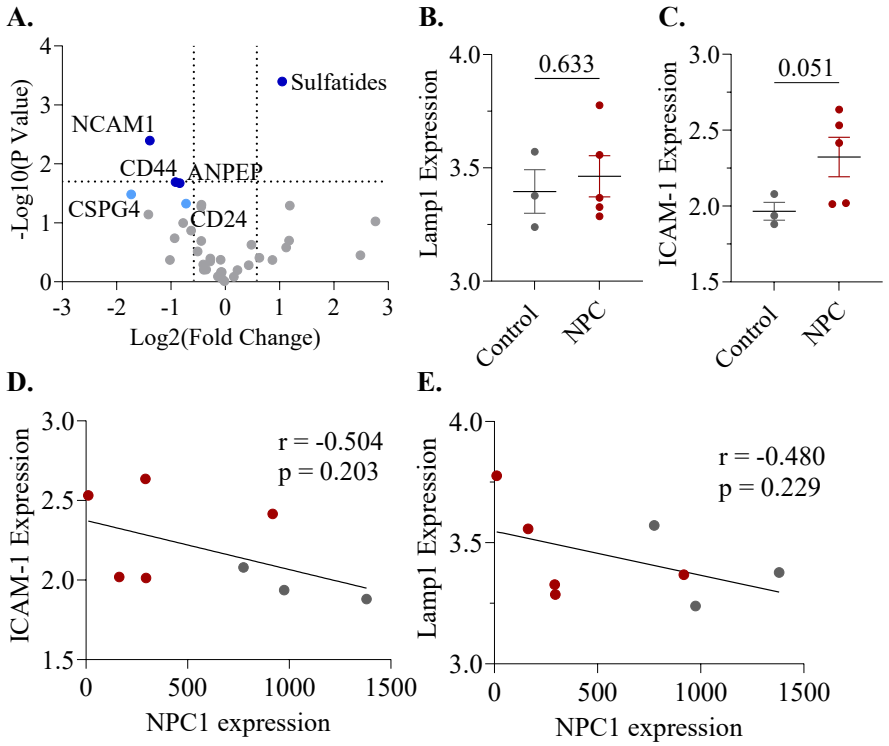

Figure 3.9: Marker expression in unfractionated fibroblast media differs from EVs A) MBFC was used to compare the expression levels of 37 different proteins total conditioned media collected from each NPC and control cell line. Plot represents Welch's t-test; dashed lines represent thresholds for statistical significance and meaningful fold changes. Dark blue dots indicate significantly up- or down-regulated proteins. Light blue dots represent proteins with $p<0.05$ that failed FDR with 20% BH correction. **B-C)** Lamp1 (B) and ICAM1 (C) do not show differential expression in conditioned media (Welch's t-test). **D-E)** Lamp1 (D) and ICAM1 (E) are not significantly correlated with cellular NPC1 expression (Pearson's r). Red dots correspond to NPC samples; gray dots correspond to controls. Black lines represent simple linear regression.

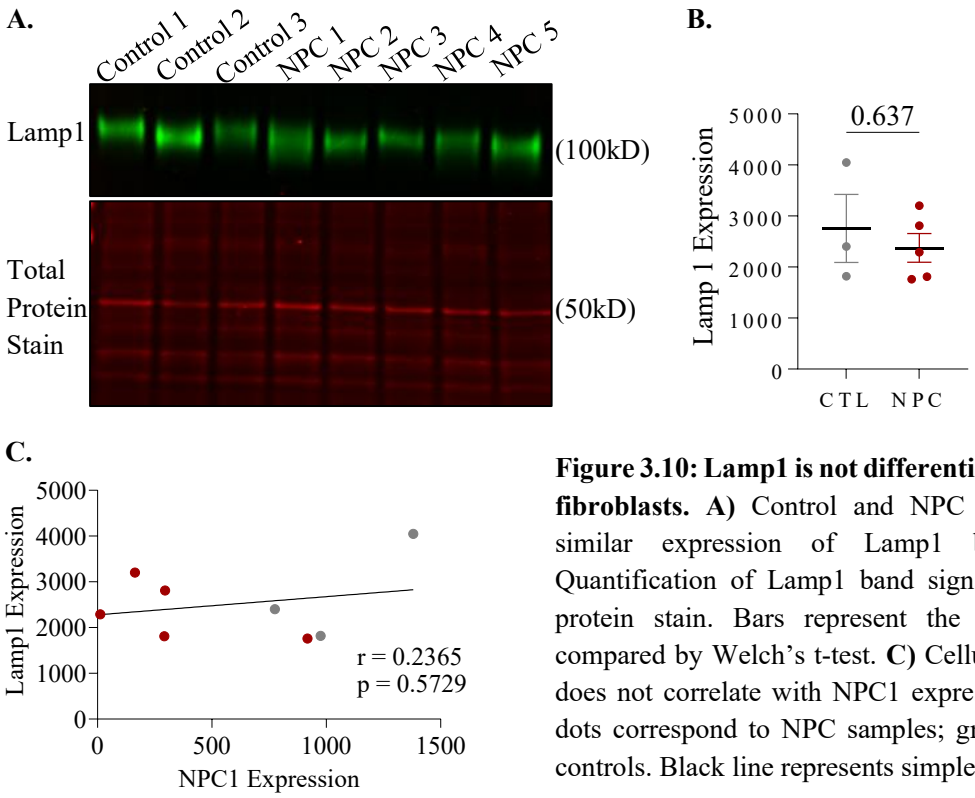

Figure 3.10: Lamp1 is not differentially expressed in NPC fibroblasts. A) Control and NPC fibroblast lines show similar expression of Lamp1 by immunoblot. **B)** Quantification of Lamp1 band signal normalized to total protein stain. Bars represent the mean ± SEM. Data compared by Welch's t-test. **C)** Cellular Lamp1 expression does not correlate with NPC1 expression (Pearson's). Red dots correspond to NPC samples; gray dots correspond to controls. Black line represents simple linear regression.

3.3f: MiRNA Profile of NPC EVs is Distinct from Parent Cells and Healthy Controls

We and many others have demonstrated that EV miRNA content is related to disease pathology[92, 114, 115], and research in mouse models and one patient fibroblast line has shown that NPC causes alterations to cellular miRNA expression[87, 88]. In the previous chapter, we also identified two miRNAs differentially expressed in NPC CSF. We thus sought to investigate whether any miRNAs previously implicated in NPC are alternatively expressed in EVs from our cohort of fibroblasts.

Prior to EV testing, we first determined whether miRNAs previously implicated in NPC were differentially expressed in our three control and five NPC cell lines. We used premade qPCR arrays that contained 377 miRNAs commonly expressed in human samples, and which included all but one miRNA (885-5p) that we screened for in our custom qPCR CSF analysis. Total RNA was isolated from each cell line, and equal amounts were analyzed by the qPCR

premade array. Of the 377 miRNAs screened, 178 passed the qPCR quality control metrics and were analyzed for differential expression (**Fig3.11A**). We identified three miRNAs significantly upregulated in NPC fibroblasts relative to controls: miRs-365-3p, -654-3p, and -598-3p (**Fig 3.11A-D**). Only one miRNA (34c-5p) was significantly downregulated in NPC fibroblasts (**Fig 3.11A)**, but it did not pass multiple-comparisons correction. Four additional miRNAs (miR-652-3p, -493-3p, -134-5p, -127-3p) were significantly upregulated but did not pass multiple-comparisons correction (**Fig 3.11A)**. None of the miRNAs differentially expressed in our cell lines have yet been implicated in NPC.

Next, we investigated whether the three miRNAs upregulated in NPC fibroblasts were altered in fibroblast EVs. SEC was used to isolate EVs from conditioned media of each cell line and total RNA was extracted. There was no difference in the total amount of RNA isolated from controls and NPC EVs (**Fig 3.12A**). Out of 377 miRNAs, 22 passed our quality control metrics and were analyzed for differential expression (**Fig 3.12B**). Interestingly, the miRNAs that were

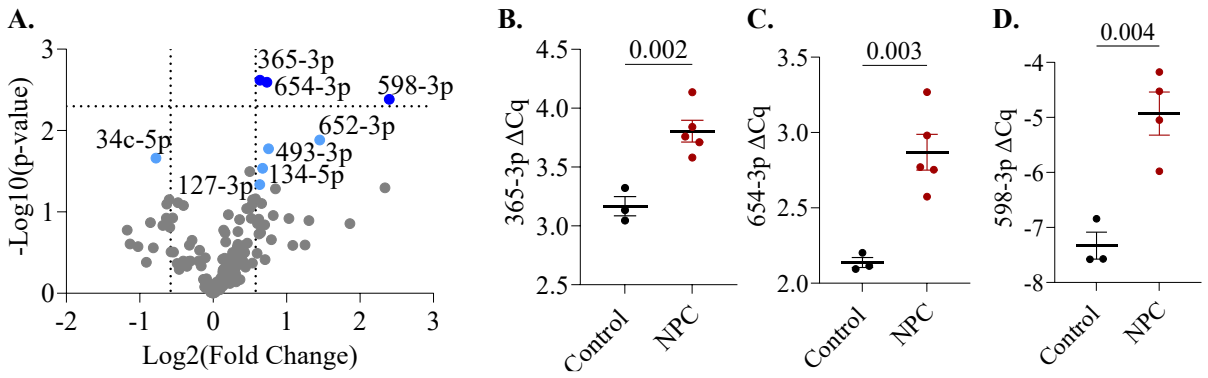

Figure 3.11: MiRNAs are differentially expressed in NPC fibroblasts. MiRNA content of control and NPC fibroblast cells were analyzed by qPCR array. **A)** MiRNAs expressed in NPC versus control cells. Dashed lines represent thresholds for statistical significance (Welch's t-test with 20% BH FDR) and meaningful fold changes. Dark blue dots indicate significantly upregulated miRNAs that passed FDR; light blue indicates significantly upregulated miRNAs that failed FDR. **B-D)** Differentially expressed miRNAs (B) 356-3p; (C) 654-3p; and (D) 598-3p (Welch's t-test). Each symbol represents normalized signal of individual cell lineage (average of technical duplicates). Lines represent the mean ± SEM of control (grey) and NPC (red) samples.

differentially expressed in fibroblast cells were not expressed at detectable levels in fibroblast EVs. We did observe a two-fold downregulation of miR-376a-3p in NPC fibroblast EVs relative to controls (**Fig 3.12B**), though this result did not pass multiple comparisons (**Fig 3.12C**). Together, these results show that miRNA content is distinct between NPC and controls, as well as between EVs and cells.

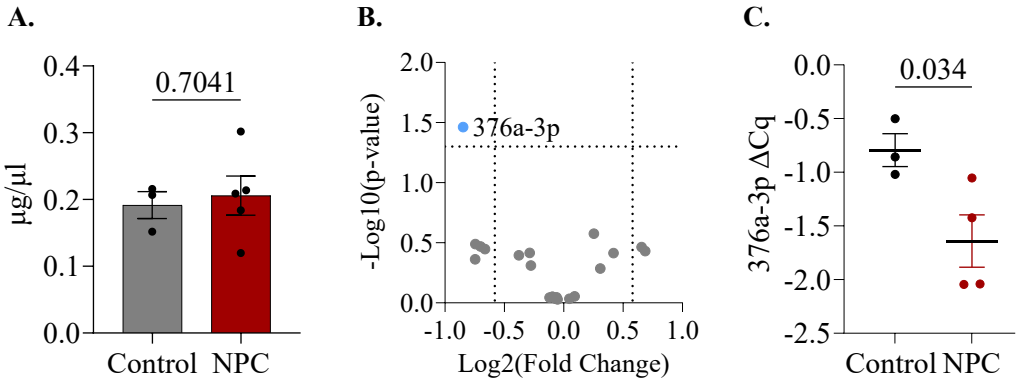

Figure 3.12: MiRNA 376a-3p is downregulated in NPC fibroblast EVs. MiRNA content of EVs isolated from individual control and NPC fibroblasts were analyzed by qPCR array. **A)** There is no difference in the total amount of RNA isolated from control and NPC EVs (Welch's t-test). **B)** MiRNAs expressed in NPC versus control CSF EVs. Dashed lines represent thresholds for statistical significance and meaningful fold changes. Blue dots indicate significantly upregulated miRNAs. **C)** Individual graph of miR-376a expression. Each symbol represents normalized signal of individual cell lineage (average of technical duplicates). Lines represent the mean ± SEM of control (grey) and NPC (red) samples.

3.4: Discussion

These studies are the first to demonstrate changes to EV concentration and cargo in a larger cohort of NPC patient fibroblasts. The only known study to investigate EVs in NPC fibroblasts found that an NPC patient fibroblast cell line released increased EVs into conditioned media (quantified by immunoblot)[72]. The NPC donor in this study was heterozygous for the P1007A mutation, which results in the "variant" NPC phenotype characterized by mild cholesterol accumulation, and a truncation mutation R934*X,* which would delete the lysosome-targeting sequencing from NPC1[17]. Although we do not know the amount of NPC1 expression in this cell line, these findings are generally in agreement with our discovery that decreased NPC1 expression correlates with increased EV release (**Fig 3.5E, F**).

In this study, the opportunity to connect genotype, clinical data, and our EV results with NPC1 expression by immunoblot provided interesting results. We first noticed that although low NPC1 expression is often correlated with earlier age of onset, this trend was not always true in our samples. For example, patient NPC-2 had almost no NPC1 expression, yet age of onset was 31; by contrast, NPC-3 expressed NPC1 at control levels, yet had an earlier age of onset at 16. One possible explanation is that age of onset, as provided here, refers specifically to the age at which patients first present neurological symptoms[5]. It does not consider peripheral symptoms, such as spleen and liver issues, which are more common in younger patients with severe cases[4]. Age of onset is also not the age of diagnosis, and must sometimes be estimated by primary caregivers. Finally, it is possible that our sample size of five patients (four with known ages of onset) is simply too small to observe the trends between protein expression and age of onset that are generally applied. This latter point underlines the challenges of working with small sample sizes for highly heterogenous rare diseases.

However, including additional patients can introduce its own challenges. Our fibroblast cells from five NPC patients had variable growth patterns, with two cell lines in particular showing extremely slow growth rates (**Fig 3.2C**). Interestingly, these were not the same cell lines that had the lowest NPC1 protein expression, indicating there are additional factors that contribute to cell growth. Many studies have shown that EV release *in vitro* can be altered by cell culture conditions, including seeding density, confluency, and cell age[116]. Thus, our EV collections from the fibroblasts had to be carefully controlled and performed relatively early in the growth phase of most cell lines, to ensure that EVs were collected form a similar number of cells at similar densities. Primary fibroblasts are not growth-inhibited cells and can typically survive for weeks in culture; whether we would obtain the same results from more mature cultures is unknown. These considerations also complicate the interpretation of previous publications on EVs and NPC cell lines, as cell culture parameters are not always fully documented.

It is interesting to note that the correlation between NPC1 protein expression and EV concentration was also true in our control cell lines. This indicates that the relationship between NPC1 and EV release is not dependent on NPC disease conditions but may be due to a more fundamental cellular pathway.

We also found that CD treatment of NPC fibroblasts lowered EV concentrations to near control levels (**Fig 3.7B**). However, this study was limited to an NPC cell line that had increased EV release compared to control fibroblasts. Whether CD would affect EVs from NPC cell lines that do not release increased EVs versus controls is unknown. CD enters the cell through endocytosis and is delivered directly to endolysosomes, where it is thought to improve NPC pathology by redistributing cholesterol and other lipids from endolysosomes to other sites in the

cell[80]. Animal models, which typically use a full knockout of the NPC1 protein, have shown CD to be highly effective at combating NPC pathology and in some cases extend the lifespan up to 120%[99]. However, results in human patients have failed to show consistent results. Our results may indicate that the effectiveness of CD treatment – which we measured as a return-to-baseline EV concentration – may be dependent on the severity of NPC1 protein loss. Other limitations of these experiments include the use of a single dose of CD and single duration of treatment, as well as the use of fibroblasts rather than neuronal cells.

It is interesting to observe that the EV surface markers present in our SEC-isolated EVs showed no overlap with markers found in total conditioned media (**Fig 3.8A, 3.9A**). Our method of marker detection (MBFC) uses fluorophores conjugated to the tetraspanins CD63, CD81, and CD9, which are commonly enriched on EVs. Yet these markers can be expressed on non-EV nanoparticles; for example, CD81 is expressed on the non-membranous exomeres[117]. They can also be expressed on larger EVs, such as microvesicles and apoptotic bodies, which would be removed during our EV isolation protocols but could be present in the total conditioned media[39]. Thus, the total conditioned media likely includes both EV- and non-EV signal. The stark contrast between marker expression in total media versus isolated EVs underlines the specificity of nanoparticle populations, and emphasizes the need to interpret EV studies within the context of their methods for isolation and profiling.

Regardless of whether it is EV- or non-EV bound, the discovery of elevated sulfatide lipids in total conditioned media contributes to a growing body of evidence that cholesterol is not the only lipid altered by NPC pathology (**Fig 3.9A, Supplementary Fig S3.6A**)[23]. Sulfatides (also called glycosphingolipid sulfates) are a class of acidic glycosphingolipids (GSLs) found primarily in the outer leaflet of the plasma membrane[118]. GSLs are well-known to accumulate

alongside cholesterol in NPC endolysosomes and have been implicated in other neurodegenerative and lysosomal storage diseases, including metachromatic leukodystrophy[119]. In fact, some studies have suggested that GSL accumulation is a primary defect of NPC cells[68, 120]. Our data showing that sulfatide is enriched in NPC fibroblast media, and indirectly correlate with NPC1 expression, support the role of this lipid in NPC (**Supplementary Fig S3.6A, E**).

Within our SEC-isolated EVs, we observed significant enrichment for Lamp1 and ICAM-1, both of which correlated with NPC1 expression (**Fig 3.9**). In agreement with other work, we also found that there is no difference in cellular expression of Lamp1 in NPC, suggesting that this change is specific to EVs (**Fig 3.10**)[95]. It is possible that these findings reflect specific packaging of Lamp1 into NPC EVs. However, Lamp1 may only be elevated in NPC endolysosomes, which immunoblotting of whole cell lysate may not be sensitive enough to detect. This has been the case of other endolysosomal disruptions in NPC, such as lipid enrichments, which can only be observed by specifically probing endolysosomes[80]. Thus, an alternative hypothesis may be that elevated EV Lamp1 is driven by an increase in Lamp1 in the membranes of endolysosomes, which then produces Lamp1-enriched exosomes.

Finally, we observed that miRNA expression differed significantly between NPC and control fibroblasts, as well as between fibroblasts and EVs (**Figs 3.11, 3.12**). None of the miRNAs differentially expressed in fibroblast cells were expressed at detectable levels in fibroblast EVs, which agrees with previous studies highlighting the specificity of EV miRNA packaging[62, 115]. Only one miRNA, miR-376a, showed a trending decrease in NPC EVs over controls. Although not previously linked to NPC, miR-376a is dysregulated in other lipid disorders, including an upregulation in diseases marked by high levels circulating cholesterol in the serum[121-123]. Our data demonstrates that the inverse is also true: when cholesterol is

sequestered in endolysosomes and not available to the rest of the cell, 376a is downregulated. These data could suggest a role for 376a in pathways of cholesterol homeostasis. Further investigation, potentially in a larger cohort of patients, will be needed to determine the significance of miRNA 376a in NPC.

Together, these studies demonstrate that NPC pathology may alter the concentration and molecular cargo of EVs. Many of the EV changes we observed are correlated with NPC1 protein expression, suggesting that NPC1 protein function and EV release are fundamentally intertwined. A better understanding of how NPC affects EVs could provide novel insight into disease biology, and potentially identify new therapeutic targets or disease biomarkers.

3.5. Materials and Methods

3.5a: Cell Culture

Primary dermal fibroblasts were sourced from skin biopsies of the upper arm. Cells were acquired either from Rush University Medical Center or the Coriell Institute of Medical Research as indicated in **Table 3.1**. Cells were maintained in DMEM with 10% fetal bovine serum in coated tissue-culture flasks. To passage cells, flasks were washed with PBS and incubated with 0.05% trypsin for 5 minutes at 37°C. Trypsinized cells were spun at 300xg for 5 minutes, resuspended, and plated onto new dishes. Cell counts and viability were obtained by trypan blue staining and a CellDrop Cell Counter (DeNovix). For CD treatments, fibroblasts were treated with 500μM CD or water as vehicle for 48 hours.

3.5b: Fibroblast Sanger Sequencing

Prior to beginning experiments genetic mutations in the *NPC1* gene were confirmed in each fibroblast cell line. Genomic DNA was extracted from cultured NPC patient primary fibroblast cell pellets using the Genomic DNA Purification Kit (Monarch) following the

manufacturer's instructions. The DNA concentration (UV 260 x 50) and purity (ratio of UV 260/280 nm) of each sample was determined using a Nanodrop 2000 (ThermoFisher Scientific, TFS). Samples were either stored at -20°C or used immediately for downstream Polymerase Chain Reaction (PCR).

For the PCR, 100 ng of the extracted DNA sample (NPC or control) was added to thin-walled PCR strips containing 12.5 µl of 2X RedTaq PCR master mix (Sigma), 1 µl of forward primer (20 pmol/µl),1 µl of reverse primer (20 pmol/µl) and water to a final reaction volume of 25 µl. Each primer set is specific to 1 of the 7 mutations found in the NPC patient set. The PCR was run using a 40-cycle touchdown PCR program on a BioRad T-100 thermocycler. Program details are given in **Table 3.3.**

PCR products were visualized using a 1.0% agarose gel containing SybrSafe intercalating dye. 20 µL of each PCR product was loaded into the gel alongside a 1Kb DNA ladder for sizing. The gel was run at 150 volts for 20 minutes. The resulting DNA bands were visualized and imaged using a UV transilluminator. Bands were confirmed as the correct size and excised from the gel using a razor blade and placed into individual Eppendorf tubes.

Table 3.3: PCR program steps.

1.	98° C	3 mins
2.	98° C	30 sec
3.	65° C	30 sec
-1° C per cycle		
4.	72° C	45 sec
5.	GOTO step 2	10X
6.	96° C	30 sec
7.	54° C	30 sec
8.	72° C	45 sec
9.	GOTO step 6	29X
10.	72° C	5 mins
11.	4° C	HOLD

DNA was purified from the gel slices using a DNA Gel Extraction Kit (New England Biolabs) following the manufacturer's instructions. DNA was eluted with 10 µl of Tris-EDTA (TE) and the DNA concentration (UV 260 x 50) and purity (ratio of UV 260/280 nm) of each sample was determined using a Nanodrop 2000 Spectrophotometer (TFS). PCR product DNA was stored at -20°C until use.

Sanger sequencing was performed at OHSU's Vollum Sanger Sequencing core following their sample preparation instructions. Briefly, 10-20ng of each DNA sample was mixed with water and its respective forward and reverse primers (3.2 pmol) in separate reaction tubes at a final volume of 9µl. The reaction tubes were delivered to the core lab, and the sequencing results were sent as both a text file and a chromatogram file. Chromatogram files were opened using the freeware viewer Chromas. Mutations were confirmed by trimming the sequence ends and searching for ~5 base pairs upstream of the mutation site. Heterozygous mutations appeared as a double peak.

3.5c: Dermal Fibroblast EV Enrichment

To prepare cells for EV collection, $5x10^5$ cells/mL were seeded into T75 flasks and grown for 4-6 days. Two days prior to EV collection media was exchanged for DMEM with 10% EV-depleted FBS (System Bioscience EXO-FBS-250A-1). Twelve mL of conditioned media was collected from each flask and spun for 10 minutes at 300xg; the supernatant was removed and then spun for 10 minutes at 3,000xg for 10 minutes; the supernatant was again removed and passed through a 0.22µM filter. Processed conditioned media was then stored at -80°C.

Prior to EV isolation, processed conditioned media was thawed at room temperature and concentrated to <500µl using 100kD AmiconUltra-15 columns (Millipore-Sigma UFC910024). Concentrated media was then spun at 10,000xg for 10 minutes and brought to a final volume of 500µl with phosphate-buffered saline (PBS).

EV isolations were performed using Original 35nm Gen2 columns (Izon ICO-35). Prior to use columns were brought to room temperature and washed with 17 mL of PBS. 500µl of concentrated conditioned media was applied to the column and allowed to enter the frit. Next, 2.5 mL of PBS was applied to the column and collected as void, followed by 1.6 mL of PBS to

collect the EV and protein fractions. After collection, EV fractions were further concentrated in 30kDa concentrator columns until desired volume was reached (Millipore-Sigma MRCFOR030).

3.5d: Immunoblots

Protein concentrations were measured using the Qubit protein assay kit and Qubit 4 fluorometer (TFS). Gel electrophoresis was performed using 4-12% Bis-Tris gels. Gels were run at 125 volts at room temperature in MOPS buffer. Proteins were transferred to PVDF membranes (Millipore Sigma) in NuPage transfer buffer (Invitrogen) with 10% methanol for 2 hours at 100 volts at 4°C. PVDF membranes were dried overnight at 4°C and reactivated with methanol. Membranes were stained with 700 Revert Total Protein Stain (LI-COR Biosciences) and imaged on the Odyssey CLx Imager, then destained and blocked with Intercept Blocking Buffer (LI-COR Biosciences). Membranes were then incubated with primary antibodies overnight at 4°C in Intercept Blocking Buffer with 0.2% Tween-20. After four 5-minute washes (TBS with 0.2% Tween-20) membranes were incubated with IRDye secondary antibodies (LI-COR) in Intercept blocking buffer with 0.2% Tween-20 and 0.02% SDS for 1 hour at room temperature. After another four 5 minute washes (TBS with 0.2% Tween-20) membranes were imaged on the Oldyssey CLx Imager. Quantification of band signal was performed using the Quantify Western Blot application on the Empira Studio software (version 2.2, LI-COR Biosciences). Automatic lane detection, automatic band detection, background subtraction, and normalization to total protein stain were applied to generate the final normalized band intensity. The following antibodies were used: NPC1 (EPR5209) 1:1000 (134113, Abcam); CD63 (H5C6) 1:5,000 (556019, BD Biosciences); CD81 (B-11) 1:100 (sc-166029, Santa Cruz Biotechnology); Flotillin-1 1:10,000 (ab133497, Abcam); GM130 1:1000 (53420SS, Novus Biologicals); and

Lamp1 (D2D11) 1:1000 (9091S XP, Cell Signaling Technology). Secondary antibodies were purchased from LI-COR IRDye 800CW and IRDye 680RD and used at 1:20,000.

3.5e: Microchip Resistive-Pulse Sensing

MRPS was performed using the nCS1™ Particle Analyzer and C-400 microchips (Spectradyne Particle Analysis). Prior to use the instrument was primed with 1X PBS without calcium and magnesium containing 1% Tween-20 (running buffer) using the supplied cleaning cartridges cleaning cartridges and lines were flushed. For analysis, SEC-isolated fibroblast EVs were diluted 1:5 in running buffer and run on the nCS1. At least 500 particles were collected per sample.

Data was analyzed using the nCS1 Data Viewer software, version 2.5.0.325. To control for variation in microchip lots, 150nm calibration beads of known concentration were run alongside samples in C-400 microchips of matching lots. Discrepancies between actual and measured size and concentration of the calibration beads were used to generate correction factors that were applied to each sample. To generate histograms of particle size and concentration, samples were background-subtracted and scaled to their respective correction factors. The gaussian distribution of particle concentration and size was obtained. Particles over 200nm were excluded as noise.

3.5f: Vesicle Flow Cytometry

EV concentration, size, and tetraspanin expression was measured by VFC using commercially available kits (vFC Assay Kit, Cellarcus Biosciences). Fibroblast EVs were incubated at a final concentration of 1:10 with a lipophilic membrane dye pre-diluted 1:10 (vFred) and PE-conjugated anti-tetraspanin (CD63/CD81/CD9) antibody pre-diluted 1:4 for 1 hour at 27°C. Samples were then diluted in buffer to a final dilution of 1:100 and analyzed in an

Amnis CellStream flow cytometer (Cytek) using small particle detection mode. Spectral compensation was performed using stained antibody capture beads and validated by single-stain controls. Events were recorded for 120 seconds. Forward and side scatter lasers were set to zero; remaining lasers were set to 100. All samples were run in triplicate wells. Negative controls for each run included unstained samples, membrane-dye only samples, and samples with lysis buffer. Positive controls for each run included platelet-derived EVs and synthetic 100nm lipo- (Cellarcus Biosciences).

Data analysis was performed using FCS Express 7 Research Edition and templates provided by Cellarcus Biosciences. A summary of analysis settings and gating strategies is provided in **Supplemental Figs 3.2-3.5**.

3.5g: Multiplexed Bead-Based Flow Cytometry

MBFC was performed using commercially available kits and reagents as per the manufacturer's instructions (Miltenyi Bioscience MacsPlex EV Human Neuro kit). 120µL of isolated EVs or total conditioned media was incubated with antigen-coated capture beads overnight at room temperature on a rotator (Miltenyi Biosciences). After repeated washings, samples were then incubated with fluorophore-conjugated detection beads against CD63, CD81, and CD9. For isolated EVs, sample buffer was processed identically to samples and used as negative control. For conditioned media, blank DMEM with 10% EV-depleted FBS was processed identically to samples and used as negative control. Flow cytometry was performed on a BD Biosciences LSR II with the following laser settings: forward scatter 350, side scatter 200, 488-1 360, 488-2 520, 633-1. Events were collected for 120 seconds with run speed at low.

Data analysis was performed using FlowJo version 10.10.0. The median value of the allophycocyanin (APC) channel in each population was extracted. The negative control values

were subtracted from each sample and values were log10 transformed. Populations with APC values equal to buffer were considered not expressed; populations with APC values below buffer were considered technical failures and removed from the analysis. Populations that had APC values greater than buffer were considered expressed. Only proteins expressed in at least seven of eight samples were analyzed.

3.5h: RNA Isolation

Fibroblast EVs were isolated through SEC as described and 500µl was used for miRNA analysis. RNA was extracted from EVs using the Urine miRNA Purification Kit (Norgen Biotek Corp), according to the manufacturer's instructions. Prior to final RNA elution samples were incubated with 30µL of elution buffer for 10 minutes at room temperature. To confirm successful isolations, 2µL of eluted RNA was analyzed using the Qubit miRNA assay kit and Qubit 4 fluorometer (TFS). Isolated RNA was stored overnight at -20°C prior to qPCR.

For fibroblast cell studies RNA was extracted from cell pellets. Approximately $2x10^6$ cells were pelleted, flash frozen in liquid nitrogen, and stored at -80º until used. RNA was extracted from cell pellets using the Total RNA Purification Kit (Norgen Biotek) according to the manufacturer's instructions. RNA was eluted in 50µl of elution buffer. Final RNA concentration and purity was confirmed using a NanoDrop 2000 Spectrophotometer (TFS). RNA was frozen at -20º until use. Equal amounts of RNA from each cell line were then analyzed by qPCR.

3.5i: MiRNA qPCR

Fibroblast and fibroblast EV miRNA was analyzed by TaqMan qPCR arrays (TFS). MiRNA was converted to cDNA using the TaqMan Advanced miRNA cDNA Synthesis kit (A28007, TFS). Briefly, 3µL of total RNA was 3' poly-adenylated, followed by a 5' adaptor ligation step and reverse transcription. The resulting cDNA (5µL) was added to a 14-cycle

universal miR-amplification step. The miR-amplification reaction was diluted 1:10 with nuclease free water, 220µL of the diluted cDNA was mixed with 220µL of nuclease free water and 440µL of TaqMan Fast Advanced master mix (4444556, TFS). The qPCR mix (100µL) was loaded into each of the 8 ports of a TaqMan Advanced miRNA Human A Card (A34714, TFS). All cards included a primary endogenous normalization control (miR-16-5p), an exogenous spike-in calibration control (cel-39-3p), and an exogenous negative control (plant ath-miR159a). Each card was assayed using a QuantStudio 7 Flex Real-Time PCR System (4485695, TFS) with the aid of an Orbitor RS2 Microplate Mover (ORB2001, TFS) to increase throughput and ensure each RNA isolation batch was processed on the same day. As a negative control, one card was run as described with water included in place of RNA.

3.5j: MiRNA Analysis

QuantStudio 12K Flex Software v1.3 and ExpressionSuite software v1.3 was used to process the qPCR data. MiRNA amplification values were calculated from the quantification cycle (Cq; number of PCR cycles before signal surpasses background) using automated baseline and threshold values determined by ExpressionSuite. MiRNAs with $Cq \leq 34.000$ were considered expressed. MiRNAs that showed no amplification ("undetected") or had Cq values over 34.000 were considered not expressed and censored at Cq=34. Amplification quality, calculated by Expression Suite, was further evaluated by Amplification Score (signal quality during the linear phase of amplification) and Cq Confidence (statistical confidence in the Cq value). MiRNAs with an Amplification Score < 0.950 and/or a Cq Confidence < 0.750 were considered technical failures and removed from analysis. We also verified that there was little to no amplification in the exogenous negative control in each sample (plant ath-miR159a).

After filtering, miRNAs with good quality amplifications were calibrated and normalized. To control for technical variation in the quality of RNA isolation between samples, Cq values were calibrated with two normalization factors calculated for each sample: the Cq of the exogenous spike-in miRNA (cel-miR-39-3p); and the median Cq of all miRNAs that showed good quality amplification in all samples (n=24).

Sample normalization was performed by calculating the average expression of 4 endogenous controls for each sample. Endogenous controls were selected by identifying which miRNAs showed the most stable Cq values across all samples. The average endogenous Cq value was then subtracted from the Cq values of each miRNA to generate ΔCq. To compare expression between control and NPC samples, the ΔΔCq was calculated by subtracting the ΔCq of the control from the ΔCq of the NPC samples. The fold change (RQ) was calculated by using the $2^{\Delta\Delta Cq}$ method, with RQ > 1 indicating increased miRNA expression. Statistical significance was calculated by comparing the ΔCq of the control replicates with the ΔCq of the NPC replicates (Welch's t test). Data is shown as a Volcano plot (−Log10 (q-value) vs. the Log2(Fold change)) and the ΔCq mean ± standard error mean (SEM).

3.5k: Statistical Analysis

For VFC, MBFC, and miRNA experiments the samples were randomized and the experimenter was blinded to group and sample identity. Data were analyzed with GraphPad Prism software v10.1.0 (GraphPad Software, Inc). Cell culture experiments were repeated 1-3 times as indicated in figure legends and results were averaged. Statistical tests were performed as indicated in legends. To compare between two groups Welch's t-test was used; for analyses involving more than four t-tests a false-discovery rate (FDR) of Benjamini-Hochberg (BH) 20% was applied. Comparisons between more groups in VFC analysis was performed using two-way

ANOVAs with Tukey's correction. Relationships between two variables were assessed using Pearson's correlation tests and simple linear regression.

3.6. Supplementary Figures

Figure S3.1: Confirmation of *NPC1* mutations. Chromatograms display the results of *NPC1* Sanger sequencing in each fibroblast cell line.

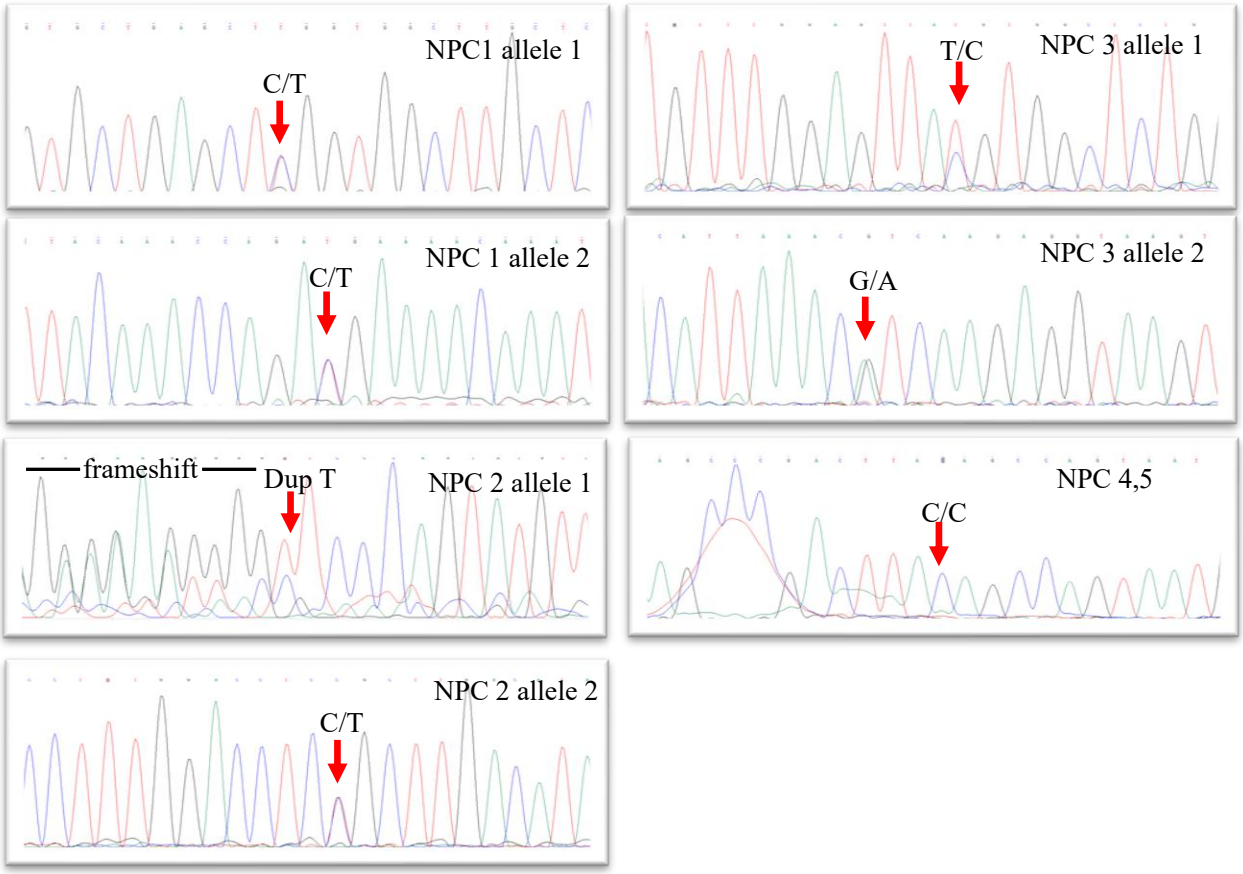

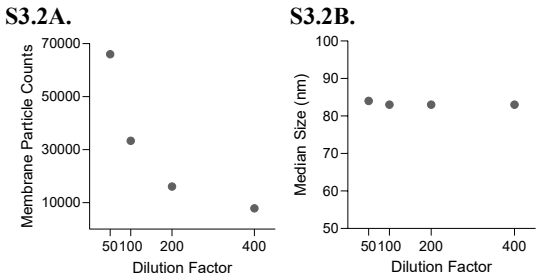

Figure S3.2: Identification of optimal fibroblast EV dilution for VFC. EVs were isolated from fibroblast conditioned media and incubated with membrane dye and tetraspanin antibodies at a final dilution of 1:50, 1:100, 1:200, and 1:400. **A)** In keeping with ISEV recommendations, dilution curves were used to identify the sample dilution that results in ~50,000 particle counts. **B)** Particle size does not change with dilution, confirming high dilutions do not result in particle swarm.

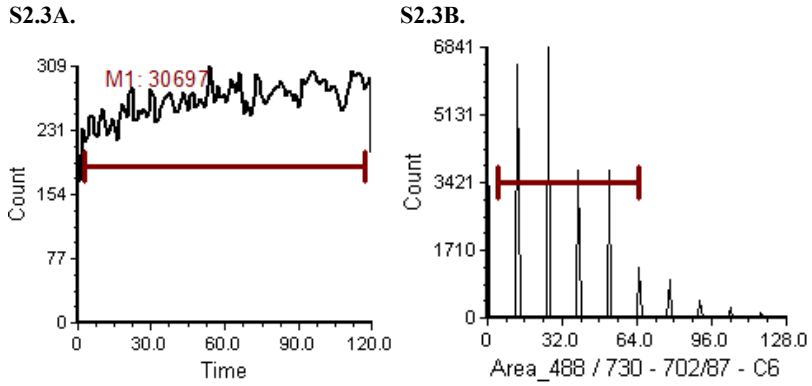

Figure S3.3: VFC time and area gates. A) Time gate of representative fibroblast EV sample. Plot shows number of events occurring over a 120 second run. The time gate (red line) removes the first and last 3 seconds of the run to exclude fluidic anomalies. **B)** Area gate of representative fibroblast EV sample. Plot shows the area of particles occurring the in 488 FITC channel. Area gate (red line) is drawn to exclude background signal with no area, or signal with area greater than 4 pixels (coincident or out of focus events).

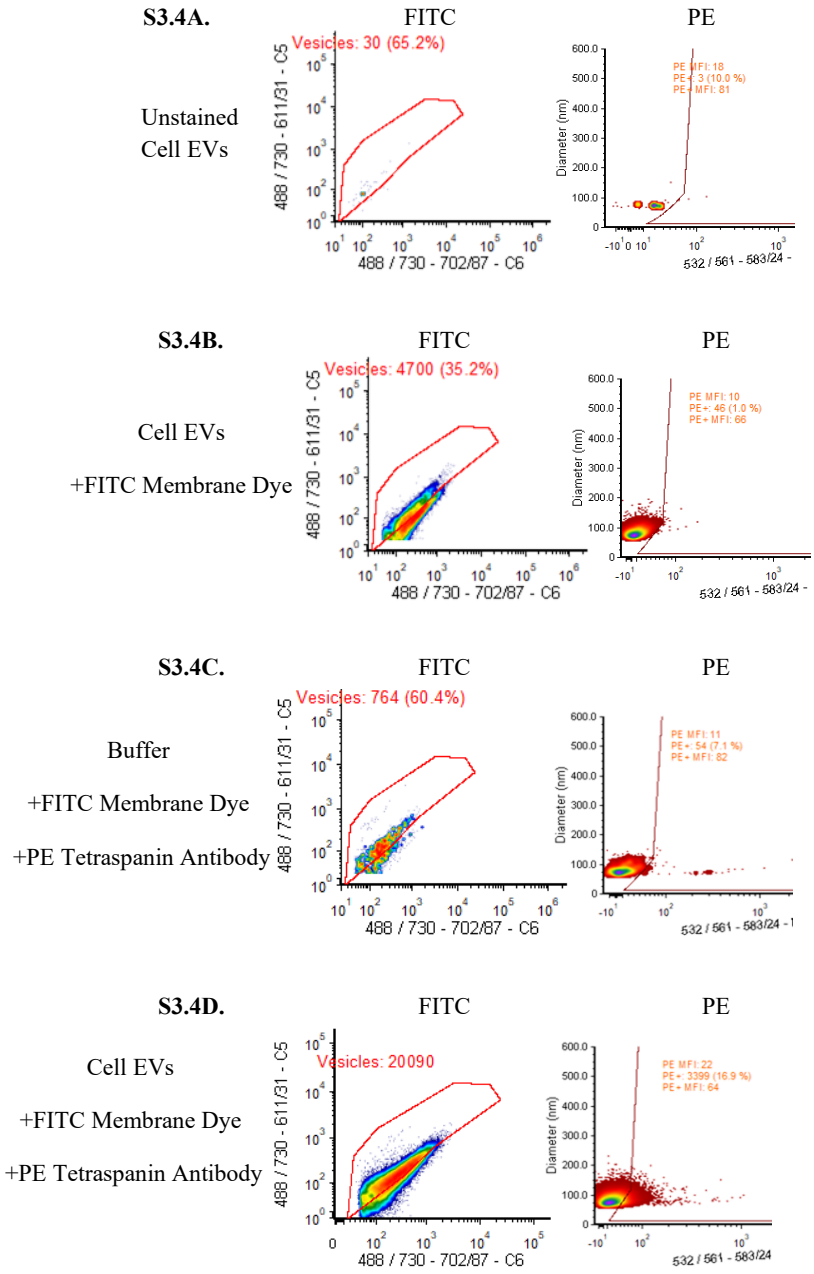

Figure S3.4: VFC background gating strategy. Multiple negative controls are included to ensure background signal is removed. **A)** Unstained fibroblast EVs shows near negative signal in both the FITC and PE channels. **B)** Fibroblast EVs stained only with membrane dye shows strong signal in the FITC channel, as expected. Signal appearing in the PE channel is considered background and gated out. **C)** Buffer stained with both membrane dye and tetraspanin antibodies shows some background signal in both the FITC and PE channels, which is considered background and gated out. **D)** Final gates applied to fully stained fibroblast EV sample allow for the inclusion of true signal and removal of background. Red lines on all plots represent final gates that have been adjusted to remove all background signals.

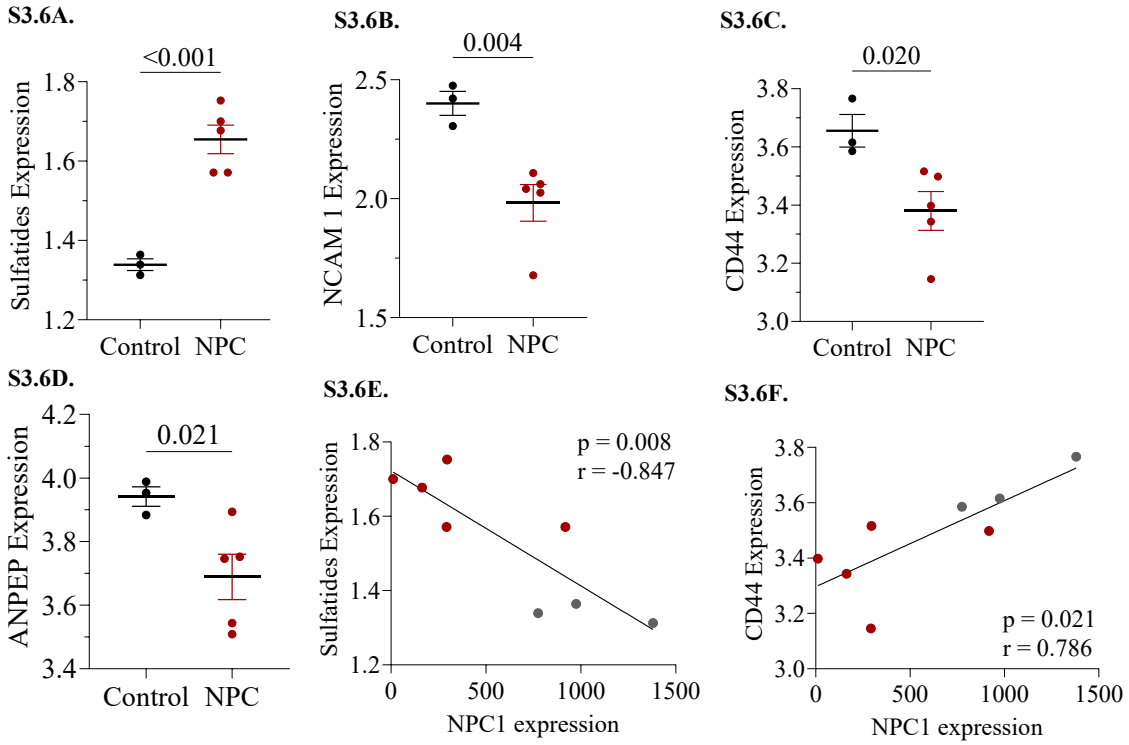

Figure S3.6: Differential marker expression in unfractionated fibroblast media. MBFC was used to compare the expression levels of 37 different proteins in total conditioned media collected from each NPC and control cell line. **A-D)** Differentially expressed markers in NPC conditioned media. Sulfatide lipids (A) are significantly increased in NPC samples; NCAM1 (B), CD44 (C), and ANPEP (D) are significantly decreased (Welch's t-test with FDR 20% BH). Lines represent the mean ± SEM. **E)** Sulfatides are negatively correlated with NPC1 protein expression (Pearson's r). **F)** CD44 is positively correlated with NPC1 expression (Pearson's r). Symbols on all plots represent individual cell lines (average of technical duplicates); red corresponds to NPC samples, gray corresponds to controls.

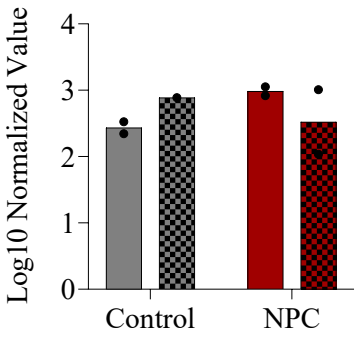

Figure S3.7: CD treatment does not appear to affect Lamp1 EV expression. MBFC was used to compare Lamp1 expression on EVs from Control 2 and NPC 2 fibroblasts. Experiment was repeated twice, as indicated by symbols.

CHAPTER 4: DISCUSSION

4.1: Personal Reflections

In this project, I sought to explore the role of extracellular vesicles (EVs) in Niemann Pick Disease Type C (NPC). I have been told not to use the word "explore" as a scientist, as it suggests that we are casually bumbling around a topic to see what we find. Yet when reflecting on how this research evolved over the past five years, I believe "explore" is exactly the right word – and while there may have been some bumbling, there was nothing casual about it. There are now 18 publications that consider EVs in NPC, but when I began this project in 2020 there were only four. There was very little known on this subject, and the information that did exist was often conflicting. I thus began this project with absolutely no idea what I would find, but with determination to find it. The discoveries I made were thrilling; when they did not replicate (or survive multiple comparisons), I was crushed. And like all good explorers, I never know when to stop. There are always more experiments to do, always new ways to analyze the data, always new publications that change our interpretations. But in this final chapter of my dissertation, I will do my best to put the whole thing to rest. Below are my summaries, conclusions, and best guesses as to the role of EVs in NPC – as well as some ideas for the next explorer.

4.2: EV Concentrations in NPC Samples: Up, Down, Left, Right?

A key goal for this project was to understand how NPC pathology impacts the concentration of EVs. It is a deceptively simple question: seven previous studies have investigated this matter, and found that NPC either increases[72-74], decreases[75, 76], or does not affect[77, 78] EV concentration. Establishing EV concentration in NPC is important for a number of reasons. If EVs are to serve as NPC disease biomarkers, as has been proposed for other neurodegenerative diseases, understanding how the amount of EVs varies between healthy and

disease samples is a key first step[92]. Additionally, establishing differences in EV concentrations is important for interpreting differences in specific EV cargo, as such changes could be due to an increase in overall EVs or to changes in the amount or type of cargo per EV. Finally, identifying changes to EV concentration could provide new insight into disease pathology, and ultimately identify new therapeutic targets.

Our experiments show that NPC CSF from living donors contains a significantly higher concentration of EVs than healthy controls. While patient fibroblasts did not show the same result, they did reveal significantly more variability in concentration than controls and an inverse correlation between NPC1 protein expression and EV concentration.

The different observations between NPC EVs in CSF versus fibroblasts could be due to a number of factors. Firstly, it is possible that the relationship between NPC and EVs is tissue- or cell type-specific, especially given the unique central nervous system (CNS) impacts in NPC[21]. It is difficult to know exactly where EVs in CSF come from, as by the time it is collected from the lumbar spine, CSF has come into contact with the most of the brain (including ventricles, subarachnoid space, and arachnoid villi) as well as the epithelial and endothelial cells lining the spinal column [64]. Any cell type in these tissues can theoretically contribute EVs to CSF, and proteomics have shown that CSF EVs express neuronal, microglial, endothelial, and epithelial markers in relatively equal proportion[124]. Our attempts to define the surface marker expression of CSF EVs returned similar results, as there was no clear trend in expression of markers from any one tissue or cell type. In order to determine whether the increase in NPC EVs is CNS-specific, more research in CNS-specific models is needed. Induced pluripotent stem cell (iPSC) neurons generated from NPC patient fibroblasts, which have been recently developed, could be an ideal tool for this question[125, 126].

An alternative explanation for why NPC CSF contained significantly higher EVs than controls while fibroblasts did not is that all of the NPC CSF donors were undergoing treatment with the experimental treatment hydroxypropyl-β-cyclodextrin (CD), which may have influenced the results. However, our experiments in fibroblasts suggest that CD treatment in NPC actually decreases EV release. The NPC fibroblast cell line used in this experiment shared mutations with a CSF sample, and in both CSF and fibroblasts this mutant had the highest EV concentration. Yet it remains possible that the relationship between NPC and EVs is different in fibroblasts than it is in the CNS, with different impacts by CD, and repeating this experiment in a neural model would likely be illustrative.

A third possible explanation is provided by the striking inverse correlation between NPC1 protein expression and EV concentration in fibroblasts. It is unfortunate that we do not know NPC1 expression levels for our CSF patients, as this information could unify our findings. It is possible that the five CSF patients all had similar, low levels of NPC1 protein expression, and that if the study was expanded to a larger and more diverse group of patients the CSF may be more similar to the fibroblasts. The fact that the S733fsX10/ P434L mutant, which had almost zero NPC1 expression, showed the highest EV concentration in both CSF and fibroblasts supports this hypothesis.

In fact, our discovery that NPC1 expression indirectly correlates with EV concentration may explain the disparate results obtained by previous studies. The relationship between EV concentration and NPC has been previously investigated using patient fibroblasts and genetic knockouts[72], mouse models[74, 76], and small molecule inhibitors[73, 75, 77, 78], each of which impacts NPC1 protein expression to a different extent. Even studies that use the same NPC1 inhibitor (U18) had different dosing strategies, which could result in different amounts of inhibition. A

simple dose-response curve with U18 or *NPC1* siRNA may be an effective way to measure the impact of NPC1 inhibition on EV concentration. If performed in multiple cell types (e.g. fibroblasts, iPSC-derived neurons and glia), and mouse models, with or without CD, this experiment could provide definitive, tissue-specific information on the relationship between NPC1 expression and EV concentration, and unify the currently disparate results.

4.3: The LAMP Proteins: Shedding Light on NPC, or Just Shedding EVs?

Our data suggests that perturbations to EVs in NPC are driven, at least in part, by perturbations of the endolysosomes. This is evidenced by *i)* the upregulation of lysosomal-associated membrane protein-1 (Lamp1) on NPC EVs, which we observed in both CSF and fibroblasts; *ii*) the inverse correlation between EV Lamp1 and cellular NPC1 expression in fibroblasts; *iii*) the trending increase of the related protein Lamp4 in NPC CSF; and *iv*) the increase in NPC CSF of EVs positive for CD63, also known as Lamp3, which correlated with patient age of onset. It is well-established that NPC endolysosomes are enriched in Lamp proteins as a consequence of over-accumulation of cholesterol, further supporting the hypothesis that Lamp-positive EVs in NPC are of endolysosomal origin and thus are exosomes[127, 128].

One interpretation of these results is that increased release of Lamp-positive exosomes in NPC is a compensatory mechanism to remove endolysosomal content from over-burdened cells. The logical consequence would be that these exosomes are enriched in cholesterol and other accumulating lipids; while our attempts to measure lipids in NPC EVs were unsuccessful, a recent publication did show that CD63 positive EVs are enriched in cholesterol[56]. Further lipidomic studies on EV subpopulations in the context of NPC would be illustrative.

The compensatory hypothesis is supported by the fact that inhibiting EV release in NPC cell lines increases endolysosomal cholesterol[81], and conversely, that stimulating EV release in

NPC models decreases endolysosomal cholesterol[51, 79]. While removing toxic endolysosomal build-up via exosomes may benefit the releasing cell, consequences for the recipient cell(s) are difficult to predict. Delivery of EVs and their cargo can occur through a number of pathways, including clathrin- and caveolin-mediated endocytosis, micropinocytosis, phagocytosis, uptake via lipid rafts or lectins, and even direct fusion with the plasma membrane[129]. If Lamp-positive, cholesterol-enriched exosomes enter recipient cells through endocytosis, they would exacerbate the cholesterol storage issues already present. However, exosomes taken up by alternative methods may be able to ameliorate the cholesterol starvation experienced at other cellular locations, such as the plasma membrane[130].

Thus, the increased NPC exosomes we observed could have positive and/or negative consequences for disease pathology. The correlation with more severe disease, determined by either age of onset or NPC1 expression, turns this question into chicken-and-egg: are exosomes higher because endolysosomal injury is higher, or do higher exosomes lead to higher endolysosomal injury? If EVs are to ever become a therapeutic target for NPC, determining the impact of increased exosome release – and whether it should be stimulated or inhibited – will be critical.

4.4: EVs, Cholesterol, and NPC: a Proposed Mechanism

We do not yet know the mechanism behind NPC and altered EVs, but like many aspects of NPC, it is likely influenced by cholesterol. A series of three publications in 2024 suggest a possible model. First, Palmulli *et. al.* demonstrated that CD63 is a key regulator of EV cholesterol content. The authors discovered a cholesterol binding-pocket on CD63, and found that CD63 clusters and sorts cholesterol into intraluminal vesicles (ILVs) for release as cholesterol-rich, CD63-positive exosomes[56]. Though not tested by the authors, this finding

suggests that increased endolysosomal cholesterol content could result in increased formation of CD63+ ILVs. These CD63+ ILVs could then be released from the cell as exosomes through a number of established NPC1-independent pathways, including Rab7 and Rab27a[131, 132]. A second study by Bonora *et. al.* found that modulating intracellular cholesterol release directly impacts EV release, and in particular release of CD63+ EVs. They thus proposed that CD63+ EV biogenesis occurs on a cholesterol synthesis axis, in which greater cholesterol synthesis leads to greater EV release[133]. Finally, research by Kestecher *et. al.* provided evidence using a mouse model for atherosclerosis and hypercholesterolemia, which results in elevated cholesterol in serum but depleted cholesterol in endolysosomes. The authors found significantly decreased concentrations of circulating CD63 positive EVs, further connecting endolysosomal cholesterol content with exosome release[134, 135].

Together, these discoveries suggest a model that fits well with our data: loss of NPC1 drives cholesterol accumulation inside endolysosomes; this cholesterol is then sorted into ILVs by CD63; these ILVs are then ultimately released as exosomes that are enriched in endolysosomal markers. This model explains the increase in EVs we observe in NPC samples, particularly CD63+ populations, and why it is correlated with NPC1 protein expression; and why NPC EVs are enriched in endolysosomal surface markers such as Lamp1. In further support of this model our data show that NPC EVs are enriched in miR-320a, which is a CD63-associated miRNA[44]. It seems likely that elements of this pathway are not unique to NPC, or even dependent on NPC1 loss, but are rather a result of endolysosomal cholesterol perturbations. With the context of the 2024 publications, our research also highlights the complexity of connecting cholesterol changes with EV changes: increased cellular cholesterol synthesis increases CD63+ EV release, but increased serum cholesterol decreases CD63+ EV release, and increasing

cholesterol in endolysosomes (as in NPC) causes increased EV release. Thus, our discoveries contribute to a growing appreciation for the complex relationship between endolysosomal injury, cholesterol, and exosomes, and provide new information about the fundamental cell biology behind Niemann Pick Disease Type C.

REFERENCES

1. Wassif CA, Cross JL, Iben J, Sanchez-Pulido L, Cougnoux A, Platt FM, Ory DS, Ponting CP, Bailey-Wilson JE, Biesecker LG, Porter FD. High incidence of unrecognized visceral/neurological late-onset Niemann-Pick disease, type C1, predicted by analysis of massively parallel sequencing data sets. Genet Med. 2016;18(1):41-8. Epub 2015/03/13. doi: 10.1038/gim.2015.25. PubMed PMID: 25764212; PMCID: PMC4486368.
2. Bianconi SE, Hammond DI, Farhat NY, Dang Do A, Jenkins K, Cougnoux A, Martin K, Porter FD. Evaluation of age of death in Niemann-Pick disease, type C: Utility of disease support group websites to understand natural history. Mol Genet Metab. 2019;126(4):466-9. Epub 2019/03/10. doi: 10.1016/j.ymgme.2019.02.004. PubMed PMID: 30850267; PMCID: PMC6535124.
3. Jan M, Akbar HM, Ashfaque M, Khan ML, Talha M, Haque MA. FDA approval of Miplyffa and Aqneursa: A dual breakthrough for the treatment of Neimann-Pick disease type C. Alzheimers Dement (N Y). 2025;11(1):e70029. Epub 20250224. doi: 10.1002/trc2.70029. PubMed PMID: 39995598; PMCID: PMC11848562.
4. Geberhiwot T, Moro A, Dardis A, Ramaswami U, Sirrs S, Marfa MP, Vanier MT, Walterfang M, Bolton S, Dawson C, Héron B, Stampfer M, Imrie J, Hendriksz C, Gissen P, Crushell E, Coll MJ, Nadjar Y, Klünemann H, Mengel E, Hrebicek M, Jones SA, Ory D, Bembi B, Patterson M, on behalf of the International Niemann-Pick Disease R. Consensus clinical management guidelines for Niemann-Pick disease type C. Orphanet Journal of Rare Diseases. 2018;13(1):50. doi: 10.1186/s13023-018-0785-7.
5. Berry-Kravis E. Niemann-Pick Disease, Type C: Diagnosis, Management and Disease-Targeted Therapies in Development. Semin Pediatr Neurol. 2021;37:100879. Epub 2021/04/25. doi: 10.1016/j.spen.2021.100879. PubMed PMID: 33892845.
6. Malnar M, Hecimovic S, Mattsson N, Zetterberg H. Bidirectional links between Alzheimer's disease and Niemann-Pick type C disease. Neurobiol Dis. 2014;72 Pt A:37-47. Epub 2014/06/08. doi: 10.1016/j.nbd.2014.05.033. PubMed PMID: 24907492.
7. Vanier MT. Niemann-Pick disease type C. Orphanet Journal of Rare Diseases. 2010;5(1):16. doi: 10.1186/1750-1172-5-16.
8. Carstea ED, Morris JA, Coleman KG, Loftus SK, Zhang D, Cummings C, Gu J, Rosenfeld MA, Pavan WJ, Krizman DB, Nagle J, Polymeropoulos MH, Sturley SL, Ioannou YA, Higgins ME, Comly M, Cooney A, Brown A, Kaneski CR, Blanchette-Mackie EJ, Dwyer NK, Neufeld EB, Chang TY, Liscum L, Strauss JF, 3rd, Ohno K, Zeigler M, Carmi R, Sokol J, Markie D, O'Neill RR, van Diggelen OP, Elleder M, Patterson MC, Brady RO, Vanier MT, Pentchev PG, Tagle DA. Niemann-Pick C1 disease gene: homology to mediators of cholesterol homeostasis. Science. 1997;277(5323):228-31. Epub 1997/07/11. doi: 10.1126/science.277.5323.228. PubMed PMID: 9211849.
9. Naureckiene S, Sleat DE, Lackland H, Fensom A, Vanier MT, Wattiaux R, Jadot M, Lobel P. Identification of HE1 as the Second Gene of Niemann-Pick C Disease. Science. 2000;290(5500):2298-301. doi: doi:10.1126/science.290.5500.2298.
10. Millat G, Marçais C, Rafi MA, Yamamoto T, Morris JA, Pentchev PG, Ohno K, Wenger DA, Vanier MT. Niemann-Pick C1 disease: the I1061T substitution is a frequent mutant allele in patients of Western European descent and correlates with a classic juvenile phenotype. Am J Hum Genet. 1999;65(5):1321-9. doi: 10.1086/302626. PubMed PMID: 10521297; PMCID: PMC1288284.

11. Benussi A, Alberici A, Premi E, Bertasi V, Cotelli MS, Turla M, Dardis A, Zampieri S, Marchina E, Paghera B, Gallivanone F, Castiglioni I, Padovani A, Borroni B. Phenotypic heterogeneity of Niemann-Pick disease type C in monozygotic twins. J Neurol. 2015;262(3):642-7. Epub 20141224. doi: 10.1007/s00415-014-7619-x. PubMed PMID: 25536905.
12. Las Heras M, Szenfeld B, Ballout RA, Buratti E, Zanlungo S, Dardis A, Klein AD. Understanding the phenotypic variability in Niemann-Pick disease type C (NPC): a need for precision medicine. npj Genomic Medicine. 2023;8(1):21. doi: 10.1038/s41525-023-00365-w.
13. Evans W, Patterson M, Platt F, Guldberg C, Mathieson T, Pacey J. International consensus on clinical severity scale use in evaluating Niemann-Pick disease Type C in paediatric and adult patients: results from a Delphi Study. Orphanet J Rare Dis. 2021;16(1):482. Epub 20211118. doi: 10.1186/s13023-021-02115-6. PubMed PMID: 34794481; PMCID: PMC8600786.
14. Patterson MC, Lloyd-Price L, Guldberg C, Doll H, Burbridge C, Chladek M, íDali C, Mengel E, Symonds T. Validation of the 5-domain Niemann-Pick type C Clinical Severity Scale. Orphanet Journal of Rare Diseases. 2021;16(1):79. doi: 10.1186/s13023-021-01719-2.
15. Li X, Wang J, Coutavas E, Shi H, Hao Q, Blobel G. Structure of human Niemann–Pick C1 protein. Proceedings of the National Academy of Sciences. 2016;113(29):8212-7. doi: doi:10.1073/pnas.1607795113.
16. Vanier MT, Millat G. Structure and function of the NPC2 protein. Biochim Biophys Acta. 2004;1685(1-3):14-21. doi: 10.1016/j.bbalip.2004.08.007. PubMed PMID: 15465422.
17. Trinh MN, Brown MS, Seemann J, Goldstein JL, Lu F. Lysosomal cholesterol export reconstituted from fragments of Niemann-Pick C1. eLife. 2018;7:e38564. doi: 10.7554/eLife.38564.
18. Pfeffer SR. NPC intracellular cholesterol transporter 1 (NPC1)-mediated cholesterol export from lysosomes. J Biol Chem. 2019;294(5):1706-9. doi: 10.1074/jbc.TM118.004165. PubMed PMID: 30710017; PMCID: PMC6364775.
19. Bajwa H, Azhar W. Niemann-Pick Disease. StatPearls. Treasure Island (FL): StatPearls Publishing Copyright © 2021, StatPearls Publishing LLC.; 2021.
20. Cougnoux A, Cluzeau C, Mitra S, Li R, Williams I, Burkert K, Xu X, Wassif CA, Zheng W, Porter FD. Necroptosis in Niemann-Pick disease, type C1: a potential therapeutic target. Cell Death Dis. 2016;7:e2147. Epub 2016/03/18. doi: 10.1038/cddis.2016.16. PubMed PMID: 26986514; PMCID: PMC4823930.
21. Cariati I, Masuelli L, Bei R, Tancredi V, Frank C, D'Arcangelo G. Neurodegeneration in Niemann-Pick Type C Disease: An Updated Review on Pharmacological and Non-Pharmacological Approaches to Counteract Brain and Cognitive Impairment. Int J Mol Sci. 2021;22(12). Epub 20210620. doi: 10.3390/ijms22126600. PubMed PMID: 34202978; PMCID: PMC8234817.
22. Wheeler S, Sillence DJ. Niemann-Pick type C disease: cellular pathology and pharmacotherapy. J Neurochem. 2020;153(6):674-92. Epub 2019/10/15. doi: 10.1111/jnc.14895. PubMed PMID: 31608980.
23. Newton J, Milstien S, Spiegel S. Niemann-Pick type C disease: The atypical sphingolipidosis. Adv Biol Regul. 2018;70:82-8. Epub 2018/09/13. doi: 10.1016/j.jbior.2018.08.001. PubMed PMID: 30205942; PMCID: PMC6327306.
24. Pacheco CD, Lieberman AP. The pathogenesis of Niemann-Pick type C disease: a role for autophagy? Expert Rev Mol Med. 2008;10:e26. Epub 20080910. doi: 10.1017/s146239940800080x. PubMed PMID: 18782459; PMCID: PMC2662713.

25. Torres S, Balboa E, Zanlungo S, Enrich C, Garcia-Ruiz C, Fernandez-Checa JC. Lysosomal and Mitochondrial Liaisons in Niemann-Pick Disease. Front Physiol. 2017;8:982. Epub 20171130. doi: 10.3389/fphys.2017.00982. PubMed PMID: 29249985; PMCID: PMC5714892.
26. Thery C, Witwer KW, Aikawa E, Alcaraz MJ, Anderson JD, Andriantsitohaina R, Antoniou A, Arab T, Archer F, Atkin-Smith GK, Ayre DC, Bach JM, Bachurski D, Baharvand H, Balaj L, Baldacchino S, Bauer NN, Baxter AA, Bebawy M, Beckham C, Bedina Zavec A, Benmoussa A, Berardi AC, Bergese P, Bielska E, Blenkiron C, Bobis-Wozowicz S, Boilard E, Boireau W, Bongiovanni A, Borras FE, Bosch S, Boulanger CM, Breakefield X, Breglio AM, Brennan MA, Brigstock DR, Brisson A, Broekman ML, Bromberg JF, Bryl-Gorecka P, Buch S, Buck AH, Burger D, Busatto S, Buschmann D, Bussolati B, Buzas EI, Byrd JB, Camussi G, Carter DR, Caruso S, Chamley LW, Chang YT, Chen C, Chen S, Cheng L, Chin AR, Clayton A, Clerici SP, Cocks A, Cocucci E, Coffey RJ, Cordeiro-da-Silva A, Couch Y, Coumans FA, Coyle B, Crescitelli R, Criado MF, D'Souza-Schorey C, Das S, Datta Chaudhuri A, de Candia P, De Santana EF, De Wever O, Del Portillo HA, Demaret T, Deville S, Devitt A, Dhondt B, Di Vizio D, Dieterich LC, Dolo V, Dominguez Rubio AP, Dominici M, Dourado MR, Driedonks TA, Duarte FV, Duncan HM, Eichenberger RM, Ekstrom K, El Andaloussi S, Elie-Caille C, Erdbrugger U, Falcon-Perez JM, Fatima F, Fish JE, Flores-Bellver M, Forsonits A, Frelet-Barrand A, Fricke F, Fuhrmann G, Gabrielsson S, Gamez-Valero A, Gardiner C, Gartner K, Gaudin R, Gho YS, Giebel B, Gilbert C, Gimona M, Giusti I, Goberdhan DC, Gorgens A, Gorski SM, Greening DW, Gross JC, Gualerzi A, Gupta GN, Gustafson D, Handberg A, Haraszti RA, Harrison P, Hegyesi H, Hendrix A, Hill AF, Hochberg FH, Hoffmann KF, Holder B, Holthofer H, Hosseinkhani B, Hu G, Huang Y, Huber V, Hunt S, Ibrahim AG, Ikezu T, Inal JM, Isin M, Ivanova A, Jackson HK, Jacobsen S, Jay SM, Jayachandran M, Jenster G, Jiang L, Johnson SM, Jones JC, Jong A, Jovanovic-Talisman T, Jung S, Kalluri R, Kano SI, Kaur S, Kawamura Y, Keller ET, Khamari D, Khomyakova E, Khvorova A, Kierulf P, Kim KP, Kislinger T, Klingeborn M, Klinke DJ, 2nd, Kornek M, Kosanovic MM, Kovacs AF, Kramer-Albers EM, Krasemann S, Krause M, Kurochkin IV, Kusuma GD, Kuypers S, Laitinen S, Langevin SM, Languino LR, Lannigan J, Lasser C, Laurent LC, Lavieu G, Lazaro-Ibanez E, Le Lay S, Lee MS, Lee YXF, Lemos DS, Lenassi M, Leszczynska A, Li IT, Liao K, Libregts SF, Ligeti E, Lim R, Lim SK, Line A, Linnemannstons K, Llorente A, Lombard CA, Lorenowicz MJ, Lorincz AM, Lotvall J, Lovett J, Lowry MC, Loyer X, Lu Q, Lukomska B, Lunavat TR, Maas SL, Malhi H, Marcilla A, Mariani J, Mariscal J, Martens-Uzunova ES, Martin-Jaular L, Martinez MC, Martins VR, Mathieu M, Mathivanan S, Maugeri M, McGinnis LK, McVey MJ, Meckes DG, Jr., Meehan KL, Mertens I, Minciacchi VR, Moller A, Moller Jorgensen M, Morales-Kastresana A, Morhayim J, Mullier F, Muraca M, Musante L, Mussack V, Muth DC, Myburgh KH, Najrana T, Nawaz M, Nazarenko I, Nejsum P, Neri C, Neri T, Nieuwland R, Nimrichter L, Nolan JP, Nolte-'t Hoen EN, Noren Hooten N, O'Driscoll L, O'Grady T, O'Loghlen A, Ochiya T, Olivier M, Ortiz A, Ortiz LA, Osteikoetxea X, Ostergaard O, Ostrowski M, Park J, Pegtel DM, Peinado H, Perut F, Pfaffl MW, Phinney DG, Pieters BC, Pink RC, Pisetsky DS, Pogge von Strandmann E, Polakovicova I, Poon IK, Powell BH, Prada I, Pulliam L, Quesenberry P, Radeghieri A, Raffai RL, Raimondo S, Rak J, Ramirez MI, Raposo G, Rayyan MS, Regev-Rudzki N, Ricklefs FL, Robbins PD, Roberts DD, Rodrigues SC, Rohde E, Rome S, Rouschop KM, Rughetti A, Russell AE, Saa P, Sahoo S, Salas-Huenuleo E, Sanchez C, Saugstad JA, Saul MJ, Schiffelers RM, Schneider R, Schoyen TH, Scott A, Shahaj E, Sharma S, Shatnyeva O, Shekari F, Shelke GV, Shetty AK, Shiba K, Siljander PR, Silva AM, Skowronek A, Snyder OL, 2nd, Soares RP, Sodar BW, Soekmadji C, Sotillo J, Stahl

PD, Stoorvogel W, Stott SL, Strasser EF, Swift S, Tahara H, Tewari M, Timms K, Tiwari S, Tixeira R, Tkach M, Toh WS, Tomasini R, Torrecilhas AC, Tosar JP, Toxavidis V, Urbanelli L, Vader P, van Balkom BW, van der Grein SG, Van Deun J, van Herwijnen MJ, Van Keuren-Jensen K, van Niel G, van Royen ME, van Wijnen AJ, Vasconcelos MH, Vechetti IJ, Jr., Veit TD, Vella LJ, Velot E, Verweij FJ, Vestad B, Vinas JL, Visnovitz T, Vukman KV, Wahlgren J, Watson DC, Wauben MH, Weaver A, Webber JP, Weber V, Wehman AM, Weiss DJ, Welsh JA, Wendt S, Wheelock AM, Wiener Z, Witte L, Wolfram J, Xagorari A, Xander P, Xu J, Yan X, Yanez-Mo M, Yin H, Yuana Y, Zappulli V, Zarubova J, Zekas V, Zhang JY, Zhao Z, Zheng L, Zheutlin AR, Zickler AM, Zimmermann P, Zivkovic AM, Zocco D, Zuba-Surma EK. Minimal information for studies of extracellular vesicles 2018 (MISEV2018): a position statement of the International Society for Extracellular Vesicles and update of the MISEV2014 guidelines. J Extracell Vesicles. 2018;7(1):1535750. Epub 2019/01/15. doi: 10.1080/20013078.2018.1535750. PubMed PMID: 30637094; PMCID: PMC6322352.

27. Sardar Sinha M, Ansell-Schultz A, Civitelli L, Hildesjo C, Larsson M, Lannfelt L, Ingelsson M, Hallbeck M. Alzheimer's disease pathology propagation by exosomes containing toxic amyloid-beta oligomers. Acta Neuropathol. 2018;136(1):41-56. Epub 2018/06/24. doi: 10.1007/s00401-018-1868-1. PubMed PMID: 29934873; PMCID: PMC6015111.

28. Van Hoecke L, Van Cauwenberghe C, Börger V, Bruggeman A, Castelein J, Van Imschoot G, Van Wonterghem E, Dittrich R, Claeys W, Xie J, Giebel B, Vandenbroucke RE. Anti-Inflammatory Mesenchymal Stromal Cell-Derived Extracellular Vesicles Improve Pathology in Niemann-Pick Type C Disease. Biomedicines. 2021;9(12). Epub 20211208. doi: 10.3390/biomedicines9121864. PubMed PMID: 34944681; PMCID: PMC8698931.

29. Upadhya R, Zingg W, Shetty S, Shetty AK. Astrocyte-derived extracellular vesicles: Neuroreparative properties and role in the pathogenesis of neurodegenerative disorders. J Control Release. 2020;323:225-39. Epub 20200411. doi: 10.1016/j.jconrel.2020.04.017. PubMed PMID: 32289328; PMCID: PMC7299747.

30. Richards KE, Zeleniak AE, Fishel ML, Wu J, Littlepage LE, Hill R. Cancer-associated fibroblast exosomes regulate survival and proliferation of pancreatic cancer cells. Oncogene. 2017;36(13):1770-8. Epub 2016/09/27. doi: 10.1038/onc.2016.353. PubMed PMID: 27669441; PMCID: PMC5366272.

31. Zhou E, Li Y, Wu F, Guo M, Xu J, Wang S, Tan Q, Ma P, Song S, Jin Y. Circulating extracellular vesicles are effective biomarkers for predicting response to cancer therapy. EBioMedicine. 2021;67:103365. Epub 20210507. doi: 10.1016/j.ebiom.2021.103365. PubMed PMID: 33971402; PMCID: PMC8121992.

32. Rastogi S, Sharma V, Bharti PS, Rani K, Modi GP, Nikolajeff F, Kumar S. The Evolving Landscape of Exosomes in Neurodegenerative Diseases: Exosomes Characteristics and a Promising Role in Early Diagnosis. Int J Mol Sci. 2021;22(1). Epub 2021/01/08. doi: 10.3390/ijms22010440. PubMed PMID: 33406804; PMCID: PMC7795439.

33. Soliman HM, Ghonaim GA, Gharib SM, Chopra H, Farag AK, Hassanin MH, Nagah A, Emad-Eldin M, Hashem NE, Yahya G, Emam SE, Hassan AEA, Attia MS. Exosomes in Alzheimer’s Disease: From Being Pathological Players to Potential Diagnostics and Therapeutics. International Journal of Molecular Sciences. 2021;22(19):10794. PubMed PMID: doi:10.3390/ijms221910794.

34. Picca A, Guerra F, Calvani R, Coelho-Junior HJ, Landi F, Bernabei R, Romano R, Bucci C, Marzetti E. Extracellular Vesicles and Damage-Associated Molecular Patterns: A Pandora's

Box in Health and Disease. Front Immunol. 2020;11:601740. Epub 2020/12/12. doi: 10.3389/fimmu.2020.601740. PubMed PMID: 33304353; PMCID: PMC7701251.
35. Costafreda MI, Abbasi A, Lu H, Kaplan G. Exosome mimicry by a HAVCR1-NPC1 pathway of endosomal fusion mediates hepatitis A virus infection. Nat Microbiol. 2020;5(9):1096-106. Epub 20200615. doi: 10.1038/s41564-020-0740-y. PubMed PMID: 32541946; PMCID: PMC7483988.
36. Tatiana S, Stanislav N, Darya K, Luiza G, Konstantin S, Sergey L, Elena V, Galina S, Nikolai V, Arthur K, Elena Z, Roman K, Tatiana U, Alexander S, Ekaterina Z, Anton E, Sofya P. Altered level of plasma exosomes in patients with Gaucher disease. Eur J Med Genet. 2020;63(11):104038. Epub 20200818. doi: 10.1016/j.ejmg.2020.104038. PubMed PMID: 32822875.
37. Gleason AM, Woo EG, McKinney C, Sidransky E. The Role of Exosomes in Lysosomal Storage Disorders. Biomolecules. 2021;11(4). Epub 2021/05/01. doi: 10.3390/biom11040576. PubMed PMID: 33920837; PMCID: PMC8071119.
38. Welsh JA, Goberdhan DCI, O'Driscoll L, Buzas EI, Blenkiron C, Bussolati B, Cai H, Di Vizio D, Driedonks TAP, Erdbrügger U, Falcon-Perez JM, Fu QL, Hill AF, Lenassi M, Lim SK, Mahoney MG, Mohanty S, Möller A, Nieuwland R, Ochiya T, Sahoo S, Torrecilhas AC, Zheng L, Zijlstra A, Abuelreich S, Bagabas R, Bergese P, Bridges EM, Brucale M, Burger D, Carney RP, Cocucci E, Crescitelli R, Hanser E, Harris AL, Haughey NJ, Hendrix A, Ivanov AR, Jovanovic-Talisman T, Kruh-Garcia NA, Ku'ulei-Lyn Faustino V, Kyburz D, Lässer C, Lennon KM, Lötvall J, Maddox AL, Martens-Uzunova ES, Mizenko RR, Newman LA, Ridolfi A, Rohde E, Rojalin T, Rowland A, Saftics A, Sandau US, Saugstad JA, Shekari F, Swift S, Ter-Ovanesyan D, Tosar JP, Useckaite Z, Valle F, Varga Z, van der Pol E, van Herwijnen MJC, Wauben MHM, Wehman AM, Williams S, Zendrini A, Zimmerman AJ, Théry C, Witwer KW. Minimal information for studies of extracellular vesicles (MISEV2023): From basic to advanced approaches. J Extracell Vesicles. 2024;13(2):e12404. doi: 10.1002/jev2.12404. PubMed PMID: 38326288; PMCID: PMC10850029.
39. Jeppesen DK, Fenix AM, Franklin JL, Higginbotham JN, Zhang Q, Zimmerman LJ, Liebler DC, Ping J, Liu Q, Evans R, Fissell WH, Patton JG, Rome LH, Burnette DT, Coffey RJ. Reassessment of Exosome Composition. Cell. 2019;177(2):428-45 e18. Epub 2019/04/06. doi: 10.1016/j.cell.2019.02.029. PubMed PMID: 30951670; PMCID: PMC6664447.
40. Doyle LM, Wang MZ. Overview of Extracellular Vesicles, Their Origin, Composition, Purpose, and Methods for Exosome Isolation and Analysis. Cells. 2019;8(7). Epub 2019/07/18. doi: 10.3390/cells8070727. PubMed PMID: 31311206; PMCID: PMC6678302.
41. Konoshenko MY, Lekchnov EA, Vlassov AV, Laktionov PP. Isolation of Extracellular Vesicles: General Methodologies and Latest Trends. BioMed Research International. 2018;2018:8545347. doi: 10.1155/2018/8545347.
42. Couch Y, Buzàs EI, Di Vizio D, Gho YS, Harrison P, Hill AF, Lötvall J, Raposo G, Stahl PD, Théry C, Witwer KW, Carter DRF. A brief history of nearly EV-erything - The rise and rise of extracellular vesicles. J Extracell Vesicles. 2021;10(14):e12144. doi: 10.1002/jev2.12144. PubMed PMID: 34919343; PMCID: PMC8681215.
43. Valadi H, Ekström K, Bossios A, Sjöstrand M, Lee JJ, Lötvall JO. Exosome-mediated transfer of mRNAs and microRNAs is a novel mechanism of genetic exchange between cells. Nat Cell Biol. 2007;9(6):654-9. Epub 20070507. doi: 10.1038/ncb1596. PubMed PMID: 17486113.

44. Kaur S, Elkahloun AG, Arakelyan A, Young L, Myers TG, Otaizo-Carrasquero F, Wu W, Margolis L, Roberts DD. CD63, MHC class 1, and CD47 identify subsets of extracellular vesicles containing distinct populations of noncoding RNAs. Scientific Reports. 2018;8(1):2577. doi: 10.1038/s41598-018-20936-7.
45. Lai EC. Micro RNAs are complementary to 3' UTR sequence motifs that mediate negative post-transcriptional regulation. Nat Genet. 2002;30(4):363-4. Epub 20020318. doi: 10.1038/ng865. PubMed PMID: 11896390.
46. Filipowicz W, Bhattacharyya SN, Sonenberg N. Mechanisms of post-transcriptional regulation by microRNAs: are the answers in sight? Nat Rev Genet. 2008;9(2):102-14. doi: 10.1038/nrg2290. PubMed PMID: 18197166.
47. Wiedrick JT, Phillips JI, Lusardi TA, McFarland TJ, Lind B, Sandau US, Harrington CA, Lapidus JA, Galasko DR, Quinn JF, Saugstad JA. Validation of MicroRNA Biomarkers for Alzheimer's Disease in Human Cerebrospinal Fluid. J Alzheimers Dis. 2019;67(3):875-91. doi: 10.3233/jad-180539. PubMed PMID: 30689565; PMCID: PMC6687305.
48. Sandau US, Wiedrick JT, Smith SJ, McFarland TJ, Lusardi TA, Lind B, Harrington CA, Lapidus JA, Galasko DR, Quinn JF, Saugstad JA. Performance of Validated MicroRNA Biomarkers for Alzheimer's Disease in Mild Cognitive Impairment. J Alzheimers Dis. 2020;78(1):245-63. Epub 2020/09/22. doi: 10.3233/JAD-200396. PubMed PMID: 32955460.
49. Skotland T, Hessvik NP, Sandvig K, Llorente A. Exosomal lipid composition and the role of ether lipids and phosphoinositides in exosome biology. J Lipid Res. 2019;60(1):9-18. Epub 2018/08/05. doi: 10.1194/jlr.R084343. PubMed PMID: 30076207; PMCID: PMC6314266.
50. Su H, Rustam YH, Masters CL, Makalic E, McLean CA, Hill AF, Barnham KJ, Reid GE, Vella LJ. Characterization of brain-derived extracellular vesicle lipids in Alzheimer's disease. J Extracell Vesicles. 2021;10(7):e12089. Epub 2021/05/21. doi: 10.1002/jev2.12089. PubMed PMID: 34012516; PMCID: PMC8111496.
51. Soto-Huelin B, Babiy B, Pastor O, Díaz-García M, Toledano-Zaragoza A, Frutos MD, Espín JC, Tomás-Barberán FA, Busto R, Ledesma MD. Ellagic acid and its metabolites urolithins A/B ameliorate most common disease phenotypes in cellular and mouse models for lysosomal storage disorders by enhancing extracellular vesicle secretion. Neurobiol Dis. 2023;182:106141. Epub 20230428. doi: 10.1016/j.nbd.2023.106141. PubMed PMID: 37121555.
52. Gurung S, Perocheau D, Touramanidou L, Baruteau J. The exosome journey: from biogenesis to uptake and intracellular signalling. Cell Commun Signal. 2021;19(1):47. Epub 2021/04/25. doi: 10.1186/s12964-021-00730-1. PubMed PMID: 33892745; PMCID: PMC8063428.
53. Zhang Y, Liu Y, Liu H, Tang WH. Exosomes: biogenesis, biologic function and clinical potential. Cell Biosci. 2019;9:19. Epub 2019/03/01. doi: 10.1186/s13578-019-0282-2. PubMed PMID: 30815248; PMCID: PMC6377728.
54. Trajkovic K, Hsu C, Chiantia S, Rajendran L, Wenzel D, Wieland F, Schwille P, Brügger B, Simons M. Ceramide Triggers Budding of Exosome Vesicles into Multivesicular Endosomes. Science. 2008;319(5867):1244-7. doi: 10.1126/science.1153124.
55. Dinkins MB, Enasko J, Hernandez C, Wang G, Kong J, Helwa I, Liu Y, Terry AV, Jr., Bieberich E. Neutral Sphingomyelinase-2 Deficiency Ameliorates Alzheimer's Disease Pathology and Improves Cognition in the 5XFAD Mouse. J Neurosci. 2016;36(33):8653-67. Epub 2016/08/19. doi: 10.1523/JNEUROSCI.1429-16.2016. PubMed PMID: 27535912; PMCID: PMC4987436.

56. Palmulli R, Couty M, Piontek MC, Ponnaiah M, Dingli F, Verweij FJ, Charrin S, Tantucci M, Sasidharan S, Rubinstein E, Kontush A, Loew D, Lhomme M, Roos WH, Raposo G, van Niel G. CD63 sorts cholesterol into endosomes for storage and distribution via exosomes. Nat Cell Biol. 2024;26(7):1093-109. Epub 20240617. doi: 10.1038/s41556-024-01432-9. PubMed PMID: 38886558.
57. Peruzzi JA, Gunnels TF, Edelstein HI, Lu P, Baker D, Leonard JN, Kamat NP. Enhancing extracellular vesicle cargo loading and functional delivery by engineering protein-lipid interactions. Nature Communications. 2024;15(1):5618. doi: 10.1038/s41467-024-49678-z.
58. Phuyal S, Hessvik NP, Skotland T, Sandvig K, Llorente A. Regulation of exosome release by glycosphingolipids and flotillins. FEBS J. 2014;281(9):2214-27. Epub 2014/03/13. doi: 10.1111/febs.12775. PubMed PMID: 24605801.
59. Kalra H, Drummen GPC, Mathivanan S. Focus on Extracellular Vesicles: Introducing the Next Small Big Thing. International Journal of Molecular Sciences. 2016;17(2):170. PubMed PMID: doi:10.3390/ijms17020170.
60. Yu J, Sane S, Kim J-E, Yun S, Kim H-J, Jo KB, Wright JP, Khoshdoozmasouleh N, Lee K, Oh HT, Thiel K, Parvin A, Williams X, Hannon C, Lee H, Kim D-K. Biogenesis and delivery of extracellular vesicles: harnessing the power of EVs for diagnostics and therapeutics. Frontiers in Molecular Biosciences. 2024;Volume 10 - 2023. doi: 10.3389/fmolb.2023.1330400.
61. Kim HI, Park J, Zhu Y, Wang X, Han Y, Zhang D. Recent advances in extracellular vesicles for therapeutic cargo delivery. Experimental & Molecular Medicine. 2024;56(4):836-49. doi: 10.1038/s12276-024-01201-6.
62. Dellar ER, Hill C, Melling GE, Carter DRF, Baena-Lopez LA. Unpacking extracellular vesicles: RNA cargo loading and function. J Extracell Biol. 2022;1(5):e40. Epub 20220502. doi: 10.1002/jex2.40. PubMed PMID: 38939528; PMCID: PMC11080855.
63. Nolan JP, Duggan E. Analysis of Individual Extracellular Vesicles by Flow Cytometry. Methods Mol Biol. 2018;1678:79-92. Epub 2017/10/27. doi: 10.1007/978-1-4939-7346-0_5. PubMed PMID: 29071676.
64. Sandau US, Magaña SM, Costa J, Nolan JP, Ikezu T, Vella LJ, Jackson HK, Moreira LR, Palacio PL, Hill AF, Quinn JF, Van Keuren-Jensen KR, McFarland TJ, Palade J, Sribnick EA, Su H, Vekrellis K, Coyle B, Yang Y, Falcón-Perez JM, Nieuwland R, Saugstad JA, Force ISfEVCFT. Recommendations for reproducibility of cerebrospinal fluid extracellular vesicle studies. Journal of Extracellular Vesicles. 2024;13(1):12397. doi: https://doi.org/10.1002/jev2.12397.
65. Zeng Y, Qiu Y, Jiang W, Shen J, Yao X, He X, Li L, Fu B, Liu X. Biological Features of Extracellular Vesicles and Challenges. Front Cell Dev Biol. 2022;10:816698. Epub 20220624. doi: 10.3389/fcell.2022.816698. PubMed PMID: 35813192; PMCID: PMC9263222.
66. Welsh JA, Van Der Pol E, Arkesteijn GJA, Bremer M, Brisson A, Coumans F, Dignat-George F, Duggan E, Ghiran I, Giebel B, Gorgens A, Hendrix A, Lacroix R, Lannigan J, Libregts S, Lozano-Andres E, Morales-Kastresana A, Robert S, De Rond L, Tertel T, Tigges J, De Wever O, Yan X, Nieuwland R, Wauben MHM, Nolan JP, Jones JC. MIFlowCyt-EV: a framework for standardized reporting of extracellular vesicle flow cytometry experiments. J Extracell Vesicles. 2020;9(1):1713526. Epub 2020/03/05. doi: 10.1080/20013078.2020.1713526. PubMed PMID: 32128070; PMCID: PMC7034442.
67. Eitan E, Suire C, Zhang S, Mattson MP. Impact of lysosome status on extracellular vesicle content and release. Ageing Res Rev. 2016;32:65-74. Epub 2016/05/31. doi: 10.1016/j.arr.2016.05.001. PubMed PMID: 27238186; PMCID: PMC5154730.

68. Lu F, Liang Q, Abi-Mosleh L, Das A, De Brabander JK, Goldstein JL, Brown MS. Identification of NPC1 as the target of U18666A, an inhibitor of lysosomal cholesterol export and Ebola infection. Elife. 2015;4. Epub 20151208. doi: 10.7554/eLife.12177. PubMed PMID: 26646182; PMCID: PMC4718804.
69. Elgner F, Ren H, Medvedev R, Ploen D, Himmelsbach K, Boller K, Hildt E. The Intracellular Cholesterol Transport Inhibitor U18666A Inhibits the Exosome-Dependent Release of Mature Hepatitis C Virus. J Virol. 2016;90(24):11181-96. Epub 20161128. doi: 10.1128/jvi.01053-16. PubMed PMID: 27707921; PMCID: PMC5126375.
70. Juhl AD, Lund FW, Jensen MLV, Szomek M, Heegaard CW, Guttmann P, Werner S, McNally J, Schneider G, Kapishnikov S, Wüstner D. Niemann Pick C2 protein enables cholesterol transfer from endo-lysosomes to the plasma membrane for efflux by shedding of extracellular vesicles. Chem Phys Lipids. 2021;235:105047. Epub 20210107. doi: 10.1016/j.chemphyslip.2020.105047. PubMed PMID: 33422548.
71. Wüstner D, Dupont Juhl A, Egebjerg JM, Werner S, McNally J, Schneider G. Kinetic modelling of sterol transport between plasma membrane and endo-lysosomes based on quantitative fluorescence and X-ray imaging data. Front Cell Dev Biol. 2023;11:1144936. Epub 20231031. doi: 10.3389/fcell.2023.1144936. PubMed PMID: 38020900; PMCID: PMC10644255.
72. Strauss K, Goebel C, Runz H, Mobius W, Weiss S, Feussner I, Simons M, Schneider A. Exosome secretion ameliorates lysosomal storage of cholesterol in Niemann-Pick type C disease. J Biol Chem. 2010;285(34):26279-88. Epub 2010/06/18. doi: 10.1074/jbc.M110.134775. PubMed PMID: 20554533; PMCID: PMC2924046.
73. Albacete-Albacete L, Navarro-Lérida I, López JA, Martín-Padura I, Astudillo AM, Ferrarini A, Van-Der-Heyden M, Balsinde J, Orend G, Vázquez J, Del Pozo M. ECM deposition is driven by caveolin-1-dependent regulation of exosomal biogenesis and cargo sorting. J Cell Biol. 2020;219(11). doi: 10.1083/jcb.202006178. PubMed PMID: 33053168; PMCID: PMC7551399.
74. Guix FX, Capitán AM, Casadomé-Perales Á, Palomares-Pérez I, López Del Castillo I, Miguel V, Goedeke L, Martín MG, Lamas S, Peinado H, Fernández-Hernando C, Dotti CG. Increased exosome secretion in neurons aging in vitro by NPC1-mediated endosomal cholesterol buildup. Life Sci Alliance. 2021;4(8). Epub 20210628. doi: 10.26508/lsa.202101055. PubMed PMID: 34183444; PMCID: PMC8321659.
75. Wu Q, Cortez L, Kamali-Jamil R, Sim V, Wille H, Kar S. Implications of exosomes derived from cholesterol-accumulated astrocytes in Alzheimer's disease pathology. Dis Model Mech. 2021;14(10). Epub 20211026. doi: 10.1242/dmm.048929. PubMed PMID: 34524402; PMCID: PMC8560497.
76. Van Hoecke L, Van Cauwenberghe C, Dominko K, Van Imschoot G, Van Wonterghem E, Castelein J, Xie J, Claeys W, Vandendriessche C, Kremer A, Borghgraef P, De Rycke R, Hecimovic S, Vandenbroucke RE. Involvement of the Choroid Plexus in the Pathogenesis of Niemann-Pick Disease Type C. Front Cell Neurosci. 2021;15:757482. Epub 20211015. doi: 10.3389/fncel.2021.757482. PubMed PMID: 34720883; PMCID: PMC8555471.
77. Cashikar AG, Hanson PI. A cell-based assay for CD63-containing extracellular vesicles. PLoS One. 2019;14(7):e0220007. Epub 20190724. doi: 10.1371/journal.pone.0220007. PubMed PMID: 31339911; PMCID: PMC6655660.
78. Canfrán-Duque A, Pastor O, Quintana-Portillo R, Lerma M, de la Peña G, Martín-Hidalgo A, Fernández-Hernando C, Lasunción MA, Busto R. Curcumin promotes

exosomes/microvesicles secretion that attenuates lysosomal cholesterol traffic impairment. Mol Nutr Food Res. 2014;58(4):687-97. Epub 20131129. doi: 10.1002/mnfr.201300350. PubMed PMID: 24288129.
79. Ilnytska O, Jeziorek M, Lai K, Altan-Bonnet N, Dobrowolski R, Storch J. Lysobisphosphatidic acid (LBPA) enrichment promotes cholesterol egress via exosomes in Niemann Pick type C1 deficient cells. Biochim Biophys Acta Mol Cell Biol Lipids. 2021;1866(6):158916. Epub 20210312. doi: 10.1016/j.bbalip.2021.158916. PubMed PMID: 33716137; PMCID: PMC8038758.
80. Feltes M, Gale SE, Moores S, Ory DS, Schaffer JE. Monitoring the itinerary of lysosomal cholesterol in Niemann-Pick Type C1-deficient cells after cyclodextrin treatment. J Lipid Res. 2020;61(3):403-12. Epub 2020/01/29. doi: 10.1194/jlr.RA119000571. PubMed PMID: 31988149; PMCID: PMC7053843.
81. Lu A, Hsieh F, Sharma BR, Vaughn SR, Enrich C, Pfeffer SR. CRISPR screens for lipid regulators reveal a role for ER-bound SNX13 in lysosomal cholesterol export. J Cell Biol. 2022;221(2). Epub 20211222. doi: 10.1083/jcb.202105060. PubMed PMID: 34936700; PMCID: PMC8704955.
82. Du X, Kazim AS, Brown AJ, Yang H. An essential role of Hrs/Vps27 in endosomal cholesterol trafficking. Cell Rep. 2012;1(1):29-35. Epub 20120126. doi: 10.1016/j.celrep.2011.10.004. PubMed PMID: 22832105.
83. Mishra S, Kell P, Scherrer D, Dietzen DJ, Vite CH, Berry-Kravis E, Davidson C, Cologna SM, Porter FD, Ory DS, Jiang X. Accumulation of alkyl-lysophosphatidylcholines in Niemann-Pick disease type C1. J Lipid Res. 2024;65(8):100600. Epub 20240722. doi: 10.1016/j.jlr.2024.100600. PubMed PMID: 39048052; PMCID: PMC11367646.
84. Vella LJ, Hill AF, Cheng L. Focus on Extracellular Vesicles: Exosomes and Their Role in Protein Trafficking and Biomarker Potential in Alzheimer's and Parkinson's Disease. International journal of molecular sciences. 2016;17(2):173-. doi: 10.3390/ijms17020173. PubMed PMID: 26861304.
85. Tancini B, Buratta S, Sagini K, Costanzi E, Delo F, Urbanelli L, Emiliani C. Insight into the Role of Extracellular Vesicles in Lysosomal Storage Disorders. Genes. 2019;10(7):510. PubMed PMID: doi:10.3390/genes10070510.
86. Gurunathan S, Kang MH, Kim JH. A Comprehensive Review on Factors Influences Biogenesis, Functions, Therapeutic and Clinical Implications of Exosomes. Int J Nanomedicine. 2021;16:1281-312. Epub 2021/02/26. doi: 10.2147/IJN.S291956. PubMed PMID: 33628021; PMCID: PMC7898217.
87. Ozsait B, Komurcu-Bayrak E, Levula M, Erginel-Unaltuna N, Kähönen M, Rai M, Lehtimäki T, Laaksonen R. Niemann-Pick type C fibroblasts have a distinct microRNA profile related to lipid metabolism and certain cellular components. Biochem Biophys Res Commun. 2010;403(3-4):316-21. Epub 20101112. doi: 10.1016/j.bbrc.2010.11.026. PubMed PMID: 21075073.
88. Pergande MR, Cougnoux A, Rathnayake RAC, Porter FD, Cologna SM. Differential Proteomics Reveals miR-155 as a Novel Indicator of Liver and Spleen Pathology in the Symptomatic Niemann-Pick Disease, Type C1 Mouse Model. Molecules. 2019;24(5). Epub 20190312. doi: 10.3390/molecules24050994. PubMed PMID: 30870990; PMCID: PMC6429457.

89. Qian H, Wu X, Du X, Yao X, Zhao X, Lee J, Yang H, Yan N. Structural Basis of Low-pH-Dependent Lysosomal Cholesterol Egress by NPC1 and NPC2. Cell. 2020;182(1):98-111.e18. doi: https://doi.org/10.1016/j.cell.2020.05.020.
90. Sun X, Marks DL, Park WD, Wheatley CL, Puri V, O'Brien JF, Kraft DL, Lundquist PA, Patterson MC, Pagano RE, Snow K. Niemann-Pick C variant detection by altered sphingolipid trafficking and correlation with mutations within a specific domain of NPC1. Am J Hum Genet. 2001;68(6):1361-72. Epub 20010509. doi: 10.1086/320599. PubMed PMID: 11349231; PMCID: PMC1226123.
91. Millat G, Marçais C, Tomasetto C, Chikh K, Fensom AH, Harzer K, Wenger DA, Ohno K, Vanier MT. Niemann-Pick C1 Disease: Correlations between NPC1 Mutations, Levels of NPC1 Protein, and Phenotypes Emphasize the Functional Significance of the Putative Sterol-Sensing Domain and of the Cysteine-Rich Luminal Loop. The American Journal of Human Genetics. 2001;68(6):1373-85. doi: https://doi.org/10.1086/320606.
92. Sandau US, McFarland TJ, Smith SJ, Galasko DR, Quinn JF, Saugstad JA. Differential Effects of APOE Genotype on MicroRNA Cargo of Cerebrospinal Fluid Extracellular Vesicles in Females With Alzheimer's Disease Compared to Males. Front Cell Dev Biol. 2022;10:864022. Epub 20220427. doi: 10.3389/fcell.2022.864022. PubMed PMID: 35573689; PMCID: PMC9092217.
93. Mathieu M, Névo N, Jouve M, Valenzuela JI, Maurin M, Verweij FJ, Palmulli R, Lankar D, Dingli F, Loew D, Rubinstein E, Boncompain G, Perez F, Théry C. Specificities of exosome versus small ectosome secretion revealed by live intracellular tracking of CD63 and CD9. Nature Communications. 2021;12(1):4389. doi: 10.1038/s41467-021-24384-2.
94. Rubinstein E, Théry C, Zimmermann P. Tetraspanins affect membrane structures and the trafficking of molecular partners: what impact on extracellular vesicles? Biochemical Society Transactions. 2025;53(02):371-82. doi: 10.1042/bst20240523.
95. Cawley NX, Sojka C, Cougnoux A, Lyons AT, Nicoli ER, Wassif CA, Porter FD. Abnormal LAMP1 glycosylation may play a role in Niemann-Pick disease, type C pathology. PLoS One. 2020;15(1):e0227829. Epub 20200130. doi: 10.1371/journal.pone.0227829. PubMed PMID: 31999726; PMCID: PMC6992233.
96. Huang HY, Lin YC, Cui S, Huang Y, Tang Y, Xu J, Bao J, Li Y, Wen J, Zuo H, Wang W, Li J, Ni J, Ruan Y, Li L, Chen Y, Xie Y, Zhu Z, Cai X, Chen X, Yao L, Chen Y, Luo Y, LuXu S, Luo M, Chiu CM, Ma K, Zhu L, Cheng GJ, Bai C, Chiang YC, Wang L, Wei F, Lee TY, Huang HD. miRTarBase update 2022: an informative resource for experimentally validated miRNA-target interactions. Nucleic Acids Res. 2022;50(D1):D222-d30. doi: 10.1093/nar/gkab1079. PubMed PMID: 34850920; PMCID: PMC8728135.
97. Agarwal V, Bell GW, Nam J-W, Bartel DP. Predicting effective microRNA target sites in mammalian mRNAs. eLife. 2015;4:e05005. doi: 10.7554/eLife.05005.
98. Chen Y, Wang X. miRDB: an online database for prediction of functional microRNA targets. Nucleic Acids Res. 2020;48(D1):D127-d31. doi: 10.1093/nar/gkz757. PubMed PMID: 31504780; PMCID: PMC6943051.
99. Chen FW, Li C, Ioannou YA. Cyclodextrin induces calcium-dependent lysosomal exocytosis. PloS one. 2010;5(11):e15054-e. doi: 10.1371/journal.pone.0015054. PubMed PMID: 21124786.
100. Singhal A, Krystofiak ES, Jerome WG, Song B. 2-Hydroxypropyl-gamma-cyclodextrin overcomes NPC1 deficiency by enhancing lysosome-ER association and autophagy. Scientific Reports. 2020;10(1):8663. doi: 10.1038/s41598-020-65627-4.

101. Lu X, Yang B, Yang H, Wang L, Li H, Chen S, Lu X, Gu D. MicroRNA-320b Modulates Cholesterol Efflux and Atherosclerosis. Journal of Atherosclerosis and Thrombosis. 2022;29(2):200-20. doi: 10.5551/jat.57125.
102. Aranda JF, Pérez-García A, Torrecilla-Parra M, Fernández-de Frutos M, Martín-Martín Y, Mateos-Gómez PA, Pardo-Marqués V, Busto R, Ramírez CM. Role of miR-199a-5p in the post-transcriptional regulation of ABCA1 in response to hypoxia in peritoneal macrophages. Front Cardiovasc Med. 2022;9:994080. Epub 20221103. doi: 10.3389/fcvm.2022.994080. PubMed PMID: 36407436; PMCID: PMC9669644.
103. Gui J, Tian Y, Wen X, Zhang W, Zhang P, Gao J, Run W, Tian L, Jia X, Gao Y. Serum microRNA characterization identifies miR-885-5p as a potential marker for detecting liver pathologies. Clinical Science. 2010;120(5):183-93. doi: 10.1042/cs20100297.
104. Berry-Kravis E, Chin J, Hoffmann A, Winston A, Stoner R, LaGorio L, Friedmann K, Hernandez M, Ory DS, Porter FD, O'Keefe JA. Long-Term Treatment of Niemann-Pick Type C1 Disease With Intrathecal 2-Hydroxypropyl-β-Cyclodextrin. Pediatr Neurol. 2018;80:24-34. Epub 20180108. doi: 10.1016/j.pediatrneurol.2017.12.014. PubMed PMID: 29429782; PMCID: PMC5857219.
105. Padilla CJ, Alexander DM, Labor DA, Albert OK, Robbins KP, Berry-Kravis E, Porter FD. Cerebrospinal Fluid and Serum Neuron-Specific Enolase in Niemann-Pick Disease Type C1. American Journal of Medical Genetics Part A. 2025;197(5):e63970. doi: https://doi.org/10.1002/ajmg.a.63970.
106. Lusardi TA, Sandau US, Sakhanenko NA, Baker SCB, Wiedrick JT, Lapidus JA, Raskind MA, Li G, Peskind ER, Galas DJ, Quinn JF, Saugstad JA. Cerebrospinal Fluid MicroRNA Changes in Cognitively Normal Veterans With a History of Deployment-Associated Mild Traumatic Brain Injury. Frontiers in Neuroscience. 2021;15(1051). doi: 10.3389/fnins.2021.720778.
107. World Medical Association Declaration of Helsinki: ethical principles for medical research involving human subjects. Jama. 2013;310(20):2191-4. doi: 10.1001/jama.2013.281053. PubMed PMID: 24141714.
108. Peskind ER, Riekse R, Quinn JF, Kaye J, Clark CM, Farlow MR, Decarli C, Chabal C, Vavrek D, Raskind MA, Galasko D. Safety and acceptability of the research lumbar puncture. Alzheimer Dis Assoc Disord. 2005;19(4):220-5. doi: 10.1097/01.wad.0000194014.43575.fd. PubMed PMID: 16327349.
109. Shi M, Bradner J, Hancock AM, Chung KA, Quinn JF, Peskind ER, Galasko D, Jankovic J, Zabetian CP, Kim HM, Leverenz JB, Montine TJ, Ginghina C, Kang UJ, Cain KC, Wang Y, Aasly J, Goldstein D, Zhang J. Cerebrospinal fluid biomarkers for Parkinson disease diagnosis and progression. Ann Neurol. 2011;69(3):570-80. Epub 20110311. doi: 10.1002/ana.22311. PubMed PMID: 21400565; PMCID: PMC3117674.
110. Ory DS, Ottinger EA, Farhat NY, King KA, Jiang X, Weissfeld L, Berry-Kravis E, Davidson CD, Bianconi S, Keener LA, Rao R, Soldatos A, Sidhu R, Walters KA, Xu X, Thurm A, Solomon B, Pavan WJ, Machielse BN, Kao M, Silber SA, McKew JC, Brewer CC, Vite CH, Walkley SU, Austin CP, Porter FD. Intrathecal 2-hydroxypropyl-β-cyclodextrin decreases neurological disease progression in Niemann-Pick disease, type C1: a non-randomised, open-label, phase 1–2 trial. The Lancet. 2017;390(10104):1758-68. doi: https://doi.org/10.1016/S0140-6736(17)31465-4.
111. Gelsthorpe ME, Baumann N, Millard E, Gale SE, Langmade SJ, Schaffer JE, Ory DS. Niemann-Pick type C1 I1061T mutant encodes a functional protein that is selected for

endoplasmic reticulum-associated degradation due to protein misfolding. J Biol Chem. 2008;283(13):8229-36. Epub 20080123. doi: 10.1074/jbc.M708735200. PubMed PMID: 18216017; PMCID: PMC2276376.
112. Pfrieger FW, Vitale N. Cholesterol and the journey of extracellular vesicles. J Lipid Res. 2018;59(12):2255-61. Epub 2018/04/22. doi: 10.1194/jlr.R084210. PubMed PMID: 29678958; PMCID: PMC6277151.
113. Gabandé-Rodríguez E, Pérez-Cañamás A, Soto-Huelin B, Mitroi DN, Sánchez-Redondo S, Martínez-Sáez E, Venero C, Peinado H, Ledesma MD. Lipid-induced lysosomal damage after demyelination corrupts microglia protective function in lysosomal storage disorders. The EMBO Journal. 2019;38(2):e99553. doi: https://doi.org/10.15252/embj.201899553.
114. Sandau US, Duggan E, Shi X, Smith SJ, Huckans M, Schutzer WE, Loftis JM, Janowsky A, Nolan JP, Saugstad JA. Methamphetamine use alters human plasma extracellular vesicles and their microRNA cargo: An exploratory study. J Extracell Vesicles. 2020;10(1):e12028. Epub 2021/02/23. doi: 10.1002/jev2.12028. PubMed PMID: 33613872; PMCID: PMC7890470.
115. Das S, Ansel KM, Bitzer M, Breakefield XO, Charest A, Galas DJ, Gerstein MB, Gupta M, Milosavljevic A, McManus MT, Patel T, Raffai RL, Rozowsky J, Roth ME, Saugstad JA, Van Keuren-Jensen K, Weaver AM, Laurent LC. The Extracellular RNA Communication Consortium: Establishing Foundational Knowledge and Technologies for Extracellular RNA Research. Cell. 2019;177(2):231-42. doi: 10.1016/j.cell.2019.03.023. PubMed PMID: 30951667; PMCID: PMC6601620.
116. Shekari F, Alibhai FJ, Baharvand H, Börger V, Bruno S, Davies O, Giebel B, Gimona M, Salekdeh GH, Martin-Jaular L, Mathivanan S, Nelissen I, Nolte-'t Hoen E, O'Driscoll L, Perut F, Pluchino S, Pocsfalvi G, Salomon C, Soekmadji C, Staubach S, Torrecilhas AC, Shelke GV, Tertel T, Zhu D, Théry C, Witwer K, Nieuwland R. Cell culture-derived extracellular vesicles: Considerations for reporting cell culturing parameters. Journal of Extracellular Biology. 2023;2(10):e115. doi: https://doi.org/10.1002/jex2.115.
117. Zhang Q, Higginbotham JN, Jeppesen DK, Yang YP, Li W, McKinley ET, Graves-Deal R, Ping J, Britain CM, Dorsett KA, Hartman CL, Ford DA, Allen RM, Vickers KC, Liu Q, Franklin JL, Bellis SL, Coffey RJ. Transfer of Functional Cargo in Exomeres. Cell Rep. 2019;27(3):940-54 e6. Epub 2019/04/09. doi: 10.1016/j.celrep.2019.01.009. PubMed PMID: 30956133; PMCID: PMC6559347.
118. Blomqvist M, Zetterberg H, Blennow K, Månsson JE. Sulfatide in health and disease. The evaluation of sulfatide in cerebrospinal fluid as a possible biomarker for neurodegeneration. Mol Cell Neurosci. 2021;116:103670. Epub 20210923. doi: 10.1016/j.mcn.2021.103670. PubMed PMID: 34562592.
119. Mirzaian M, Kramer G, Poorthuis BJ. Quantification of sulfatides and lysosulfatides in tissues and body fluids by liquid chromatography-tandem mass spectrometry. J Lipid Res. 2015;56(4):936-43. Epub 20150127. doi: 10.1194/jlr.M057232. PubMed PMID: 25632048; PMCID: PMC4373750.
120. Lloyd-Evans E, Morgan AJ, He X, Smith DA, Elliot-Smith E, Sillence DJ, Churchill GC, Schuchman EH, Galione A, Platt FM. Niemann-Pick disease type C1 is a sphingosine storage disease that causes deregulation of lysosomal calcium. Nat Med. 2008;14(11):1247-55. Epub 2008/10/28. doi: 10.1038/nm.1876. PubMed PMID: 18953351.
121. Pescador N, Pérez-Barba M, Ibarra JM, Corbatón A, Martínez-Larrad MT, Serrano-Ríos M. Serum Circulating microRNA Profiling for Identification of Potential Type 2 Diabetes and Obesity Biomarkers. PLOS ONE. 2013;8(10):e77251. doi: 10.1371/journal.pone.0077251.

122. Mangas A, Pérez-Serra A, Bonet F, Muñiz O, Fuentes F, Gonzalez-Estrada A, Campuzano O, Rodriguez Roca JS, Alonso-Villa E, Toro R. A microRNA Signature for the Diagnosis of Statins Intolerance. Int J Mol Sci. 2022;23(15). Epub 20220724. doi: 10.3390/ijms23158146. PubMed PMID: 35897722; PMCID: PMC9330734.
123. Carvalho G, Payolla T, Brandão-Lima P, Sarti F, Fisberg R, Rogero M. Relationship Among the Presence of Metabolic Syndrome, Weight Status and Plasma miRNA Expression in Older Adults From the Healthy Survey of São Paulo: A Population-Based Study. Current Developments in Nutrition. 2021;5:5. doi: https://doi.org/10.1093/cdn/nzab033_005.
124. Guha D, Lorenz DR, Misra V, Chettimada S, Morgello S, Gabuzda D. Proteomic analysis of cerebrospinal fluid extracellular vesicles reveals synaptic injury, inflammation, and stress response markers in HIV patients with cognitive impairment. Journal of Neuroinflammation. 2019;16(1):254. doi: 10.1186/s12974-019-1617-y.
125. Volkner C, Liedtke M, Hermann A, Frech MJ. Pluripotent Stem Cells for Disease Modeling and Drug Discovery in Niemann-Pick Type C1. Int J Mol Sci. 2021;22(2). Epub 2021/01/16. doi: 10.3390/ijms22020710. PubMed PMID: 33445799; PMCID: PMC7828283.
126. Burbulla LF, Mc Donald JM, Valdez C, Gao F, Bigio EH, Krainc D. Modeling Brain Pathology of Niemann-Pick Disease Type C Using Patient-Derived Neurons. Mov Disord. 2021;36(4):1022-7. Epub 2021/01/14. doi: 10.1002/mds.28463. PubMed PMID: 33438272.
127. Pugach EK, Feltes M, Kaufman RJ, Ory DS, Bang AG. High-content screen for modifiers of Niemann-Pick type C disease in patient cells. Hum Mol Genet. 2018;27(12):2101-12. doi: 10.1093/hmg/ddy117. PubMed PMID: 29659804; PMCID: PMC5985738.
128. Zervas M, Dobrenis K, Walkley SU. Neurons in Niemann-Pick disease type C accumulate gangliosides as well as unesterified cholesterol and undergo dendritic and axonal alterations. J Neuropathol Exp Neurol. 2001;60(1):49-64. doi: 10.1093/jnen/60.1.49. PubMed PMID: 11202175.
129. Toribio V, Morales S, López-Martín S, Cardeñes B, Cabañas C, Yáñez-Mó M. Development of a quantitative method to measure EV uptake. Scientific Reports. 2019;9(1):10522. doi: 10.1038/s41598-019-47023-9.
130. Rosenbaum AI, Maxfield FR. Niemann-Pick type C disease: molecular mechanisms and potential therapeutic approaches. J Neurochem. 2011;116(5):789-95. Epub 20110107. doi: 10.1111/j.1471-4159.2010.06976.x. PubMed PMID: 20807315; PMCID: PMC3008286.
131. Lu A. Endolysosomal cholesterol export: More than just NPC1. Bioessays. 2022;44(10):e2200111. Epub 20220807. doi: 10.1002/bies.202200111. PubMed PMID: 35934896.
132. Lu A, Wawro P, Morgens DW, Portela F, Bassik MC, Pfeffer SR. Genome-wide interrogation of extracellular vesicle biology using barcoded miRNAs. eLife. 2018;7:e41460. doi: 10.7554/eLife.41460.
133. Bonora M, Morganti C, van Gastel N, Ito K, Calura E, Zanolla I, Ferroni L, Zhang Y, Jung Y, Sales G, Martini P, Nakamura T, Lasorsa FM, Finkel T, Lin CP, Zavan B, Pinton P, Georgakoudi I, Romualdi C, Scadden DT, Ito K. A mitochondrial NADPH-cholesterol axis regulates extracellular vesicle biogenesis to support hematopoietic stem cell fate. Cell Stem Cell. 2024;31(3):359-77.e10. doi: 10.1016/j.stem.2024.02.004. PubMed PMID: 38458178; PMCID: PMC10957094.
134. Kestecher BM, Németh K, Ghosal S, Sayour NV, Gergely TG, Bodnár BR, Försönits AI, Sódar BW, Oesterreicher J, Holnthoner W, Varga ZV, Giricz Z, Ferdinandy P, Buzás EI, Osteikoetxea X. Reduced circulating CD63(+) extracellular vesicle levels associate with

atherosclerosis in hypercholesterolaemic mice and humans. Cardiovasc Diabetol. 2024;23(1):368. Epub 20241017. doi: 10.1186/s12933-024-02459-w. PubMed PMID: 39420340; PMCID: PMC11487797.
135. Saint-Pol J, Fenart L. CD63, a new therapeutical candidate for cholesterol homeostasis regulation through extracellular vesicles? Extracell Vesicles Circ Nucl Acids. 2025;6(1):166-70. Epub 20250319. doi: 10.20517/evcna.2024.92. PubMed PMID: 40206806; PMCID: PMC11977374.

APPENDIX A:

Advancing rare disease clinical trials on an international scale: Barriers and emerging solutions

Sarah Catherine Hawthorne[1]; Yonaida Valentine[2]; Ankita Arora [3], Felicia Lim[4]

1. Department of Anesthesiology & Perioperative Medicine, Oregon Health & Science University, OR, USA
2. Department of Chemistry, Ohio State University, Ohio, USA
3. Department of Genetics, University of Colorado Anshutz Medical Campus, Colorado, USA
4. Medical Oncology, Dana-Farber Cancer Institute, Boston MA

MIT Science Policy Review. July 2025.

Abstract: Rare diseases affect over 300 million people worldwide, yet only 5% of these conditions have approved treatments. A key obstacle to rare disease drug development is designing clinical trials that can accommodate small patient populations and high disease heterogeneity. Increasingly, rare disease clinical trials are being conducted across multiple countries, which improves patient recruitment and therapeutic validity. However, international clinical trials introduce complex regulatory, financial, legal, and ethical challenges. These challenges can impede trial execution and ultimately delay access to treatment, particularly in low- and middle-income countries (LMICs). In this review, we explore the evolving landscape of international rare disease clinical trials. We discuss current barriers and strategies to harmonize global regulations, incentivize financial investment, adapt intellectual property frameworks, and enhance LMIC participation. By identifying both structural gaps and promising initiatives, we aim to provide a resource that supports more effective and globally inclusive rare disease research.

APPENDIX B:

Cerebrospinal Fluid MicroRNA Changes in Cognitively Normal Veterans with a History of Deployment-Associated Mild Traumatic Brain Injury

Theresa A Lusardi [1], Ursula S Sandau [2], Nikita A Sakhanenko [3], **Sarah Catherine B Baker [2]**, Jack T Wiedrick [4], Jodi A Lapidus [4], Murray A Raskind [5 6], Ge Li [5 6 7], Elaine R Peskind [5 6], David J Galas [3], Joseph F Quinn [8 9 10], Julie A Saugstad [2]

[1]Knight Cancer Institute, Cancer Early Detection Advanced Research Center, Oregon Health & Science University, Portland, OR, United States.
[2]Department of Anesthesiology & Perioperative Medicine, Oregon Health & Science University, Portland, OR, United States.
[3]Pacific Northwest Research Institute, Seattle, WA, United States.
[4]Biostatistics & Design Program, Oregon Health & Science University, Portland, OR, United States.
[5]Northwest Mental Illness, Research, Education, and Clinical Center, VA Puget Sound Health Care System, Seattle, WA, United States.
[6]Department of Psychiatry and Behavioral Sciences, University of Washington School of Medicine, Seattle, WA, United States.
[7]Geriatric Research Education and Clinical Center, VA Puget Sound Health Care System, Seattle, WA, United States.
[8]Department of Neurology, Oregon Health & Science University, Portland, OR, United States.
[9]Parkinson Center and Movement Disorders Program, School of Medicine, Oregon Health & Science University, Portland, OR, United States.
[10]Portland VAMC Parkinson's Disease Research, Education, and Clinical Center, Portland, OR, United States.

Frontiers in Neuroscience. September 2021.

Abstract: A history of traumatic brain injury (TBI) increases the odds of developing Alzheimer's disease (AD). The long latent period between injury and dementia makes it difficult to study molecular changes initiated by TBI that may increase the risk of developing AD. MicroRNA (miRNA) levels are altered in TBI at acute times post-injury (<4 weeks), and in AD. We hypothesized that miRNA levels in cerebrospinal fluid (CSF) following TBI in veterans may be indicative of increased risk for developing AD. Our population of interest is cognitively normal veterans with a history of one or more mild TBI (mTBI) at a chronic time following TBI. We measured miRNA levels in CSF from three groups of participants: (1) community controls with no lifetime history of TBI (ComC); (2) deployed Iraq/Afghanistan veterans with no lifetime history of TBI (DepC), and (3) deployed Iraq/Afghanistan veterans with a history of repetitive blast mTBI (DepTBI). CSF samples were collected at the baseline visit in a longitudinal, multimodal assessment of Gulf War veterans, and represent a heterogenous group of male

veterans and community controls. The average time since the last blast mTBI experienced was 4.7 ± 2.2 years [1.5 - 11.5]. Statistical analysis of TaqMan^{TM} miRNA array data revealed 18 miRNAs with significant differential expression in the group comparisons: 10 between DepTBI and ComC, 7 between DepC and ComC, and 8 between DepTBI and DepC. We also identified 8 miRNAs with significant differential detection in the group comparisons: 5 in DepTBI vs. ComC, 3 in DepC vs. ComC, and 2 in DepTBI vs. DepC. When we applied our previously developed multivariable dependence analysis, we found 13 miRNAs (6 of which are altered in levels or detection) that show dependencies with participant phenotypes, e.g., ApoE. Target prediction and pathway analysis with miRNAs differentially expressed in DepTBI vs. either DepC or ComC identified canonical pathways highly relevant to TBI including senescence and ephrin receptor signaling, respectively. This study shows that both TBI and deployment result in persistent changes in CSF miRNA levels that are relevant to known miRNA-mediated AD pathology, and which may reflect early events in AD**.**